Substituent effects on the electrocatalytic activity of cobalt phthalocyanine in the presence of graphene quantum dots

A thesis submitted in fulfilment of the requirements for the degree of

Master of Science

Of

Rhodes University

By

Sixolile Sibongiseni Centane

April 2018

Dedicated to:

My dearest parents Funani and Iviwe

My siblings Dunyiswa, Mangaliso and Mxolisi.

“Perseverance is not a long race; it is many short races one after the other…” Walter Elliot

Acknowledgements

The work reported in this work would have not been possible without the following people:

My supervisor, Professor Tebello Nyokong whose shoulders I stand on as a young black upcoming scientist. I am grateful for your unending support, tough love and encouragement to be better than what I ever imagined myself to ever be. I thank you for the opportunities that you have afforded me, which were beyond what I could have ever imagined. I thank you that you kept pushing beyond what I had settled for, and helped me realize my true potential. I thank you for believing in me even when I did not, your faith in me challenged me to become better every day. Thank you so much Prof.

Thank you to Dr Fethi Bedioui and Dr Anne Varenne of Chimie Paris Tech, France for being great hosts during my stay in your lab.

I would like to acknowledge the National Research Fund (NRF) for financial support during my postgraduate studies.

Thank you to Dr Munyaradzi Shumba for teaching me electrochemistry with so much patience and zeal. Thank you to Dr Edward Sekhosana and Dr David Oluwale for their assistance in the lab. I am also grateful to Njemuwa “Papa Nwaji” Nwaji for his constant push and scientific advice throughout my master’s degree. To my best friend Keamogetse Charlotte Tshenkeng, you made every day worthwhile, thank you for your support and love hle tsala yaka. Last but not least a big thank you to my mommy, daddy and my siblings I couldn’t have done it without your love and constant cheering.

Abstract

The electrocatalytic activity of metallophthalocyanines derivatives is explored. Cobalt monocarboxyphenoxy phthalocyanine (**1**), cobalt tetracarboxyphenoxy phthalocyanine (**2**), cobalt tetraaminophenoxy phthalocyanine (**3**) and cobalt tris-(tert-butylphenoxy) monocarboxyphenoxy phthalocyanine (**4**) are the phthalocyanines employed in this work. The metallophthalocyanines were employed alone as well as in the presence of the carbon based graphene quantum dots. The electrocatalytic behaviour of functionalized GQDs is also explored herein. The catalytic processes studies were conducted on a glassy carbon electrode surface. Modification of the electrode was achieved by the adsorption method. The materials were adsorbed either alone, as premixed/covalently linked GQDs/Pc conjugates or sequentially. Sequentially adsorbed electrodes involved the phthalocyanines on top or beneath GQDs. Sequentially modified electrodes where the phthalocyanine had higher currents and low detection limits than when the phthalocyanine is underneath. Premixed conjugates showed better activity than the covalently formed conjugates. The nanomaterials synthesized and used in this work were characterized using transmission electron microscopy, UV-Vis spectroscopy, dynamic light scattering, Raman spectroscopy, X-ray diffraction, Atomic Force Microscopy and X-ray photoelectron spectroscopy. The modified electrodes were characterized using cyclic voltammetry and scanning electrochemical spectroscopy. The electrocatalytic activity of the modified electrodes towards the oxidation of hydrazine was evaluated using cyclic voltammetry and chronoamperometry. Superior catalytic activity was observed for the conjugates compared to that of the individual conjugates.

Contents

List of Abbreviations

AFM	atomic force microscopy
CV	cyclic voltammetry
CZE	capillary zone electrophoresis
DCM	dichloromethane
DMF	N, N-dimethylformamide
E	potential
EDC	1-Ethy-3-(3-dimethylaminopropyl)-carbodiimide
FT-IR	Fourier transform - infrared
GCE	glassy carbon electrode
GCP	glassy carbon plate
GQDs	graphene quantum dots
HOMO	highest occupied molecular orbital
LOD	limit of detection
LUMO	lowest unoccupied molecular orbital
NHS	N-hydroxysuccinimide
Redox	reduction/oxidation
SECM	scanning electrochemical microscopy
THF	tetrahydrofuran
TEM	transmission electron microscopy
UME	ultramicroelectrode
UV-Vis	ultraviolet-visible
XRD	x-ray diffraction
XPS	x-ray photoelectron microscopy

List of symbols

α	Peripheral Position
β	Non-Peripheral Position
e^-	electron
v	scan rate
A	absorbance, area of electrode
C	concentration
ΔEp	peak to peak separation
Ep	peak potential
I	current
I_p	peak current
M	molar concentration
T	temperature
π	pi
λ	wavelength
k	catalytic rate constant

Chapter 1: Introduction

This chapter gives an overview of metallophthalocyanines (MPcs), graphene quantum dots (GQDs) and the conjugates

1.1. Metallophthalocyanines Overview

1.1.1. General Structure and Application

Phthalocyanines (Pcs) are two dimensional 18 π-electron conjugated macrocyclic systems formed from an alternate of carbon and nitrogen atoms [**1, 2**], **Fig 1.1**. The Pc ring can host more than 70 central metal and metalloids which results in the formation of metallophthalocyanines (MPcs) [**2, 3**]. Depending on the metal, the molecular electronic and optical properties may be tailored while leaving the overall geometric structure invariant [**1**, **4**]. Further structural modification may involve axial ligation and ring substitution at the peripheral (α) and non-peripheral (β) positions. The ability of an MPc to host an axial ligand is determined by the type and charge of its central metal. The diverse electronic, optical and structural properties MPcs have allowed them for applications in electrocatalysis [**5**], photovoltaic cell [**6**], bioimaging [**7**], non-linear optics [**8**] and photodynamic therapy [**9**].

The use of MPcs as electrocatalysts is made possible by their macrocyclic nature and π-electron system which grants them the ability to undergo fast redox processes [**10**]. The central metal ions of the phthalocyanines can reversibly bind to reactants and hence exhibit good electrocatalytic activity to various important reactions. The focus of this work is on the electrocatalytic behaviour of CoPc derivatives. Cobalt has accessible d-orbitals between the highest occupied molecular orbital (HOMO) and the lowest occupied molecular orbital (LUMO) which is essential for redox processes [**11**].

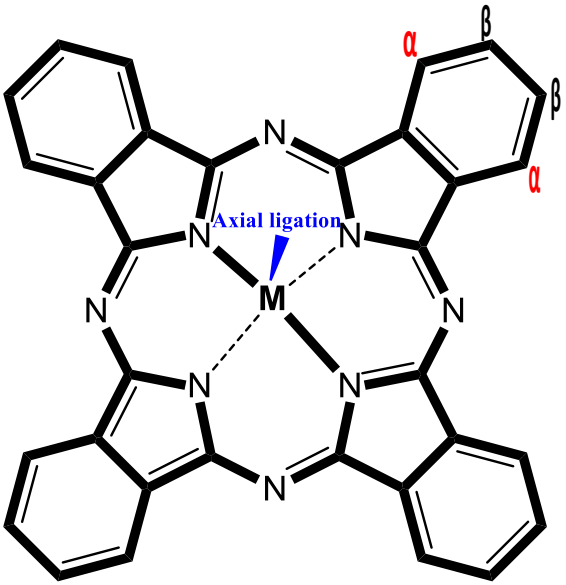

Fig. 1.1 A typical MPc structure with possible positions for modification.

1.1.2. Synthesis

The general synthesis of MPcs involves a precursor, a catalyst and a metal salt. The precursors used may involve phthalic acid derivatives or a phthalonitrile [**12**]. The used precursor can be modified to fit the desired substitution on the synthesized MPc.

1.1.2.1. Tetra Substituted MPcs

The synthesis of the symmetrical tetra substituted MPcs involves cyclotetramerisation of the substituted precursor in the presence of a metal salt and a catalyst at relatively high temperatures, **Scheme 1.1**. Substituents can sometimes be introduced onto an already existing MPc [**13**]. Isomerisation is possible during synthesis owing to the different positions on the Pc ring available for substitution [**14**]. The yields depend on both the substituent and an amount of the phthalonitrile relative to the metal salt [**15**].

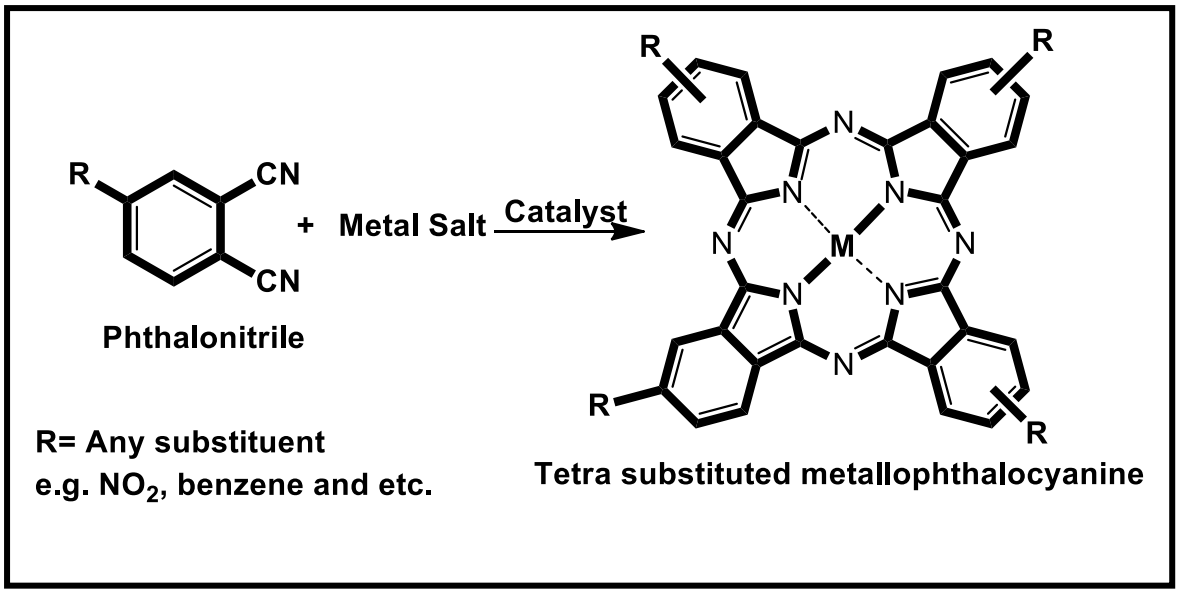

Scheme 1.1 Synthesis strategy for a tetra substituted MPc.

1.1.2.2. Mono Substituted MPcs

These are sometimes referred to as low symmetry MPcs. Their synthesis involves the use of two different phthalonitriles with the desired substituent, a catalyst and the metal salt [**16**]. **Scheme 1.2** shows the possible isomers that can form during synthesis of mono substituted MPcs. Stoichiometric quantities of the precursors are set such that asymmetrical products are formed. The ratio 3:1 is favourable for the formation of A_3B and AB_3 type phthalocyanines (where both A and B are representative of the differently substituted phthalonitriles). These phthalocyanines are formed as a mixture along with five other isomers. Column chromatography is employed to obtain the desired product and normally the yields are small.

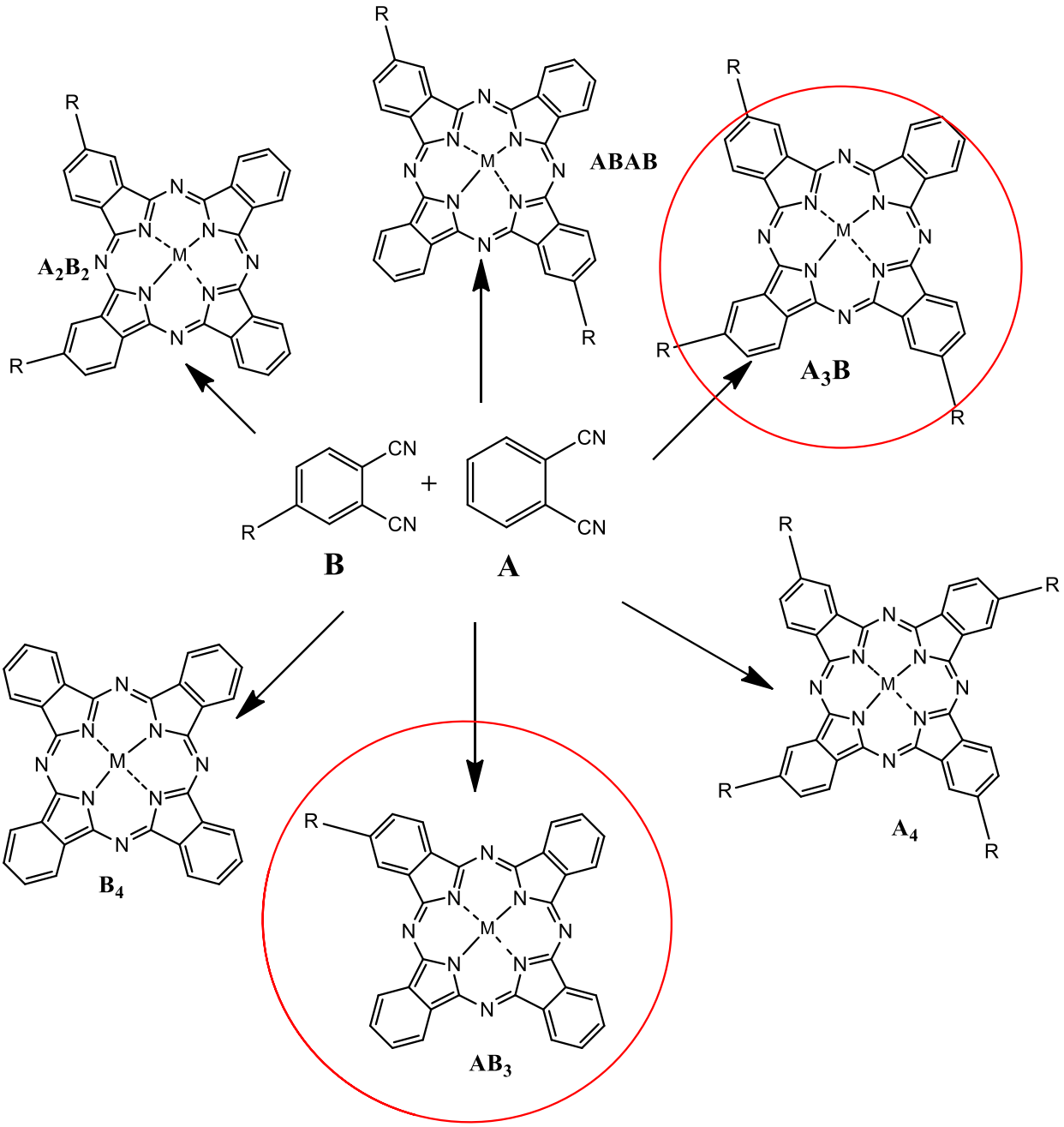

Scheme 1.2 Asymmetric MPc synthesis and possible isomer products

1.1.3. Metallophthalocyanines used in this work

Four different MPcs were used in this work; (i) cobalt monocarboxyphenoxy phthalocyanine (**1**), (ii) cobalt tetracarboxyphenoxy phthalocyanine (**2**) [**17**], (iii) cobalt tetraaminophenoxy phthalocyanine (**3**) [**18**] and (iv) cobalt tris-(*tert*-butylphenoxy) monocarboxyphenoxy phthalocyanine (**4**). The structure of the Pc complexes is shown in **Fig 1.2**: Complexes **2** and **3** are known while complexes **1** and **4** are new.

Complexes **1** and **2** were compared for the effect of the number of substituents on electrocatalytic activity. Complexes **2** and **3** were chosen for studying the effect of the type of substituents i.e. electron donating or withdrawing on their electrocatalytic behaviour. The complex **4** was ideal for studying the significance of the push-pull effect on its electrocatalytic behaviour.

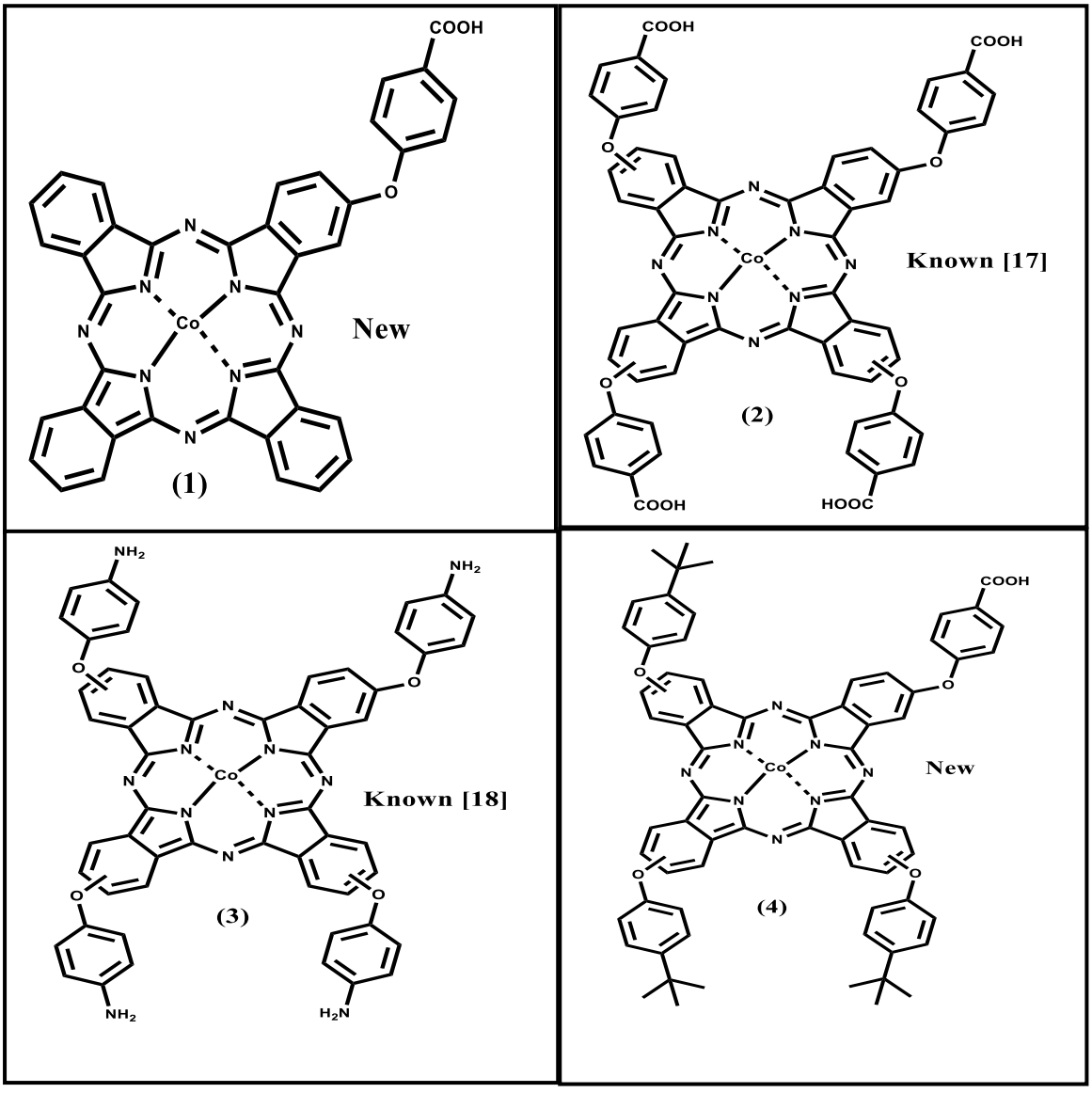

Fig 1.2 Structures of MPcs employed in this work

In electrocatalysis the MPcs are usually adsorbed onto a conductive surface to explore their electrocatalytic activity. However, the use of MPcs as surface modifiers for electrocatalysis is impeded by low conductivity which then affects their electron transfer and electrochemical properties [**19**]. To overcome this, MPcs have been combined with nanomaterials such as single walled nanotubes [**20**] to provide suitable support and enhance conductivity; in this work graphene quantum dots (GQDs) were employed.

1.2. Graphene Quantum Dots (GQDs)

Graphene quantum dots are carbon based nanomaterials with a sp^2 carbon framework [**21**]. They occur as miniscule fragments of graphene sheets and possess sizes within the range 3-10 nm [**22**]. Their size is small enough to cause exciton confinement and quantum size effect. In addition to the sp^2 framework, GQDs have edge functional moieties open for modification and tailored functionality [**23**]. Quantum confinement and edge effects bestows the GQDs with intrinsic properties such as high photostability, chemical inertness, high biocompatibility, fluorescence activity, low toxicity, resistance to photobleaching and high solubility in various solvents [**24, 25**]. The structure of GQDs is ideal for π-π interactions with a wide range of aromatic complexes, while covalent interactions are made possible by the existing edge functional moieties. Resulting interactions may confer new properties to the GQDs or even enhance already existing properties. Their structural flexibility and tunable intrinsic properties have given GQDs precedence over the conventional toxic semiconductor quantum dots. GQDs as a result have found application in various fields such as biosensing [**26**], photocatalysis [**27**], bioimaging [**28**], drug delivery and photosensitization [**29**].

GQDs on their own have found eligibility in electrocatalytic based applications in curtsey of their properties similar to that of graphene. Their high electrical conductivity, carrier mobility, large surface area and high tolerance of strong acid and alkali media have made them irresistible and attractive potential catalysts [**30**]. GQDs have the ability to act as catalysts because their structure is made up of electrocatalytically active sites and edges. Their sp^2 framework and peripheral functional moieties work hand in hand to control their electron transfer abilities. Most importantly, their modification provides control of the existing active sites and therefore measurable electrocatalytic activity. An advantage of GQDs compared to other carbon based materials as electrocatalysts is their 2D morphology which allows for accessibility of almost all atoms and groups that make the material a suitable catalyst. Their π-electron dominated core structure and high surface area allows for perfect grafting onto various electrode surfaces [**22, 31**].

1.2.1. GQDs Synthesis

The synthetic approach towards GQDs can be grouped into two categories known as the bottom up and the top down [**32**]. The former involves the carbonisation or pyrolysis of small organic molecules (e.g. acetic acid), while the latter involves decomposition and exfoliation of cheap carbonaceous materials such as graphene oxide via chemical, electrochemical approaches under harsh conditions. A schematic representation of the bottom up and top down approaches towards GQDs is shown in **Scheme 1.3**, as well as the possible GQDs structures. The approach followed towards the synthesis determines the functional moieties contained on the edges of the GQDs [**33**].

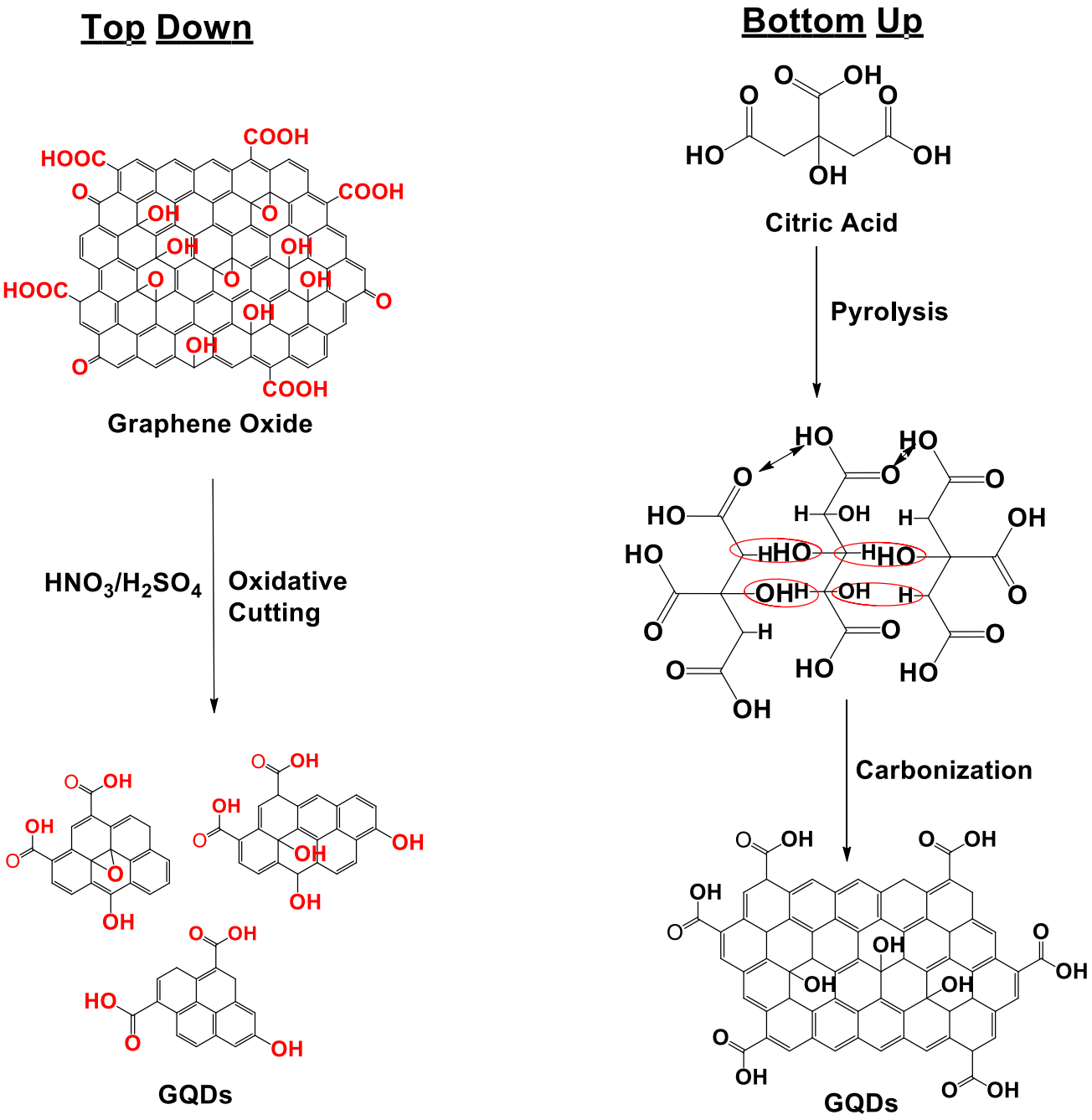

Scheme 1.3 Top down and bottom up approaches towards GQDs synthesis.

1.2.2. Structural Modification of Graphene Quantum Dots

The unique properties of GQDs are structure and size dependant. Structural modification has been a potential strategy used to alter their electronic and chemical properties for the desired application. Generally, GQDs qualify for structural modification at two distinct locations; the basal plane (sp^2 carbon framework) and the edges. Similar to their methods of production, modification approaches can be grouped into two strategies known as the pre-fabrication and post-fabrication method. The pre-fabrication method involves alteration of the parent material prior the full formation of the GQDs, whilst the post-fabrication methods involves direct altering of pre-existing GQDs [**34, 35**]. Various chemical modification methods have been developed for altering the photoluminescence, biocompatibility and conductivity of GQDs.

1.2.2.1. Modification targeting the basal plane

I. Non-covalent π-π interactions

The basal plane of GQDs is predominantly composed of sp^2 carbons and chemically unsaturated. The sp^2 hybridization of the carbon leads to delocalization of the π-electrons. The π-electron rich structure allows for modification of the graphene structure via π-π interactions with wide a range of aromatic complexes. The complexes formed have been found useful in wide range of applications as listed in **Table 1.1**. In this thesis, GQDs were π-π stacked with CoPc derivatives for electrocatalysis, discussed in detail below

II. Controlling Oxygen functionalities

The GQDs surface is heavily oxygenated with various oxygen species like hydroxyl, carboxyl and carbonyl groups. These functional moieties play an important role on the

hydrophilicity, hydrophobicity and conductivity of the GQDs [**34**, **36**]. This diverse chemistry provides chemical handles for further functionalization, and so alteration of GQDs physical properties. According to literature the energy band gap of graphene based nanomaterials is directly proportional to the available oxygen species [**37, 38**]. The reduction of GQDs would entail elimination of the excessive oxygen species thereby narrowing the energy band gap. This manipulation is ideal for conductivity and electron transfer related applications such as electrochemical sensing [**38**]. In this thesis, reduced graphene quantum dots represented as rGQDs were employed. The rGQDs were formed using hydrazine, and as a result have peripheral -NH_2 groups available for covalent linking

III. Heteroatom Doping

Amongst many, heteroatom doping of GQDs is the most popular chemical modification exercised for tuning the electronic properties of GQDs. This process involves the incorporation of a heteroatom onto the GQDs framework. The heteroatom of interest is inherited from a precursor during synthesis. Nitrogen, boron and sulphur doped GQDs have been of most popularity due to the comparable atomic size and valence electrons to carbon [**36, 39**]. In this process some carbon atoms are replaced by heteroatom of interest e.g. N, S or P while leaving the GQD structure unchanged. **Scheme 1.4** demonstrates the synthetic approach towards nitrogen doped graphene quantum dots (NGQDs) via the pre-fabrication [**40**] and post modification method [**41**].

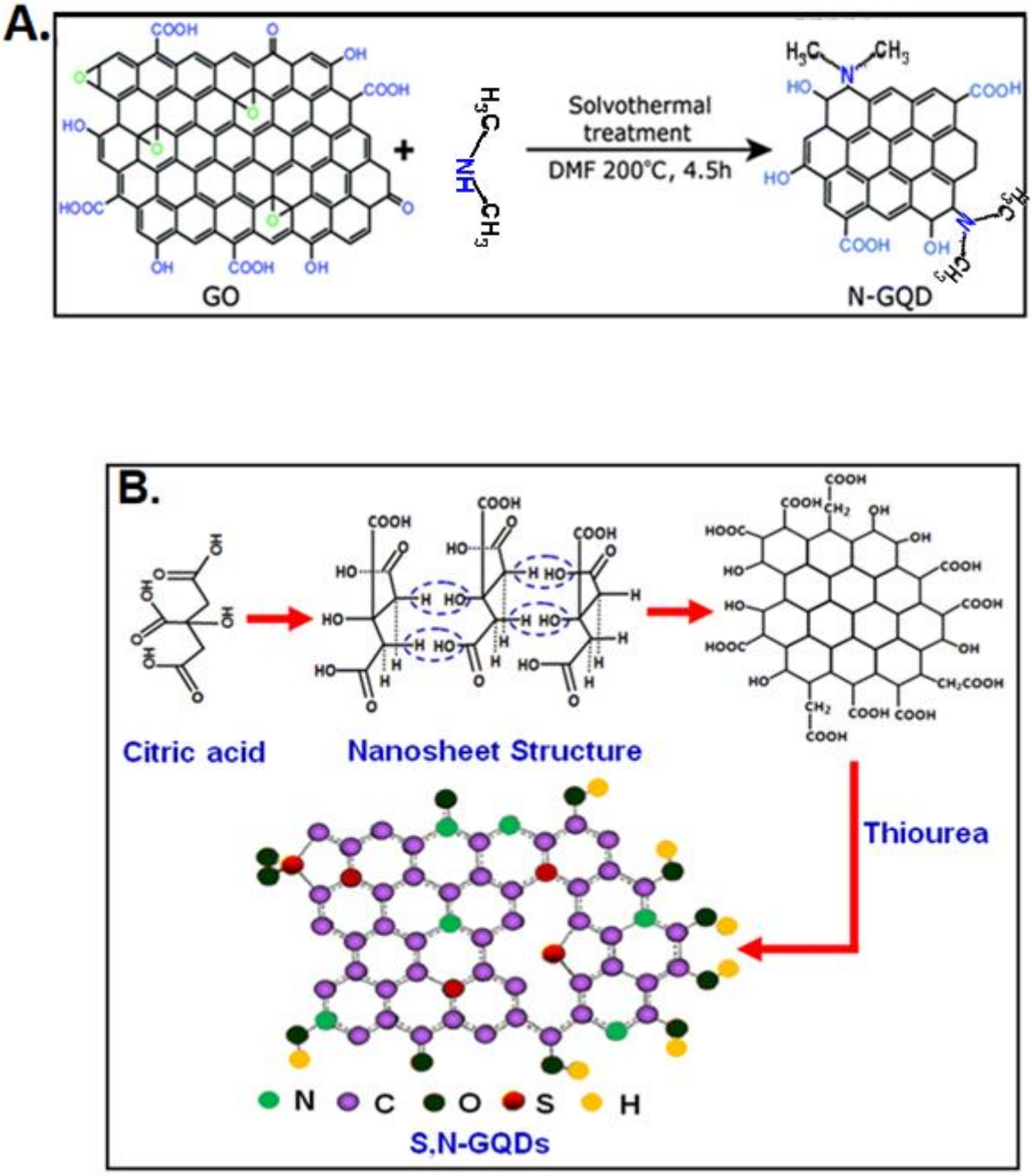

Scheme 1.4 Surface modification of GQDs with nitrogen atoms: (**A**) Shows the pre-fabrication method where the source of nitrogen is added with the reactants such that, the doping takes place simultaneously with the formation of GQDs [**40**]. In (**B**) the post-fabrication method is portrayed, in that the nitrogen source (thiourea) is not involved in the reactants but only added after GQDs have formed [**41**].

1.2.2.2. Modification of GQDs targeting the edges

The edge sites of GQDs are abundantly decorated with reactive carboxylic groups which are convenient for modification. The carboxylic group can undergo reduction to form a hydroxyl group. In addition, the electrophilic carbon of the carboxyl group allows for covalent linking of the GQDs to other materials via an amide bond. GQDs have been linked to various compounds to suit multiple applications as shown in **Table 1.1**.

Using the understanding of the structural flexibility of GQDs, in this thesis pristine GQDs were functionalized with amino groups represented as NH_2GQDs using a novel approach. The resulting functionalized GQDs were then later covalently linked to CoPc derivatives and applied in electrocatalysis studies. The influence of pristine and functionalized GQDs on the electrocatalytic behaviour of CoPc derivatives towards the electrooxidation of hydrazine is presented.

Table 1.1 [**42-51**] shows a list of reported studies conducted using MPc/GQDs conjugates and the types of interactions thereof occurring between the GQDs and MPcs. As **Table 1.1** shows, no asymmetric Pc has been employed with GQDs for electrocatalysis, hence the subject of this thesis. Asymmetry in Pcs plays an important role in the distribution of HOMO-LUMO gap. Apart from one example [**42**], GQDs have not been used together with Pcs for electrocatalysis; hence, this is a subject of this work.

Table 1.1 Few known examples of GQDs/MPc conjugate for various applications.*Structures are shown in **Table 1.2**

Conjugates	**Application**	**Type of interaction**	**References**
FePc-GQDs	Oxygen reduction	Covalent axial ligation	[**42**]
GQDs - $ZnPcS_4$ **(5)**	Molecular sensing	Amide linkage	[**43**]
GQDs –ZnPc	Physicochemical Studies	π-stacking	[**44**]
GQDs-ZnTAPc **(6)**	Fluorescence Sensing	Amide linkage	[**45**]
GQDs-ZnTcPPc **(7)**, GQDs-ZnTmPyPc **(8)**	Fluorescence Sensing	π-stacking	[**45**]
SNGQDs–TEMPO-ZnPc **(9)**, GQDs–TEMPO-ZnPc	Fluorescence sensing	π-stacking	[**46**]
Malemide – GQDs-ZnPc	Fluorescence sensing	π-stacking	[**47**]
GQDs-CoTPyPc **(10)**, GQDs-ZnTPyPc **(11)**	Physicochemical Studies	π-stacking	[**48**]
GQDs-ZnPc, Mercaptopyridine-ZnPc-GQDs (**12**)	Flourescence sensing	π-stacking	[**49**]
GQDs – Polystyrene– ZnPc	Photocatalysis	π-stacking	[**50**]
NGQDs -ZnPc, SNGQDs – ZnPc	Non-linear Optics	Amide linkage	[**51**]

Table 1.2 Structures and names of Pc used in Table 1.1

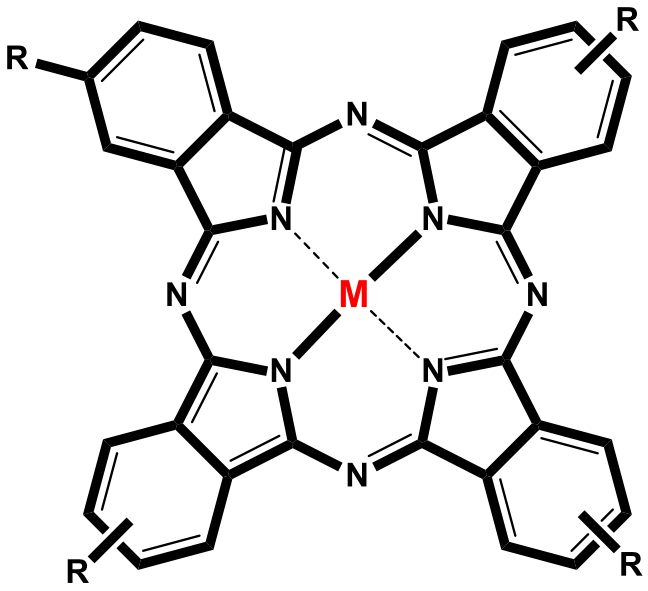

SUBSTITUENTS	COMPLEXES
R= SO_3^- ($ZnPcS_4$) M= Zn	Zinc tetrasulfonated Pc (5)
R= NH_2 (ZnTAPc) M= Zn	Zinc tetraamino Pc (6)
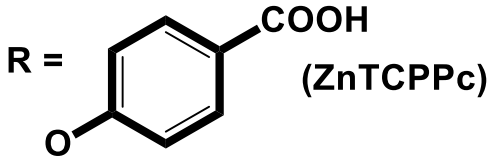 (ZnTCPPc) M= Zn	Zn tetracarboxyphenoxy Pc (7)
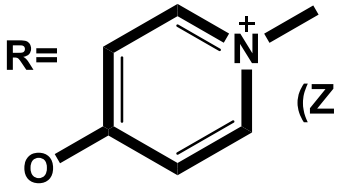 (ZnTmPyPc) M=Zn	Zn tetrapyridiloxy Pc (8)

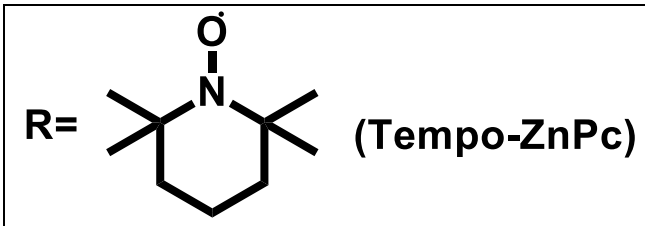	**Zinc tempo substituted Pc (9)**
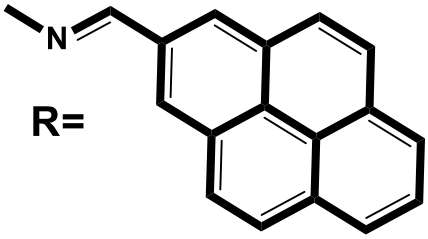	**Cobalt Pyrene derivatized Pc (10)** **Zinc Pyrene derivatized Pc (11)**
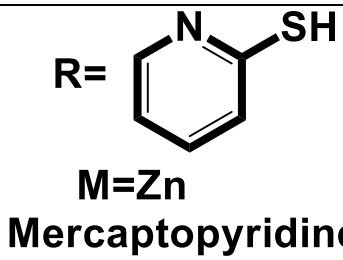	**Zinc tetra Mercaptopyridine Pc (12)**

1.3. MPc/GQDs hybrids used in this work

The MPc/GQDs hybrids used in this work are listed in **Table 1.3**. The nanohybrids are divided into groups in association of interactions and studies conducted.

1.3.1. Non-covalent interactions

Non covalent interactions differ from covalent interactions in that they do not involve sharing of electrons but the variation of electromagnetic interactions between molecules. There are certain structural requirements to be met by interacting molecules in order for the categorical interactions to occur. For example Van der Waals forces require an induced or permanent dipole on each interacting molecules.

This work focuses on π-π interactions between GQDs and several CoPc derivatives. These non-covalent interactions occur between π-orbitals of aromatic systems. These interactions have played an important role in the formation of supermolecules for various applications. The interactions are governed by the geometry, type and nature of aromatic compounds interacting [**52**]. The aromaticity of GQDs and MPcs is an established fact, and as a result both molecules qualify for π-π interactions. However, there is limited understanding on the structural contributions of each molecule to the interactions. The effect of the substituents on the interactions between the GQDs and MPcs as well as the arising properties is studied herein.

The Hunters-Sanders model has been the basis for understanding interactions between aromatic systems. The model instead of attributing the strength and nature of π-π interactions between aromatic molecules solely on attractive electronic interactions, considers other viable contributors which include solvophobic effects, charge transfer, desolvation, induction energy, Van de Waals and electrostatic interactions [**52- 54**].

In this work GQDs were π-π stacked onto CoPc derivatives and tested for electrocatalysis. Reports have shown that carbon based nanomaterials have the ability to improve the electrocatalytic activity of MPcs towards various analytes [**18, 20**]. The GQDs are utilized as agents to extend the π-electron system of the MPcs. The electrocatalytic behaviour of the resulting conjugates was studied. Attempts to explain and understand the contribution of the structural arrangement and substituent of the respective Pc molecules to the interactions were made. The individual MPcs are stacked to form hybrids **1**(π)GQDs, **2**(π)GQDs, **3**(π)GQDs, **4**(π)NH_2GQDs and **4**(π)rGQDs. The MPcs, GQDs were drop casted onto an electrode and employed and tested for electrocatalysis when alone and as hybrids.

The complexes **1** to **3** were also sequentially adsorbed onto an electrode with GQDs. Sequential adsorption involves drop casting of MPcs complex solution onto an electrode followed by GQDs and vice versa. The electrodes are denoted as GQD-Pc (seq) where GQDs are adsorbed first followed by the Pc and Pc-GQDs (seq) where the set of events are reversed, **Table 1.3**. The resulting hybrids were also tested for electrocatalysis.

1.3.2. Covalent interactions

Pristine GQDs were modified such that they contained terminal NH_2 groups (represented as NH_2GQDs and rGQDs) available for covalent linking to the carboxylic end of the complex **4** via an amide bond. The effect of functionalized GQDs on the electrocatalytic behaviour of a push-pull phthalocyanine when covalently linked is explored. The way in which these GQDs link to the complex **4** to form the resulting complex is used as basis to explain the electrocatalytic behaviour of the resulting hybrids. **Scheme 1.5** shows an example a conjugate formed from covalent interactions between GQDs and ZnPc via an amide bond. The covalently formed hybrids are labelled as **4**@rGQDs (where rGQDs stands for reduced GQDs containing NH_2 groups from hydrazine reducing agent) and **4**@NH_2GQDs (NH_2GQDs for amino functionalized GQDs). These hybrids were as well drop cast onto an electrode and tested for electrocatalysis towards the electrooxidation of hydrazine.

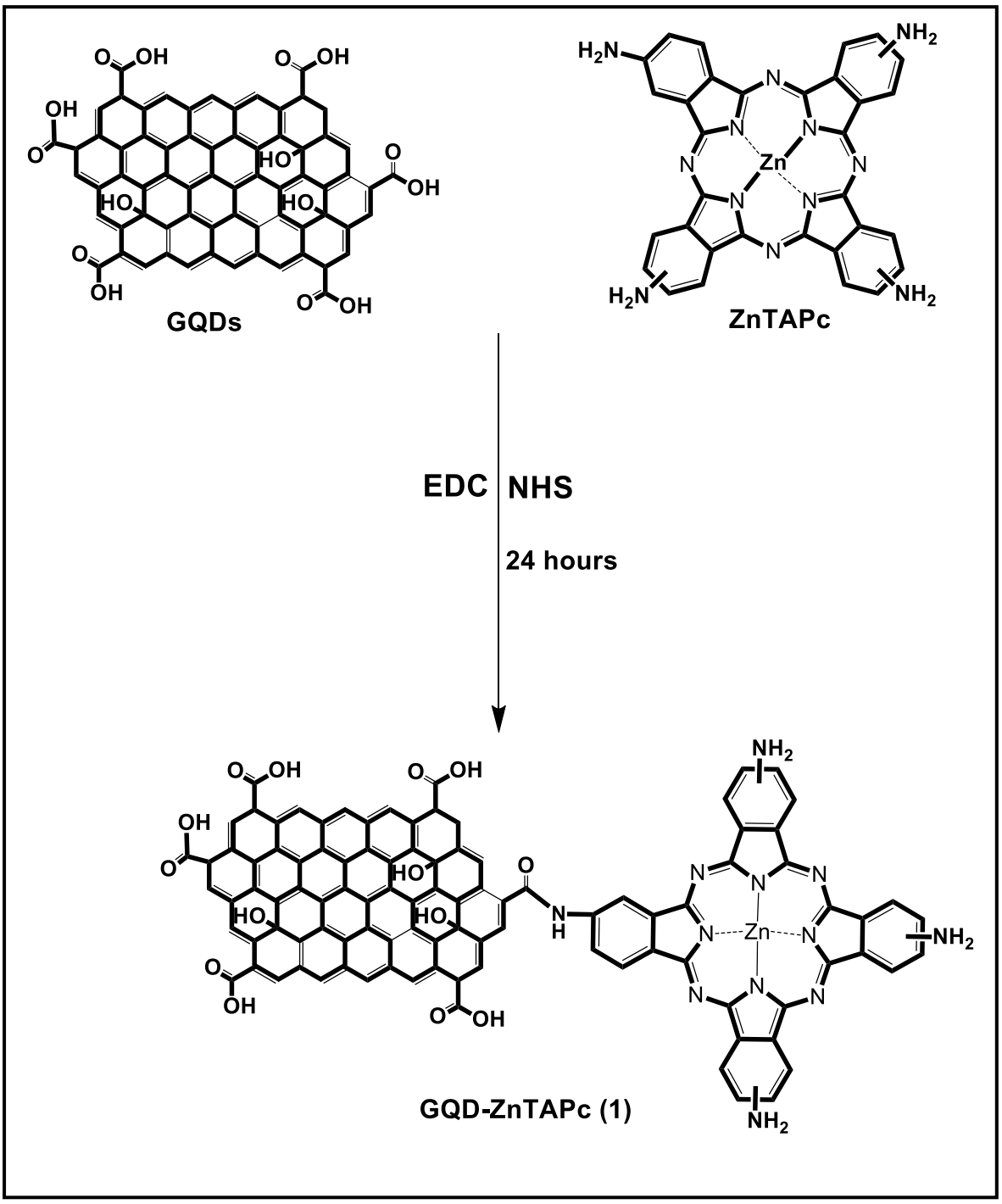

Scheme 1.5 A schematic of pristine GQDs covalently linked onto a ZnPc via an amide bond. Where EDC = 1-Ethyl-3-(3-dimethylaminopropyl) carbodiimide NHS=N-Hydroxysuccinimide and ZnTAPc = Zinc Tetra Amino Phthalocyanine [**47**]

Table 1.3 Summary of all MPc and MPc/GQDs hybrids applied in this work

Modified Electrodes[a]	
Non-covalent MPc/GQDs hybrids	GCE/**3**(π)GQDs
GCE/**1**	GCE/**3**-GQDs (seq)
GCE/**1**(π)GQDs	GCE/GQDs-**3** (seq)
GCE/**1**-GQDs (seq)	GCE/**4**
GCE/GQDs-**1** (seq)	GCE/**4**(π)rGQDs
GCE/**2**	GCE/ **4**(π)NH_2GQDs
GCE/**2**(π)GQDs	**Covalently linked MPcs/GQDs**
GCE/**2**-GQDs (seq)	GCE/**4**@rGQDs
GCE/GQDs-**2** (seq)	GCE/**4**@NH_2GQDs
GCE/**3**	

[a]seq = sequentially adsorbed electrodes

GCE = glassy carbon electrode

1.4. Electrocatalysis

Electrocatalysis is the process in which an electrochemical reaction rate is accelerated in the presence of a catalyst. An electrocatalyst can be defined as an electrode material with an ability to specifically interact with species involved in a reaction and can alter the energetics of the reaction while it remains unaltered even after the reaction has reached completion [**55, 56**]. The activity of an electrocatalyst is dependent on its ability to undergo reduction or oxidation.

1.4.1. MPcs as electrocatalysts

The use of MPcs in electrocatalysis involves their immobilization on a solid surface to form an electroactive surface that acts as an electron mediator in a redox reaction involving a test analyte [10]. The electrocatalytic behaviour of these MPcs on an electrode surface is directed by the ability to transition between oxidation states by either gaining or losing an electron to the electrode. MPcs with electroactive transition metals such as cobalt have redox processes occurring at the ring and on the central metal. The redox properties of such MPcs may vary dependant on the nature of the solvent. In **Fig.1.3**, typical electrocatalytic process of an MPcs immobilized onto an electrode surface using the M^{2+}/M^{3+} redox couple is displayed.

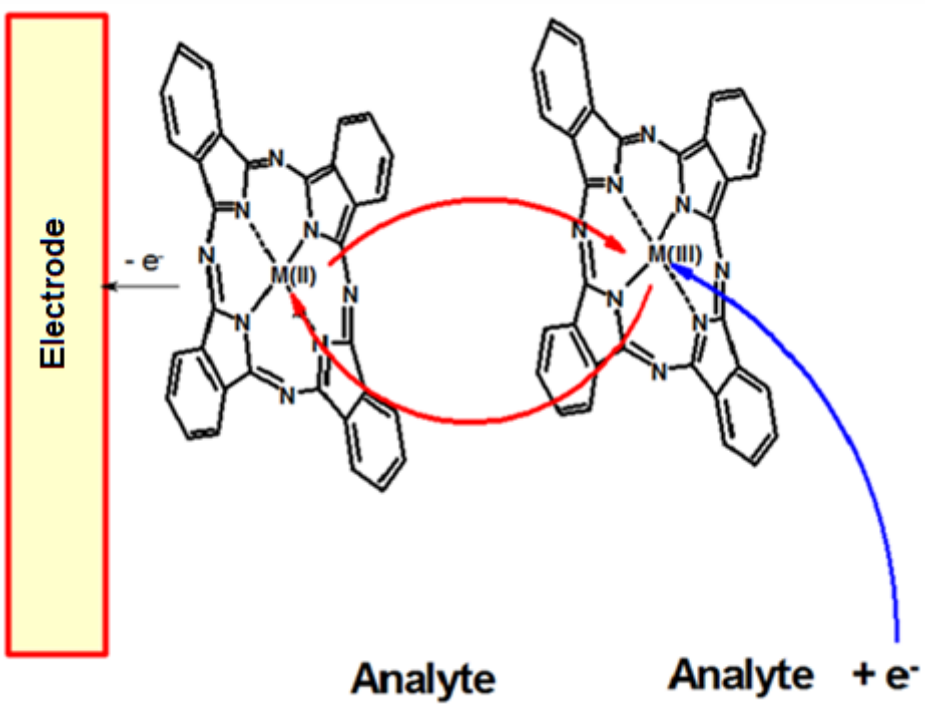

Fig.1.3 Scheme of a catalytic process promoted with MPcs based molecular electrode [**10**]

The catalytic process promoted by MPcs based molecular electrode can be via oxidation or reduction. In oxidation: the MPc is oxidized (**Eq 1.1**) at the electrode the

reduced back (**Eq 1.2**) upon interaction with the analyte. In reduction represented by (**Eq 1.3**) and (**Eq 1.4**) the sequence of reactions is reversed.

Oxidation

$$Co^{II}Pc \rightarrow [Co^{III}Pc]^{+} + e^{-} \qquad \textbf{(1.1)}$$

$$[Co^{III}Pc] + R \rightarrow Co^{II}Pc + P \qquad \textbf{(1.2)}$$

Reduction

$$Co^{II} + e \rightarrow Co^{I}Pc \qquad \textbf{(1.3)}$$

$$Co^{I}Pc + R \rightarrow Co^{II}Pc + P \qquad \textbf{(1.4)}$$

where, R and P are the reactant and products respectively. The electrocatalytic activity of an MPc modified electrode may be analysed using cyclic voltammetry. In electrocatalysis cyclic voltammetry has two characteristic properties, which show improved catalytic behaviour. In the presence of a catalyst (i) a shift in potential (V) towards less positive values for oxidation, less negative values for reduction for and (ii) increased catalytic currents for both oxidation and reduction occur. **Fig. 1.4** shows a CV diagram generated from an electrocatalytic reaction at an MPc modified electrode is displayed [**57**].

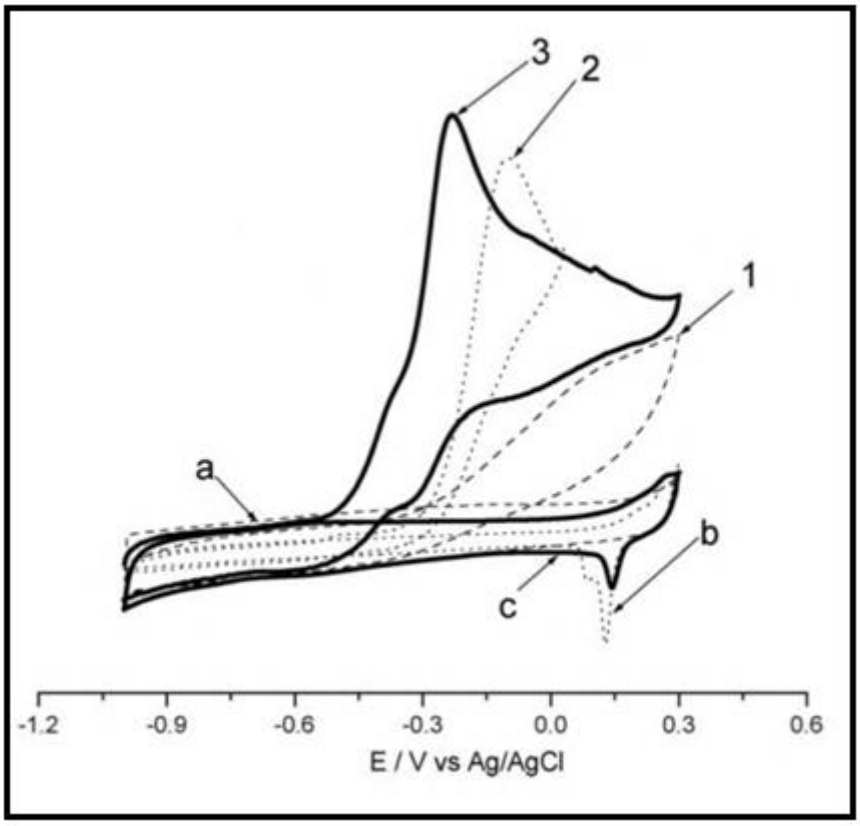

Fig 1.4 A glassy carbon electrode modified with SWCNT alone (1), CoPc alone (2) and CoPc/SWNT hybrids (3) run in the test analyte. Curves **a**, **b** and **c** show each of the mentioned curves respectively in buffer solution. SWCNT=Single walled carbon nanotubes [**57**]

1.4.2. Methods of electrode modification

Modification of an electrode can be achieved following various methods including adsorption, grafting, covalent anchoring and polymerisation, **Figure 1.5** [**58, 59**].The method for modification is strictly dependant on the purpose intended for the modified electrode.

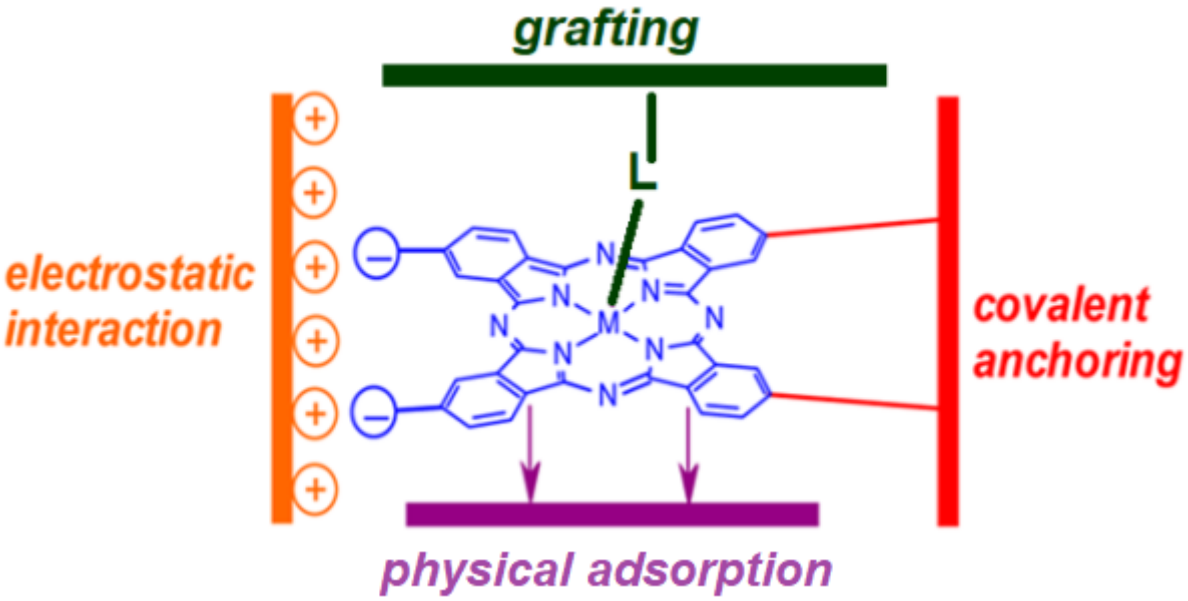

Fig 1.5 Schematic representation of electrode modification techniques using MPcs [**59**].

The electrodes used for modification may be from various materials such as metals (Pt, Au), carbon or semiconductors. Substrates for modification are usually chosen for their chemical and mechanical stability. Prior to modification, the electrodes are subject to pre-treatment which prepares their surface for modification. Pre-treatment may involve polishing or chemical and electrochemical procedures [**60**]. Herein, a glassy carbon electrode (GCE) was modified using the physical adsorption method also known as the drop and dry.

The drop and dry modification method is the most simple, easy and fast of all. It involves the dissolution of an electrocatalyst in an appropriate solvent followed by applying an aliquot of the solution onto an electrode. **Fig 1.6** shows immobilization of MPc onto a GCE using the drop and dry method. The electrode is then left to dry in an inert environment to achieve immobilization. The GCE was chosen because of its highly conductive surface, chemical inertness, low background currents and wide potential windows. As a result, stable layers of modifiers can attach to its surface in a controllable manner. In addition carbon materials are abundant and inexpensive [**61, 62**]. The relatively flat and aromatic structure of MPcs allows for adsorption onto the electrode surface.

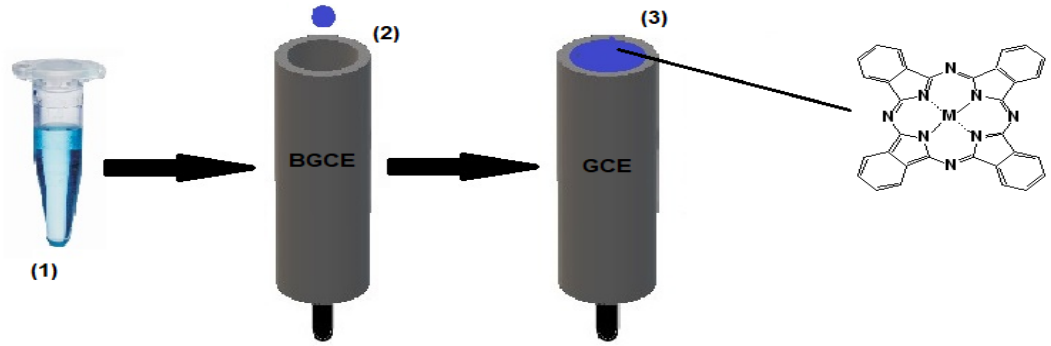

Fig 1.6 General procedure for drop and dry technique on a bare GCE. (**1**) Dispersion of MPc, (**2**) drop casting of MPc dispersion and (**3**) drying in an inert environment.

1.5. Analytes employed in this work

Hydrazine is used as a raw material for glass blowing and water cleaning agent and in the synthesis of medical drugs and agricultural products. However, hydrazine is toxic and corrosive as a result, its levels need to be monitored. Hydrazine has also been recognised as a carcinogen, which may result in liver and brain damage [**63, 64**].

The biggest challenge in the detection of many toxic compounds including hydrazine has been their occurrence at very low concentrations, which makes it almost impossible to detect. It is for this reason that the development of reusable, sensitive and stable sensors is of utmost need, as it is aimed by this thesis.

1.6. Summary of aims and objectives of this thesis

The focus of the work covered in this thesis is to controllably alter the glassy carbon electrode surface using the physical adsorption modification method. The electrode surface is modified and characterized using cyclic voltammetry to ensure that it has all the characteristics of an electrocatalytic sensor.

The present work is also aimed at investigating the electrochemical reactions; electron transfer and chemical reactions that occur at the surface. The effect of the catalysts on these reactions is investigated. Even further, the contribution of the structure of the catalyst, and the way in which the catalyst interacts with the analyte is investigated.

This work is aimed at enhancing the electrocatalytic oxidation of hydrazine by MPcs. The MPcs are combined with GQDs nanocomposites via covalent and non-covalent interactions. The electrocatalytic activity of MPcs as surface modifiers alone and as GQDs/MPcs hybrids is explored. For the first time the electrocatalytic activity of asymmetric MPcs in the presence of GQDs is explored. In summary the thesis aims at the following

1. Synthesis of novel complexes **1** and **4**, as well as the already known complexes **2** and **3**.
2. Synthesis of pristine GQDs,

3. Functionalization of the pristine GQDs by reduction (rGQDs) and amino-functionalization (NH_2GQDs) to alter and narrow band gap energy and hence improve conductivity and electron transfer abilities.
4. Non-covalent conjugation of complexes **1**, **2** and **3** to pristine GQDs to improve detection currents and limits.
5. Non-covalent conjugation of complex **4** to rGQDs and NH_2GQDs respectively,
6. Covalently link complex **4** to rGQDs and NH_2GQDs respectively and explore electrocatalytic activity.
7. Sequentially modify electrodes with layers of GQDs and MPcs
8. Investigate the kinetics occurring at nanocomposite catalyst/electrolyte interface during the electrocatalysis of hydrazine using cyclic voltammetry and chronoamperometry

Chapter 2:
Materials and Experimental

2. Materials and Experimental

2.1. Materials

The following chemicals were purchased from Sigma-Aldrich: Hydrazine hydrate,$K_4[Fe(CN)_6]$, $K_3[Fe(CN)_6]$, 1-ethyl-3-(3-dimethylaminopropyl) carbodiimide (EDC)**,** (N-hydroxysuccinimide) (NHS) and (N,N'-dicyclohexylcarbodiimide) (DCC), $CoCl_2.6H_2O$ and dialysis membrane (MW 1.5 kDa), Tetrahydrofuran (THF), methanol and 1-pentanol. Merck supplied the following: Dimethylformamide (DMF), 1, 8-diazabicyclo [5.4.0] underc-7-ene (DBU), dicyanobenzene and sodium hydroxide. Millipore water was obtained from Milli-Q Water Systems (Millipore Corp. Bedford, MA, USA). Stock solution (1 mM) hydrazine was prepared in 0.1 M sodium hydroxide. All other reagents and solvents used as received from commercial suppliers. The 4-(4-*tert*-butylphenoxy) phthalonitrile [**65**] and 4-(4-carboxyphenoxy) phthalonitrile [**66**] were synthesized following literature methods. The pristine GQDs were synthesized as reported in literature [**67, 68**]. Complexes **2** and **3** were synthesized as reported in literature [**17, 18**].

2.2. Equipment

Cyclic voltammetric and chronoamperometric data were obtained using Autolab Potentiostat PGSTAT 302 (Eco Chemie, Utrecht, The Netherlands) driven by the General Purpose Electrochemical System data processing software (GPES, software version 4.9). A three-electrode electrochemical cell made of a glassy carbon electrode (GCE) as the working electrode, platinum wire (Pt) as the counter electrode and silver|silver chloride wire (Ag|AgCl) as a pseudo-reference electrode was used. Scanning electrochemical microscopy (SECM) experiments were conducted using Uniscan equipment, model 370 and a 25 mm Pt ultra-microelectrode (UME) as the tip. Approach curve analysis was employed. The 25 mm Pt micro-electrode was used

together with a Pt counter electrode and Ag|AgCl wire as the pseudo-reference electrode. Changes were monitored using $K_3[Fe(CN)_6]$ oxidation at 0.29 V vs. Ag|AgCl. Glassy carbon plates (GCP, Good fellow, UK) were employed for SCEM. Transmission electron spectroscopy (TEM) images were obtained from Zeiss Libra TEM 120 Model operated at 90 kV.

Elemental analysis were done using a Vario-Elementar Microcube® ELIII while mass spectral data were collected on a Bruker® Auto FLEXIII smart-beam TOF/TOF mass spectrometer using α-cyano-4-hydrocinnamic acid as the matrix in the positive ion mode. X-ray photoelectron spectroscopy (XPS) analysis was done using an AXIS Ultra DLD, with Al (monochromatic) anode equipped with a charge neutraliser, supplied by Kratos Analytical. The following parameters were used: the emission was 10 mA, the anode (HT) was 15 kV and the operating pressure below 5×10^{-9} torr. A hybrid lens was used and resolution to acquire scans was at 160 eV pass energy in slot mode. The centre used for the scans was at 520 eV with a width of 1205 eV, steps at 1 eV and dwell time at 100 ms. The high resolution scans were acquired using 80 eV pass energy in slot mode. Infrared spectra were recorded on a Bruker® Alpha IR (100 FT-IR) spectrophotometer. A Bruker Vertex 70-Ram II Raman spectrometer (equipped with a 1064 nm Nd: YAG laser and liquid nitrogen cooled germanium detector) was used to collect Raman data. Dynamic light scattering (DLS) experiments were done on a Malvern Zetasizernanoseries, Nano-ZS90. Excitation and emission spectra were recorded on a Varian Eclipse spectrofluorometer. Ground state electronic absorption spectra was performed on a Shimadzu UV-2550 spectrophotometer. Atomic force microscopy (AFM) measurements in tapping mode were carried out with MFP-3D Origin supplied by Asylum research (Oxford instruments company, USA). Capillary Zone Electrophoresis (CZE) experiments were run on the Agilent Technologies 7100

Capillary Electrophoresis (ChimieParisTech Instruments, France). A Beckman eCAP capillary tube (50µm ID) with a total length of 35 cm was utilized. The distance between the injection point (capillary inlet) and detection point was at 26.5 cm. The UV detector was set at a wavelength of 214 nm. Experiments were carried out at a 25 ^{o}C while applying a voltage of 16 kV. The sample was introduced into the capillary tube by (30 mbar, 3s) injections. A phosphate buffer with pH was used as the background electrolyte (BGE). The BGE made from NaH_2PO_4 (0.1 M, 3.6 mL) and Na_2HPO_4 (0.1 M, 3.8 mL).The silanol capillary tube was activated using NaOH (1M) for 15 minutes, NaOH (0.1 M) for 15 min, water for 5 min and then lastly the BGE for 5 min.

2.3. Synthesis

2.3.1. Functionalization GQDs

2.3.1.1. Amino-functionalized GQDs (NH_2GQDs), Scheme 3.1

The post-fabrication modification of the pristine GQDs to form the amino functionalized NH_2GQDs was achieved following a novel approach via EDC-NHS coupling. The pristine GQDs were dissolved in water (6 mg/mL) to form a homogenous solution. To activate the carboxylic groups of the GQDs, EDC (0.17 mmol) and NHS (0.13 mmol) were added simultaneously to the GQDs solution and the mixture was left to stir for 24 h at room temperature. To perform the amino functionalization, ammonia solution (3 mL) was added. The resulting NH_2GQDs were precipitated out using ethanol. The particles were further subject to dialysis using a MW 1.5 kDA tube for 24 h to get rid of unreacted materials and salts.

2.3.1.2. Reduced GQDs (rGQDs), Scheme 3.2

Briefly, to a solution of the pristine GQDs (6 mg/mL) in water, hydrazine hydrate (500 µL) was added. The solution was left to stir for 12 h at room temperature. Ethanol was used to precipitate the nanoparticles and get rid of unreacted material. To achieve

absolute purity the nanoparticles were subject to dialysis for 24 h, and then washed and centrifuged at 20000 rpm for 15 min per cycle. A colour change from charcoal black to a light brown-beige colour was observed. The formed GQDs are represented as rGQDs and contain peripheral -NH_2 groups for linking.

2.3.2. CoPc derivatives

2.3.2.1. Monocarboxyphenoxy phthalocyanine (1), Scheme 3.3

A mixture of 4-(4-carboxyphenoxy) phthalonitrile (0.5 g, 1.91 mmol), anhydrous cobalt chloride 0.45 g, 3.46 mmol), dicyanobenzene (0.73 g, 5.697 mmol), 1-pentanol (3 mL) and DBU (0.2 mL) was refluxed for 7 h under argon. The product was allowed to cool down at room temperature. It was then washed with methanol, 1 M HCl and water successively. The obtained impure product was dissolved in a (3 mL) THF and chromatographed on Si_{60} column with MeOH/THF (5 % MeOH).

Yield: 57 mg (4.7 %), UV/VIS (DMSO) λ_{max}nm, (log ε): 325 (1.78), 595 (0.86), 665 (3.81). Elemental analysis Calc. for $C_{39}H_{20}CoN_8O_3.4H_2O$: C 60.08, H 3.62, N 14.37 Found: C 59.15, H 4.08, N 15.55. FT-IR [ATR] (v_{max}/cm^{-1}) 3344 (O-H stretch), 2988 (C-H aromatic), 1684 (C=N imine, C-N aryl), 1446 (C=C aromatic), 1230 (C-O-C), 1064, 956, 807, 708 (Phthalocyanine skeleton), MALDI-TOF MS m/z cal. For $C_{39}H_{20}CoN_8O_3$: 707.56, found 709.91 [M+2H]

2.3.2.2. Tris-(*tert*-butylphenoxy) monocarboxyphenoxy (4), Scheme 3.4

To 1-pentanol (3 mL), 4-(4-*tert*-butylphenoxy) phthalonitrile (150 mg, 0.543 mmol), 4, 4-carboxyphenoxy phthalonitrile (28 mg, 0.108 mmol), $CoCl_2.6H_2O$ (26 mg, 0.108 mmol), and DBU (0.1 mL) were added. The mixture was then refluxed at for 24 h under nitrogen atmosphere. The product CoPc (**4**) was precipitated out using 1:1 methanol and water. The product was dissolved in a minimum amount of chloroform, and was chromatographed on a Si_{60} column with chloroform/hexane (9:1) eluent to obtain the

desired second fraction. Several chromatographic separations were done on this fraction using 4:1 mixture of ethanol and chloroform to give the desired product, CoPc (**4**). Yield: 55 mg (43.8%) UV/Vis (DMF): λ_{max} (log ε), 674 (4.96), 613 (4.41). Elemental analysis Calc. for $C_{69}H_{56}CoN_8O_6$: C; 72.05, H; 5.71, N; 9.34, Found: C; 71.75, H; 5.64, N; 9.40.FT-IR [ATR]: (ν_{max}, cm^{-1}) 3071 (O-H stretch), 3001 (C-H aromatic), 2885 (C-H aliphatic). 1750 (-C=O), 1215 (C-O-C) 1044, 983, 872, 732 (Phthalocyanine skeleton). MALDI–TOF MS m/z: Calcd: 1152.15. Found: 1153[M+H].

2.3.3. MPc/GQDs conjugates

2.3.3.1. Non-covalently formed conjugates, Scheme 3.5(A & B)

Pristine GQDs were π-π stacked with three phthalocyanine complexes **1**, **2** and **3** to form Pc/GQDs conjugates. The conjugates were prepared following the procedure reported in literature [**69**] for adsorption of metallophthalocyanines onto carbon nanomaterials with a few modifications as follows: complexes **1** (3 mg, 0.0043 mmol), **2** (3 mg, 0.0027 mmol) and **3** (3 mg, 0.0027 mmol) were separately dissolved in DMF (2 mL), followed by addition to a GQDs solution (2 mg/mL) in water. The mixtures were then sonicated for 4 h at room temperature, and then left to stir overnight. The products represented as **1**(π)GQDs (shown in **Scheme 3.5A** as an example), **2**(π)GQDs and **3**(π)GQDs, were washed with ethanol and then dried under vacuum.

For complex **4**, rGQDs and NH_2GQDs were employed in order to compare with the covalently linked conjugates. The respective NH_2GQDs and rGQDs (5 mg/mL) were dispersed in water separately. A solution of **4** in DMF (0.00433 mmol, 2mL) was prepared. The complex **4** solution made was added to the respective GQDs solutions. The resultant mixtures were subject to sonication for 4 h at room temperature. The reaction was then left to stir for 48 h to form **4**(π)rGQDs (shown in **Scheme 3.5B** as an example) and **4**(π)NH_2GQDs conjugates. The conjugates were washed and

centrifuged with methanol:H_2O (1:1) to get rid of unreacted material, and dried at 70°C overnight.

2.3.3.2. Covalently formed conjugates (4@GQDs), Scheme 3.6

In two separate vials, solutions of complex **4** (0.0087 mmol, 5 mL) in DMF were added. To each vial, DCC (0.0048 mmol) and NHS (0.0048 mmol) were added to activate the carboxylic groups of complex **4**, the mixture was left to stir for 24 h. The functionalized GQDs (rGQDs and NH_2GQDs, 10 mg each) were then added to each of the vials separately. The mixtures were left to stir for further 24 h, resulting in the conjugates **4**@rGQDs and **4**@NH_2GQDs**, Scheme 3.6** (**4**@rGQDs used as an example). The resulting conjugates were precipitated and washed by centrifugation with methanol: H_2O (1:1) and dried at 70 °C overnight. Please note that π-π stacked conjugates represented with (π) while the covalent are represented with (@).

2.4. Electrode Modification

Glassy carbon electrode (GCE) was used as the working electrode, the silver|silver chloride (saturated potassium chloride) as the reference electrode and platinum wire as the counter electrode. The GCE was polished on a Buehler-felt pad using alumina (<10 μm). Between each polishing step, Millipore water and absolute ethanol were used to remove any impurity by sonicating for 5 min. The electrode was then rinsed with millipore water and dried before use. The GCE were modified via the drop dry method. Prior to the analyses, all the solutions were purged with argon/nitrogen gas to drive out oxygen and to ensure that there were no impurities prior the electrochemical measurements. The argon/nitrogen atmosphere was maintained throughout the analyses.

Publications

The results discussed in the following chapters have been presented in the articles listed below, that have been published or submitted for publication in peer-reviewed journals. These articles have not been referenced in this thesis:

1. M. Shumba, **S. Centane**, F. Chindeka, T. Nyokong, Nanocomposites of Sulphur-Nitrogen Co-doped graphene oxide nanosheets and Cobalt Mono Carboxyphenoxy Phthalocyanines for Facile electrocatalysis. *Journal of Electroanalytical Chemistry* 791(2017) 3648.
2. **S.Centane**, O. J. Achadu and T. Nyokong, Effects of Substituents on the Electrocatalytic Activity of Cobalt Phthalocyanines when Conjugated to Graphene Quantum Dots, *Electroanalysis* 29 (2017) 2470-2482
3. **S. Centane**, E. K. Sekhosana, R. Matshitse and T. Nyokong, Electrocatalytic activity of a push-pull phthalocyanine in the presence of reduced and amino functionalized graphene quantum dots towards the electrooxidation of hydrazine. *Journal of Electroanalytical Chemistry,* **accepted with revision**.

Chapter 3: Synthesis and Characterization

This Chapter deals with the synthesis, spectroscopic and microscopic characterization of the GQDs alone, CoPc complexes alone as well as the GQDs/CoPc conjugates.

3. Characterization

3.1. Functionalized GQDs

The functionalization of GQDs is essential for band gap manipulation [**70, 71**]. Pristine GQDs were modified with amino groups using ammonia following a novel EDC/NHS coupling mechanism to give the product NH_2GQDs (**Scheme 3.1**). The amino functionalization occurred mainly on the edges while retaining the typical GQDs structure with nitrogen doping.

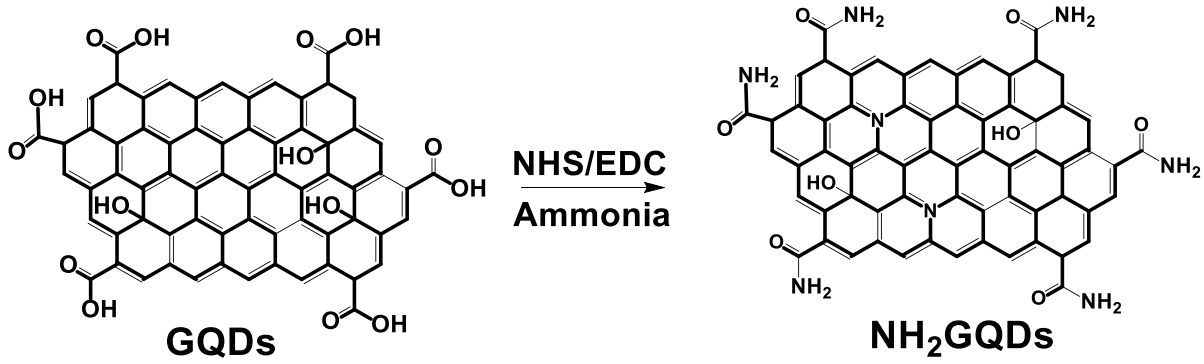

Scheme 3.1 Amino functionalization of pristine GQDs by ammonia

The reduction of GQDs reported herein followed procedures reported in literature **[72, 73]** with a few modifications, **Scheme 3.2**. Hydrazine proved to be viable for elimination of the excessive oxygen moieties and introduction of nitrogen containing groups. The lone pairs of the nitrogen atoms in the hydrazine molecule endow it with nucleophilic properties such that in the presence of an electrophile, interactions may occur. In the case of GQDs, a nucleophilic substitution reaction between the electrophilic carbon of the carboxylic group of GQDs and the nucleophilic nitrogen of the hydrazine occurred. This allowed for introduction of the nitrogen group edge functionalities. The alcohol groups were reduced to an alkene ensuring excessive elimination of the oxygen content. A few carbon atoms were replaced by nitrogen

atoms from hydrazine. The proposed schematic representation of the formed reduced GQDs (rGQDs) is shown below, **Scheme 3.2**.

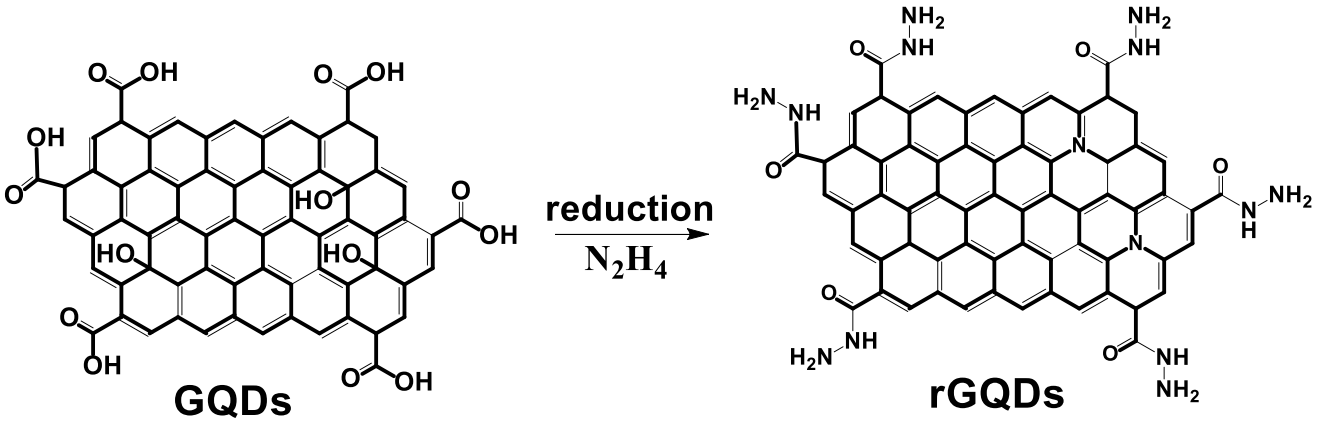

Scheme 3.2 Proposed structure of the rGQDs formed reduction of pristine GQDs by hydrazine.

3.1.1. FT-IR Spectroscopy

The functionalization of the GQDs was accompanied by structural changes when compared to the pristine GQDs. Pristine GQDs (**Fig 3.1A**) have their characteristic peaks –OH band (3250 cm^{-1}), C=O (1648 cm^{-1}) and C=C (1380 cm^{-1}). Upon reduction for rGQDs, strong intense $–NH_2$ (3550 cm^{-1}) and -C-N (1130 cm^{-1}) peaks were introduced, **Table 3.1**. These peaks serve as a confirmation of successful covalent interactions between the N_2H_4 and COOH groups of the GQDs. Furthermore, the presence of these groups on the IR data obtained is confirmation to the introduction of nitrogen containing groups onto the GQDs structure, (see **Fig 3.1B**). In addition, the disappearance of the hydroxyl broad peak and decrease in intensity of the carbonyl stretch serves as a confirmation to successful reduction and elimination of excessive oxygenated groups. New peaks for the NH_2GQDs were also observed; a 1204 cm^{-1} symbolic of a C-N bond formation and a broad peak with a shoulder at 3358 cm^{-1} representative of a primary amine, **Table 3.1**. The broadness at around 3000-3500 cm^{-1} may be as result of the overlap between the –OH stretch and $–NH_2$ peak. The

introduction of new functional groups onto the GQDs for both rGQDs and NH_2GQDs might indicate successful structural modification.

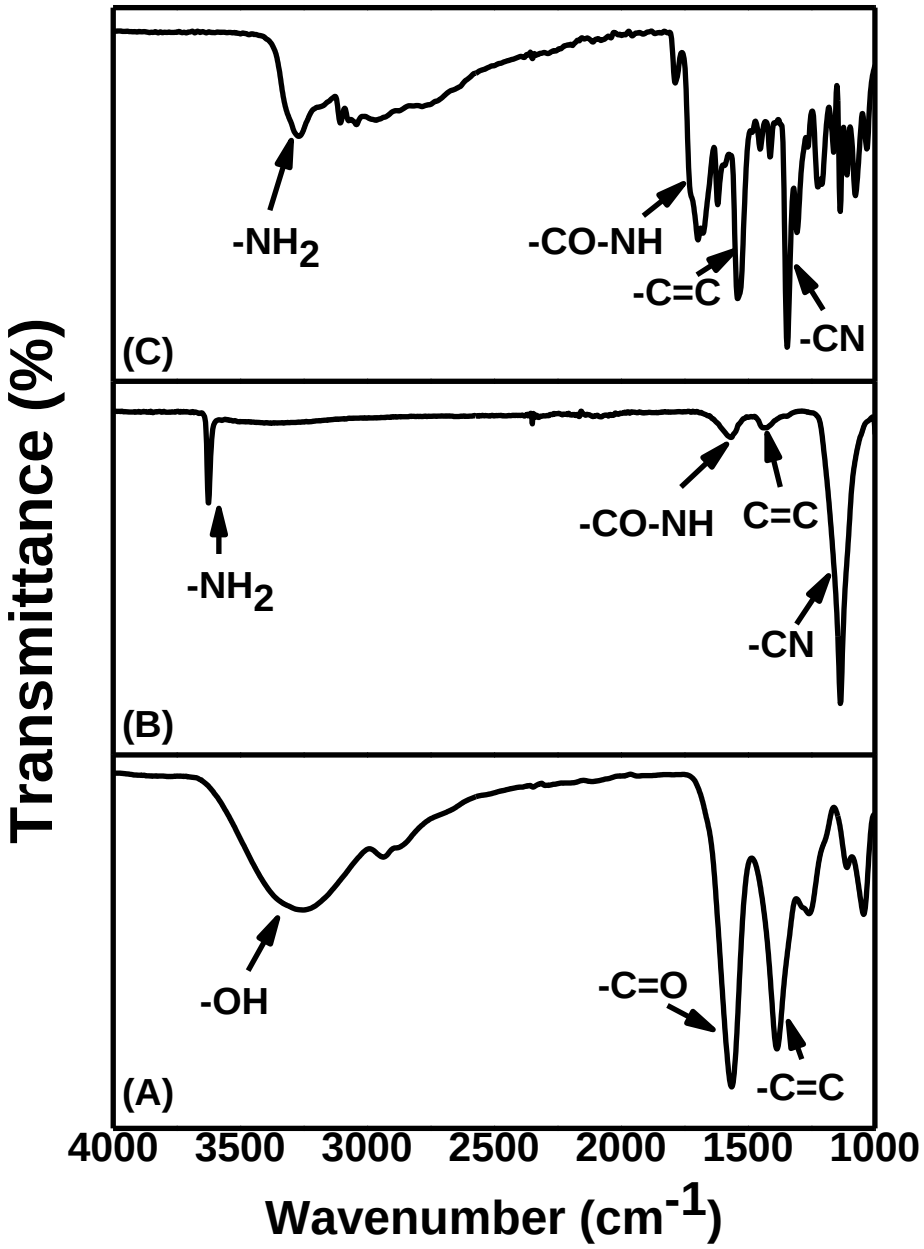

Fig 3.1 FT-IR spectra for (**A**) pristine GQDs, (**B**) rGQDs and (**C**) NH_2GQDs.

Table 3.1 FT-IR frequency (cm^{-1}) table of rGQDs, NH_2GQDs, **4**/GQDs hybrids

Stretch	**NH_2GQDs**	**rGQDs**	**4@rGQDs**	**4@NH_2GQDs**	**4(π)rGQDs**	**4(π)NH_2GQDs**
-CN	1204	1130	1115	1198	1103	1114
-NH_2	3358 (broad)	3550 (sharp)	-	-	3342	3522
-NH (amide)	-	-	3080	3060	-	-
-C=O	1638	1632	1722	1698	1623	1625
C=C	1503	1578	1623	1625	1608	1598
-OH	3023	-	-	-	3296	3285

3.1.2. Raman Spectroscopy

Fig 3.2 shows the Raman spectrum of the pristine GQDs compared to that of the functionalized rGQDs and NH_2GQDs. GQDs have two characteristic Raman peaks known as the G-band and D-band. The G-band corresponds to the (sp^2) tangential mode while the D-band corresponds to the (sp^3) breathing mode and is due to defects [**74**]. The D band and G band for pristine GQDs were located at 1350 $cm^{-1}$and 1590 cm^{-1} respectively. A shift to higher values for both the D and G bands was observed for the rGQDs, while no change was observed for the NH_2GQDs. The shifts in the Raman of the rGQDs may be attributed to structural distortions caused by the different bond distances of C-C and C-N [**75**], as well as the intense elimination of the oxygen containing functionalities. The data obtained from the Raman spectroscopy allows for assessment and quantification of any structural defects occurring upon modification. The structural defects can be quantified using the ratio of the intensities of the D and

G-band (I_D/I_G). Intense modification is accompanied by introduction of defects, and as a result upon modification an increase in the I_D/I_G is expected. The I_D/I_G ratio increased from 0.13 for pristine GQDs to 0.18 for NH_2GQDs, suggesting higher defects and disorders from decoration of GQDs with the amino groups. However, the I_D/I_G ratio of rGQDs was the highest (0.21) amongst the three GQDs, showing the highest defects and disorders, **Table 3.2**. This may be because upon reduction, there was elimination of various groups (-OH, -COOH) on the core and introduction of new edge groups (C-N-NH_2) which resulted in the disruption of the sp^2 carbon framework. Similar trends have been observed previously for functionalized GQDs [**76, 77**].

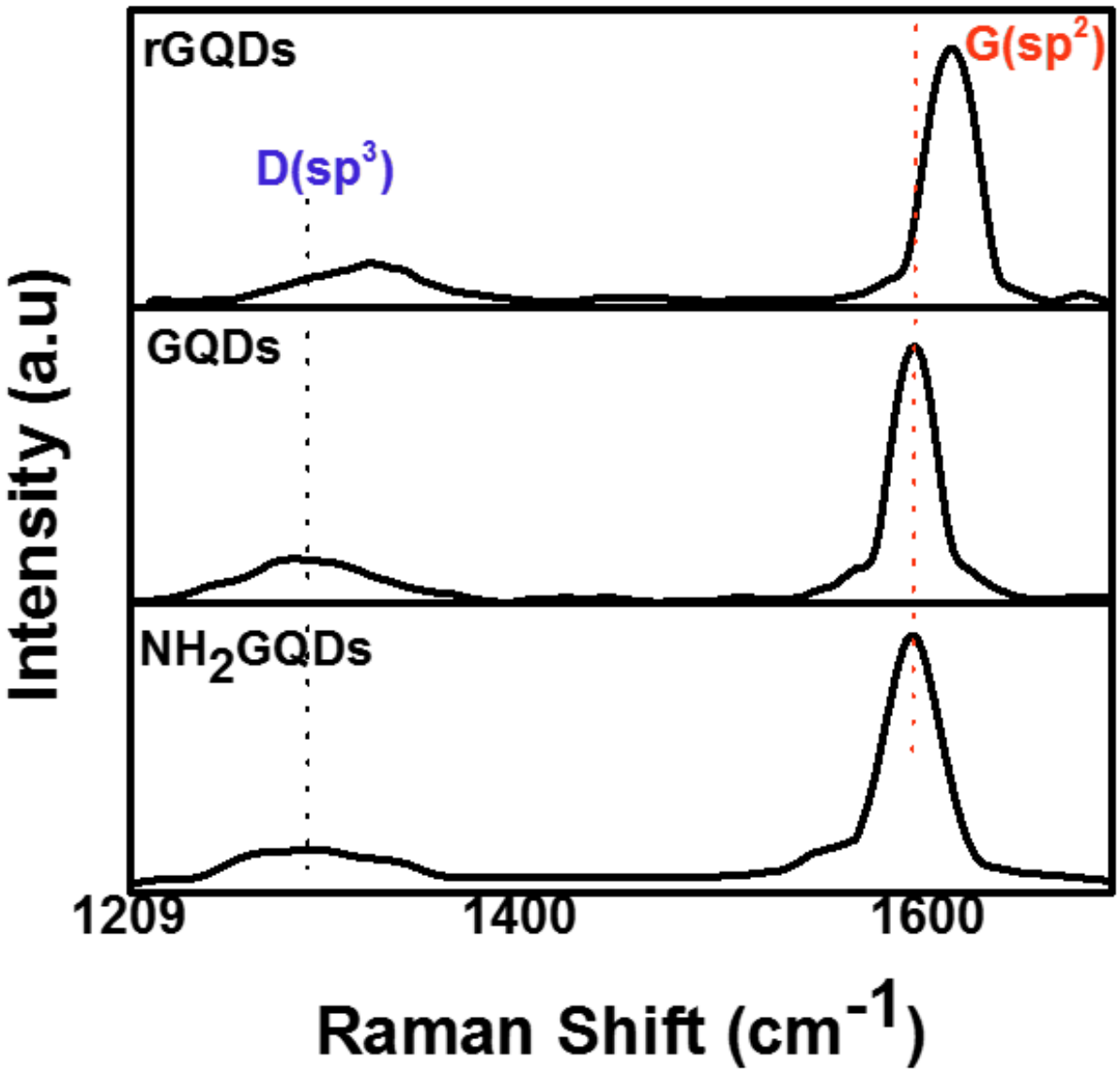

Fig 3.2 The Raman spectra of pristine GQDs, NH_2GQDs and rGQDs in water.

Table 3.2 Spectroscopic parameters of the synthesized GQDs, CoPc derivatives and CoPc/GQDs conjugates

Samples	**λ[a] (nm)**	**DLS size (nm)**	**Raman (I_D/I_G)**
GQDs	450	2.4	0.13
rGQDs	410	3.2	0.18
NH_2GQDs	403	2.8	0.21
1	665	-	-
2	656	-	-
3	680	-	-
4	670	-	-
1(π)GQDs	660	15	0.19
2(π)GQDs	672	18	0.19
3(π)GQDs	680	21	0.19
4(π)rGQDs	672	11.2	0.23
4(π)NH_2GQDs	670	8.2	0.20
4@rGQDs	664	10.4	0.58
4@NH_2GQDs	666	7.1	0.44

[a]emission for GQDs, Q band for Pcs and conjugates

3.1.3. UV-Vis Spectroscopy

Fig 3.3 shows the UV-Visible absorption and emission spectra for (A) pristine GQDs and (B) NH_2GQDs as examples. Broad absorption spectra were observed for all GQDs. The NH_2GQDs and rGQDs (the latter not shown) showed similar absorbance spectra due to bonding and anti-bonding molecular orbitals of both the C=C sp^2 and amino edge functionalities [**71, 78**]. The emission of the pristine GQDs at 450 was shifted to 410 and 403 for NH_2GQDs and rGQDs respectively, **Table 3.2**. The shift may be attributed to introduction of surface defects onto GQDs upon functionalization (reduction and amino-functionalization) **[79]**.

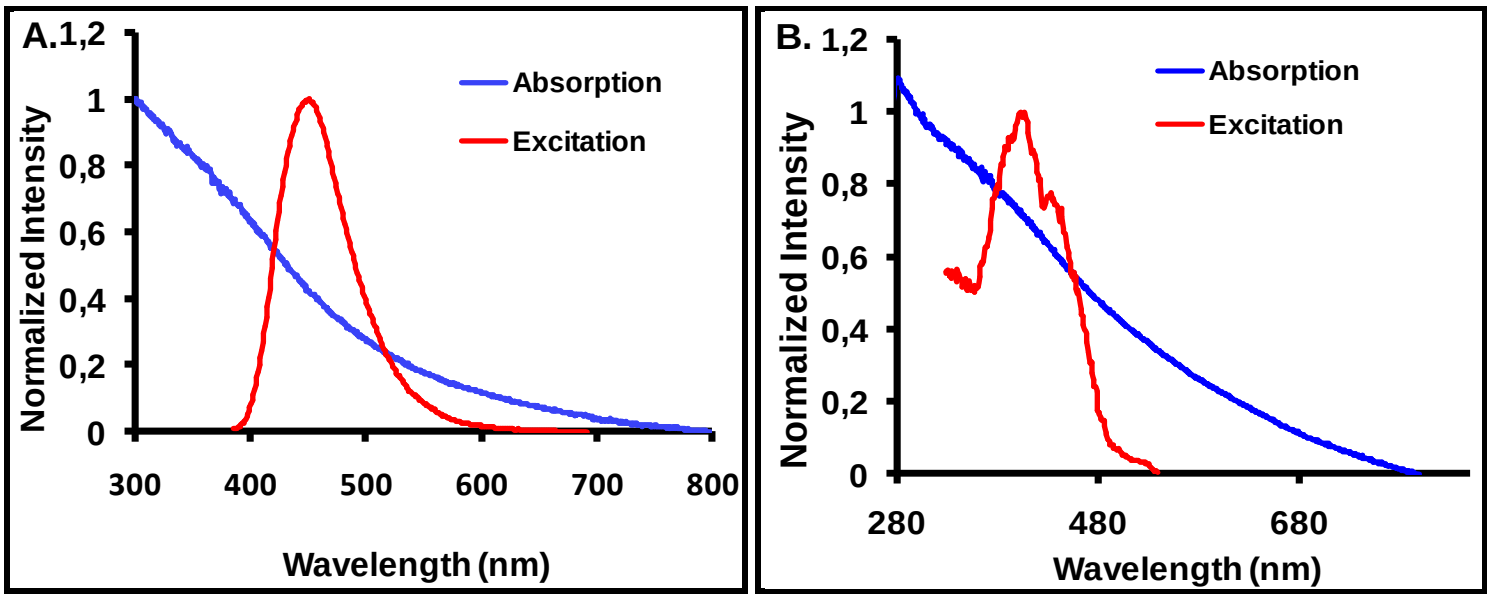

Fig 3.3 Absorption and emission spectra of (**A**) pristine GQDs and (**B**) NH_2GQDs recorded in water.

3.1.4. Atomic Force Microscopy (AFM)

Figure 3.4 shows the AFM data of pristine GQDs as an example. The AFM topography for pristine GQDs revealed sizes between 0.5-1.5 nm corresponding to 1-2 sheets of graphene [**80**]. The functionalized rGQDs and NH_2GQDs had topographic heights less

than 1 nm were obtained, with the average heights ca. 0.3-0.5 nm suggesting monolayer graphene sheets.

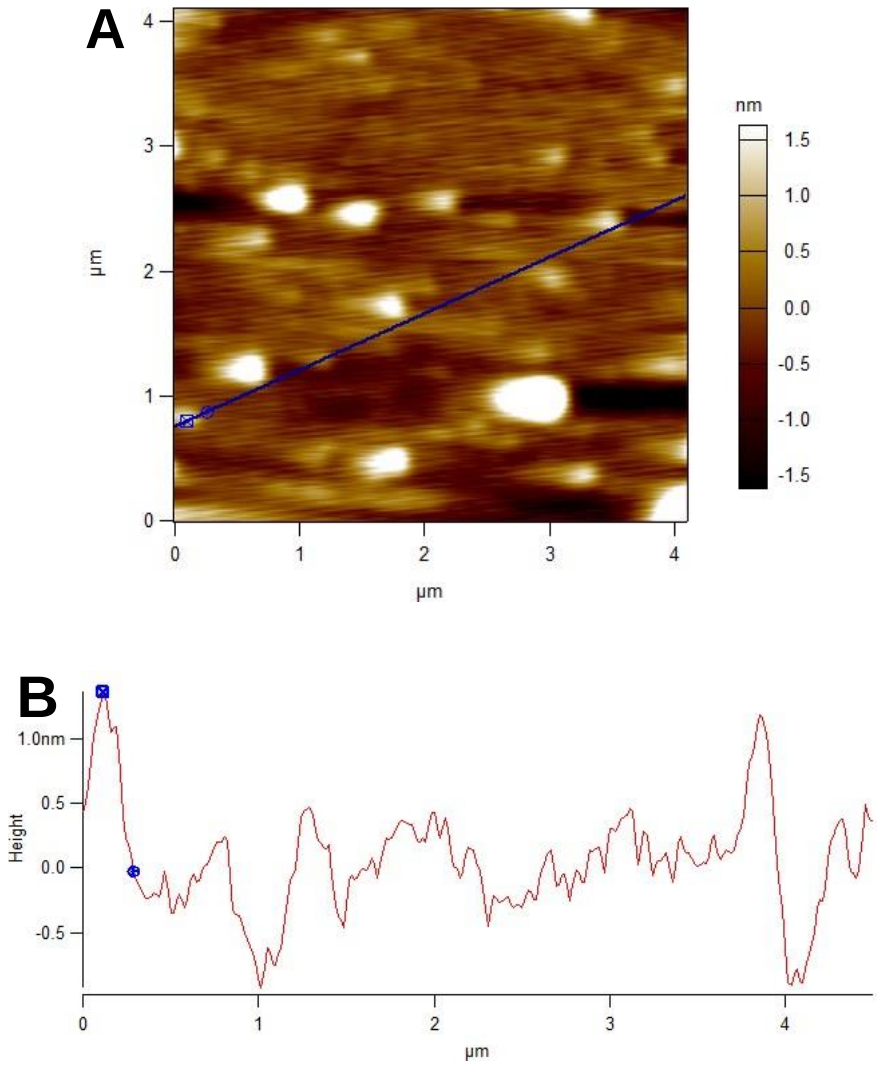

Fig 3.4 AFM topographic profile (**A**) and section graph (**B**) for pristine GQDs.

3.1.5. X-ray Diffraction (XRD)

In **Fig 3.5** the XRD patterns obtained for the synthesized GQDs are shown, using GQDs and rGQDs are used an example. The GQDs composites synthesized in this work showed a broad amorphous peak 2θ = 17 - 22° corresponding to the (002) due to the Bragg's reflection of the carbon in the graphene layers [**81**]. The calculated d-spacing for the GQDs, rGQDs and NH_2GQDs obtained were 4.25 (at 2θ = 21.1), 4.65

(at 2θ = 19.1) and 5.06 (at 2θ = 17.5) respectively. The varying d-values may be associated with the variation in surface functionalities of the GQDs where upon modification, the introduction of bulkier groups might have resulted in enhanced interlayer distance (**Scheme 3.1 and 3.2**).

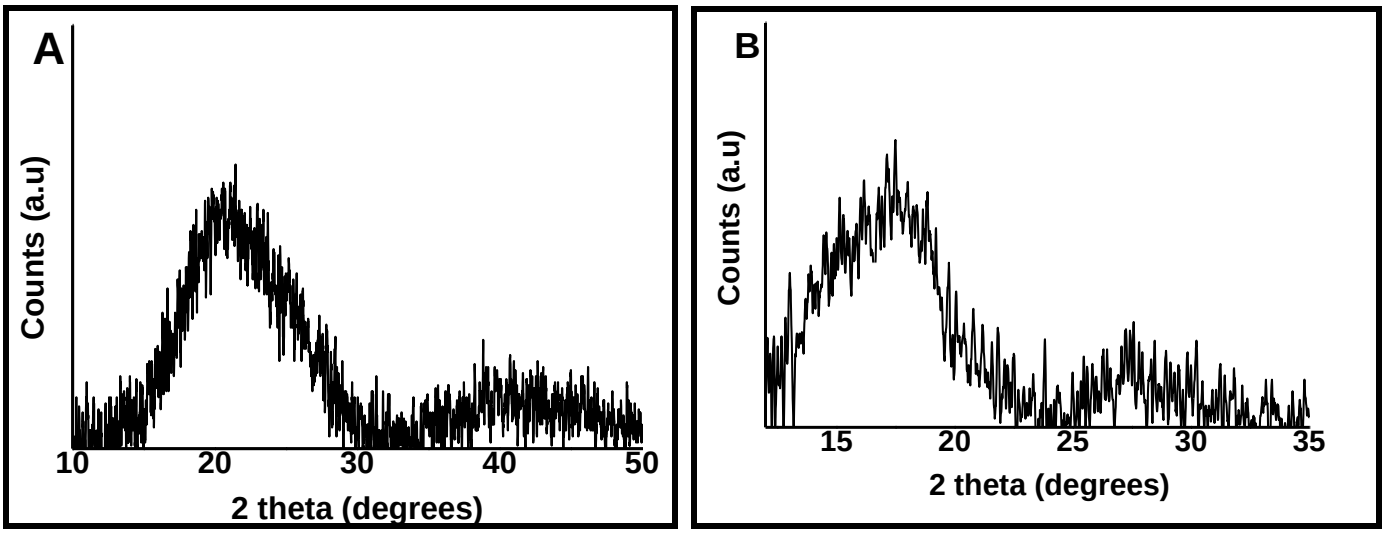

Fig 3.5 XRD patterns for pristine GQDs (**A**) and NH_2GQDs (**B**)

3.1.6. X-ray Photoelectron Spectroscopy (XPS) Analysis

To further probe the chemical composition of all the synthesized GQDs XPS characterization was carried out. The wide scans for rGQDs and NH_2GQDs are shown in **Fig 3.6(a, b)**. The XPS shows graphitic C1s and O1s peaks ca. 285 eV and 532 eV respectively, for all GQDs synthesized. An additional N1s peak for rGQDs and NH_2GQDs was observed. The chemical environment and type of nitrogen present in the GQDs is shown in the N1s high resolution spectra **Fig 3.6(c, d)**. The N1s spectra of the NH_2GQDs and rGQDs showed peaks; C=N, C-N, -NH_2, N-C=O and C-N^+ (for rGQDs only). The -NH_2 peak serves as a confirmation to successful amino functionalization of the NH_2GQDs. The presence of the C=N peaks indicate ring substitution of C atom by nitrogen atoms during modification. It can also be concluded that rGQDs were successfully functionalized with amino groups on the edges as

intended due to the presence of the –NH_2 peak. The C:O atomic ratio for pristine GQDs is 1.72, whereas the ratio for NH_2GQDs and rGQDs was 3.03 and 4.55 respectively, **Table 3.3**. This increase in C:O may be as a result of elimination of oxygenated species during modification. The obtained C1s high resolution spectra (**Fig 3.6(e, f)**) demonstrate the change in the carbon chemical environment from pristine GQDs to rGQDs and NH_2GQDs. The C1s spectra for pristine GQDs was deconvoluted in to four peaks; C=C (284 eV), C-C (283 eV), C-O (287 eV) and HO-C=O (289 eV) functional groups. Compared to the pristine GQDs, additional C-N (284 eV), C=N (282 eV, 284 eV) and O=C-NH (288 eV) peaks were observed for both NH_2GQDs and rGQDs (shown as an example in **Fig 3.6**). This new peaks suggest introduction of nitrogen containing functional groups on the structure of the GQDs during modification. The obtained data allows for conclusions on the successful amino functionalization and reduction of pristine GQDs to form NH_2GQDs and rGQDs.

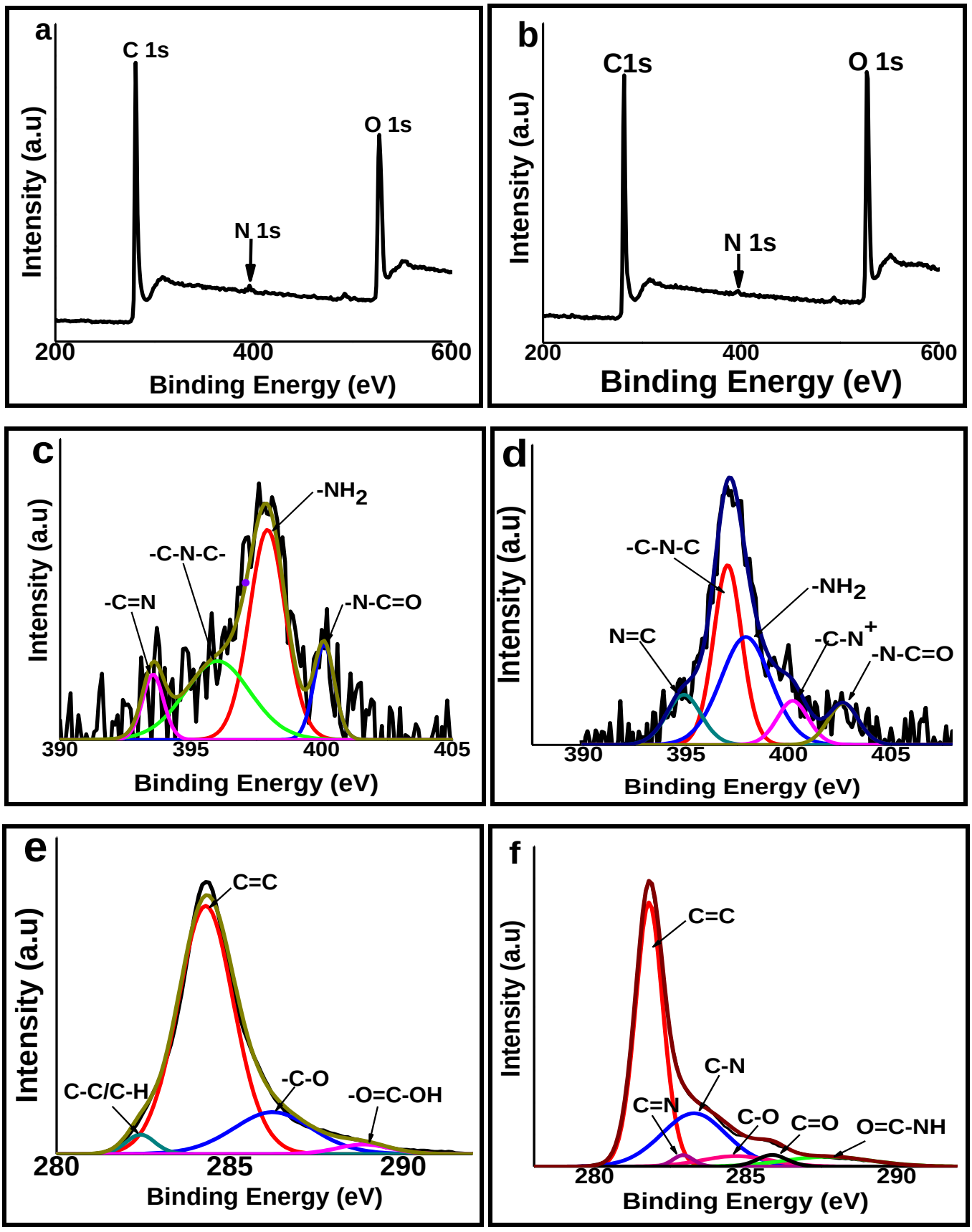

Fig 3.6 Wide scan for (**a**) rGQDs and (**b**) NH_2GQDs, (**c, d**) N1s spectra NH_2GQDs and rGQDs, (**e, f**) shows C1s spectra of pristine GQDs and rGQDs.

Table 3.3 XPS analysis results for pristine GQDs, NH_2GQDs and rGQDs.

Samples	C/O ratio	N (atomic %)	O=C-NH Intensity (au)
GQDs	**1.72**	**0.00**	**-**
NH_2GQDs	**3.03**	**1.12 (396 eV)**	**1027**
rGQDs	**4.55**	**1.61 (397 eV)**	**1909**
4@NH_2GQDs	**6.36**	**4.90 (398 eV)**	**1135**
4@rGQDs	**13.10**	**7.30 (398 eV)**	**2202**

3.1.7. Capillary Electrophoresis: UV detection

In this work pristine GQDs were characterized using capillary zone electrophoresis (CZE). The CZE technique differs from conventional electrophoresis in that it takes place in the confines of a tube. The technique separates ions based on their electrophoretic mobility; which greatly depends on the charge of the molecule and viscosity under the influence of an electric field **[82, 83]**. The tube is usually connected to a cathode and an anode at both ends as shown in **Fig 3.7.**

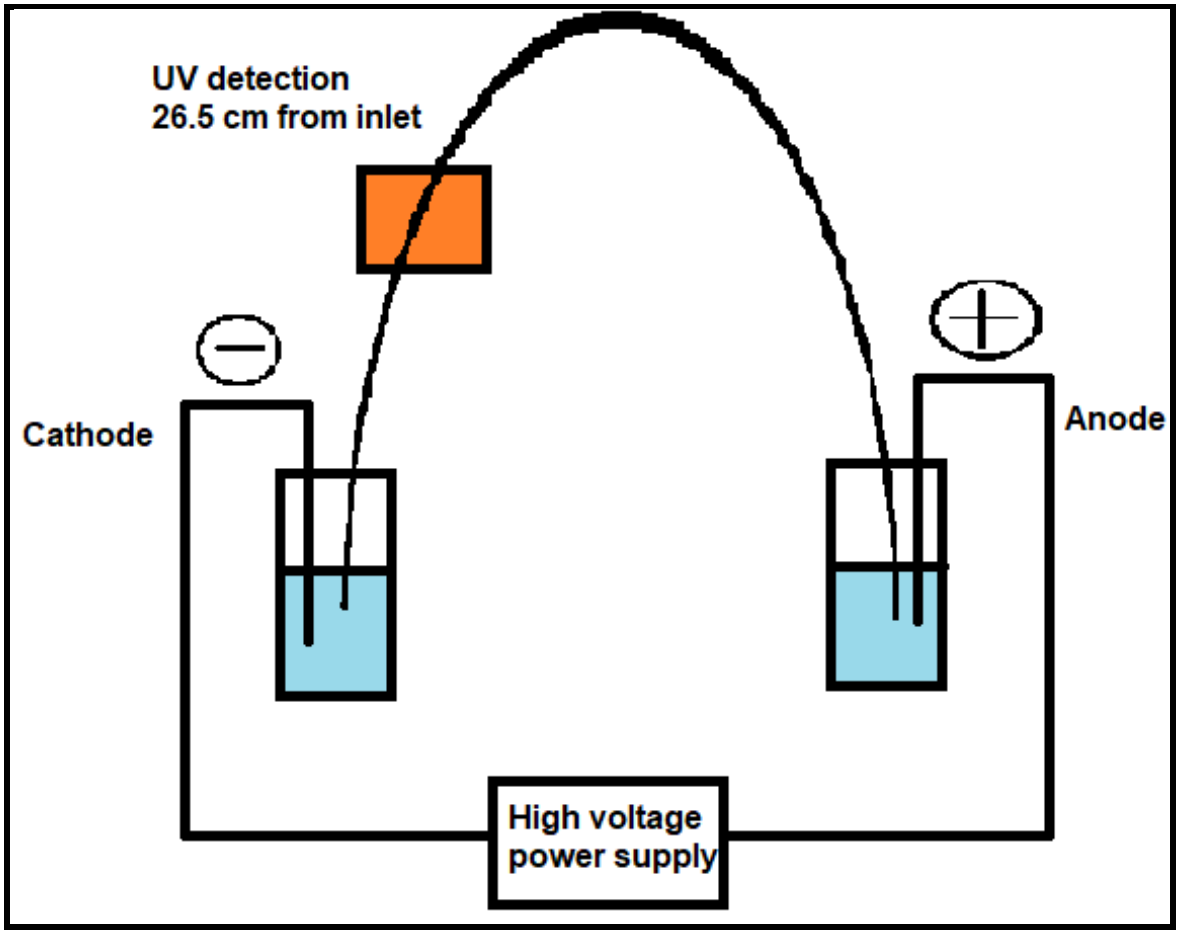

Fig 3.7 A schematic representation of a capillary electrophoresis system.

The direction of flow of the particles is determined by the charge carried by the species under analysis. The technique can be run either in positive mode or negative mode. The positive mode is used for positively charged species such that the inlet is at the anode (+ve) and species flow towards the cathode (-ve). The reverse is observed for the negative mode. GQDs are particles with a negative surface charge; the zeta potential (ζ) of the GQDs in water was -16.3 eV. The negative value of the zeta potential is owed to the presence of carboxyl and alcohol groups on the surface of the GQDs. As a result the electrophoretic measurements were run in the reversed/negative mode.

Figure 3.8a shows UV detection of just the background electrolyte (BGE) and the natural marker (DMF). The natural marker is used to mark the peak of the sample relative to its known position. The background electrolyte on the other hand conducts the transportation of current and separation of the analyte as well as assists in maintaining a constant pH **[84]**. A neutral sodium phosphate BGE was used to prevent any interferences of the electrolyte on the separation of the charged species. **Fig 3.8b** shows the presence of the analyte by an extra peak in addition to that of the natural marker. The migration time obtained in negative mode was 4.853 min. The results were in agreement with those obtained in positive mode plus external pressure, where the migration time obtained was 10.469 min which is about the same time from the end except in reverse. The presence of the GQDs peak in negative mode further confirms that GQDs indeed carry a negative surface charge. The fact that there were no other peaks except that of the natural marker (DMF) and the GQDs proved that the GQDs contained no impurities or unreacted material.

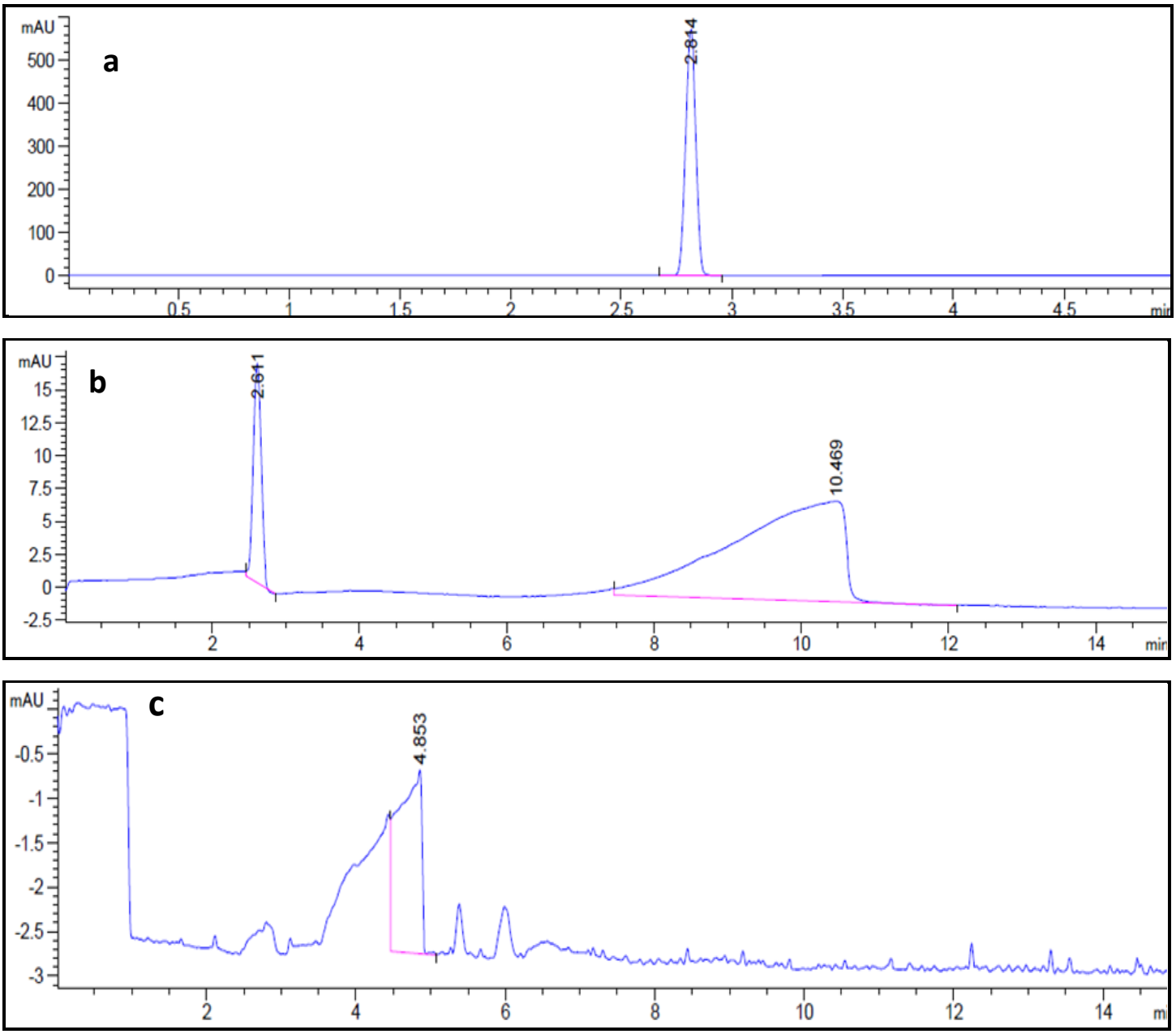

Fig 3.8 (**a**) Electrophoretic data obtained from just the natural marker, (**b**) electrophoretic data of GQDs in positive mode with an external pressure of 20 mbar and (**c**) electrophoretic data of GQDs in negative mode.

3.2. Synthesis and Characterization of Metallophthalocyanines

3.2.1. Synthesis

Complexes **2** and **3** are known while **1** and **4** are reported herein for the first time. Complexes **1** and **4** were synthesized following **Scheme 3.3** and **Scheme 3.4**.The complexes are soluble in DMF and $CHCl_3$ respectively. The statistical approach was followed for the synthesis of both complexes **1** and **4**. The mass spectra values 709 and 1153 mass units were obtained for complex **1** and **4**, respectively. The FT-IR spectrum of complex **1** displayed peaks 3344 cm^{-1} (O-H stretch), 2988cm^{-1} (C-H aromatic), 1684 cm^{-1} (C=N imine, C-N aryl), 1446 cm^{-1} (C=C aromatic) and 1230 cm^{-1} (C-O-C). The IR data for **4** displayed peaks 3071 cm^{-1} (O-H stretch), 3001 cm^{-1} (C-H aromatic), 2885 cm^{-1} (C-H aliphatic), 1750 cm^{-1} (-C=O), 1215 cm^{-1} (C-O-C). Chromatography on a Si_{60} column was employed to obtain desired products. FT-IR, mass spectroscopy and elemental analysis gave expected results for both complex **1** and **4**. NMR spectrum was not recorded due to the paramagnetic nature of the cobalt central metal.

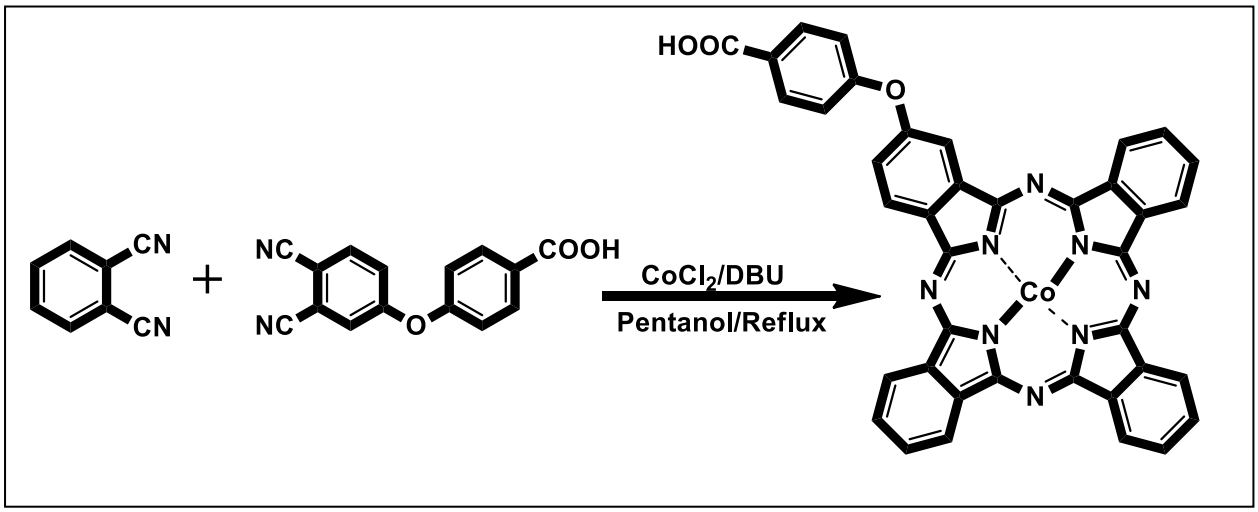

Scheme 3.3 Synthesis of cobalt monocarboxyphenoxy phthalocyanine (**1**).

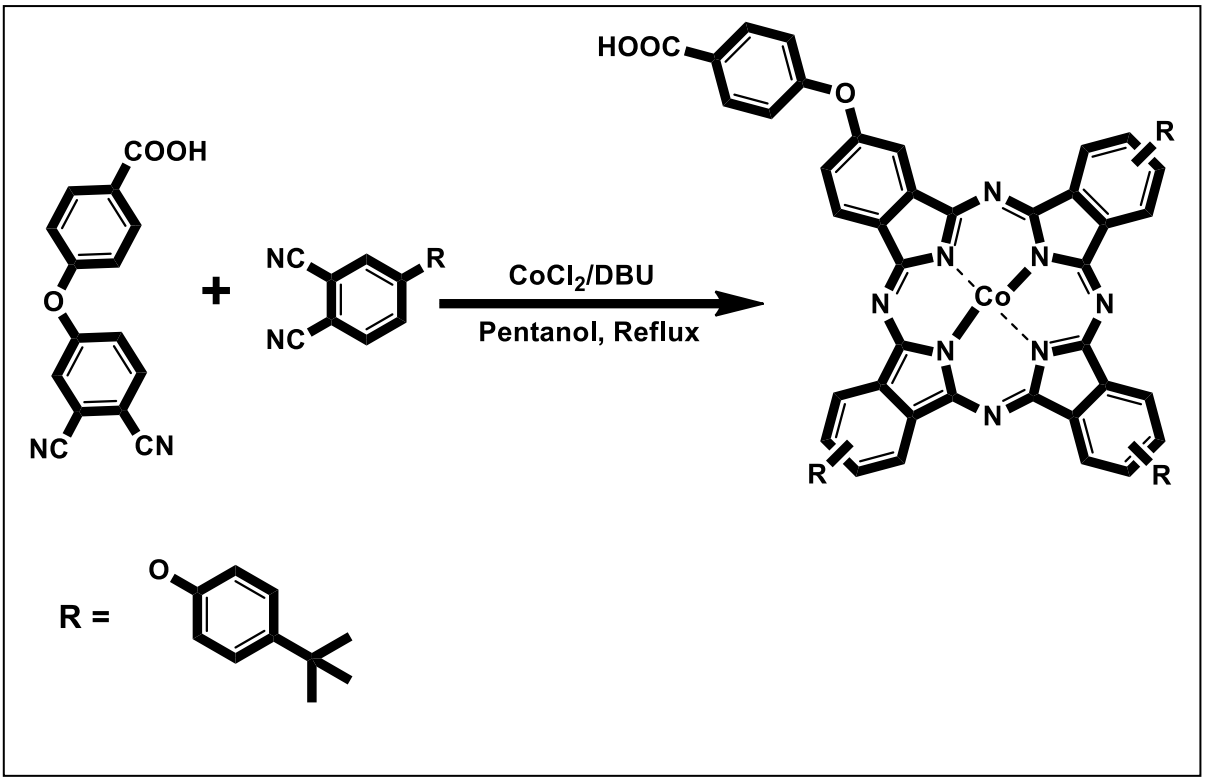

Scheme 3.4 Synthesis of cobalt tris-(*tert*-butylphenoxy) monocarboxyphenoxy phthalocyanine (**4**).

3.2.2. Characterization

The ground state electron absorption spectrum of **1** is shown in **Fig 3.9A**. The obtained spectrum exhibits the characteristic Q-band (665 nm) **Table 3.2**, a vibronic band (618 nm) and Soret band (349 nm) for a phthalocyanine. Similar peaks were observed for **4** as well; a Q-band (670 nm) **Table 3.2**, vibronic band (618 nm) and soret band (330 nm), **Fig 3.9B**. The bathometric shift (5 nm) of **4** compared to **1**, may be attributed to the push-pull structure of **4** which affects the electron density and distribution around the Pc. The HOMO-LUMO gap in **4** is more narrowed than in **1** and hence the spectroscopy of **4** is red shifted compared to **1**. The single Q-band observed for both phthalocyanines is typical of metallated phthalocyanines [**85**].

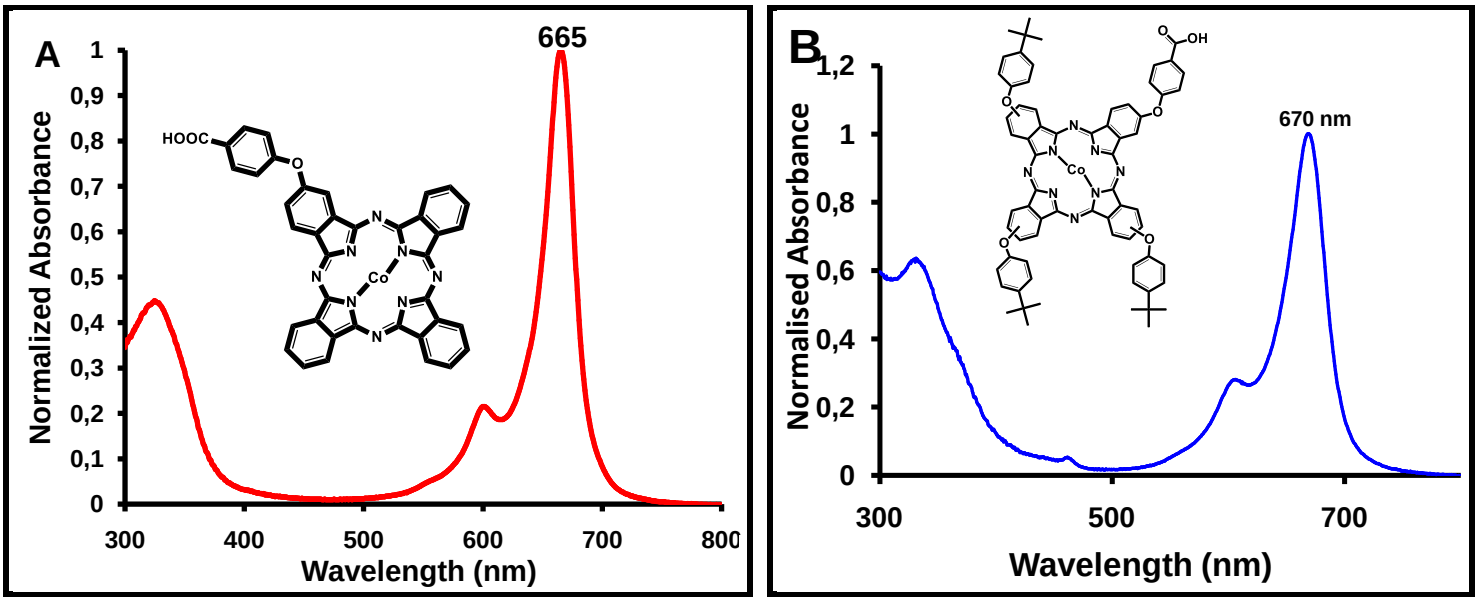

Fig 3.9 UV-Vis spectra of (**A**) 8×10^{-6} M of complex **1** and (**B**) 1×10^{-5} M of complex **4** in DMF. Insert = Molecular structure.

3.3. MPc/GQDs conjugates

Pristine GQDs were π-π stacked with three different Pc complexes **1**, **2** and **3**. The conjugates were formed using sonication at room temperature. The resulting products **1**(π)GQDs, **2**(π)GQDs and **3**(π)GQDs were washed with ethanol to remove excess unreacted material and dried under vacuum. A schematic representation of the MPc/GQDs π-π interaction is shown in **Scheme 3.5A** (showing **1**(π)GQDs as an example). Following the amino-functionalization and reduction of pristine GQDs to form NH_2GQDs and rGQDs, π-π stacked conjugates with Pc complex **4** were formed in order to compare with covalently linked **4**@GQDs conjugates. The resultant conjugates **4**(π)rGQDs and **4**(π)NH_2GQDs were formed by sonication at room temperature**, Scheme 3.5B** (using **4**(π)rGQDs as an example). The products were washed with MeOH: H_2O (1:1) to remove unreacted material and were dried at 70 °C overnight.

The functionalized rGQDs and NH_2GQDs were designed such that they have peripheral amino groups (**Scheme 3.1 & 3.2**) viable for covalent linking to the carboxylic end of the Pc complex **4**. The carboxylic terminal of the complex **4** was activated using the DCC/NHS coupling to form an amide linkage with the respective GQDs. The covalent linkage of rGQDs to complex **4** to form **4**@rGQds is depicted in **Scheme 3.6** as an example.

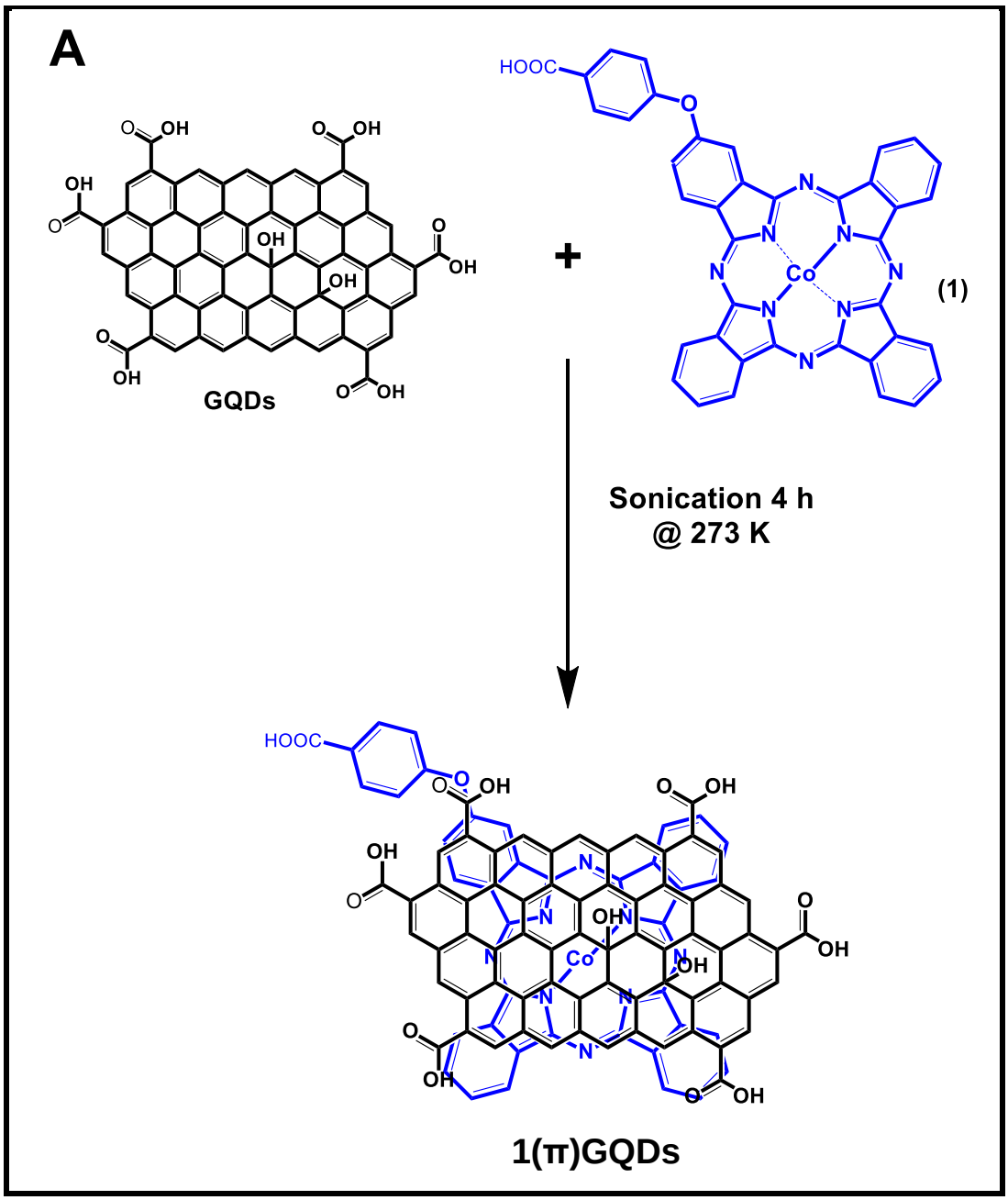

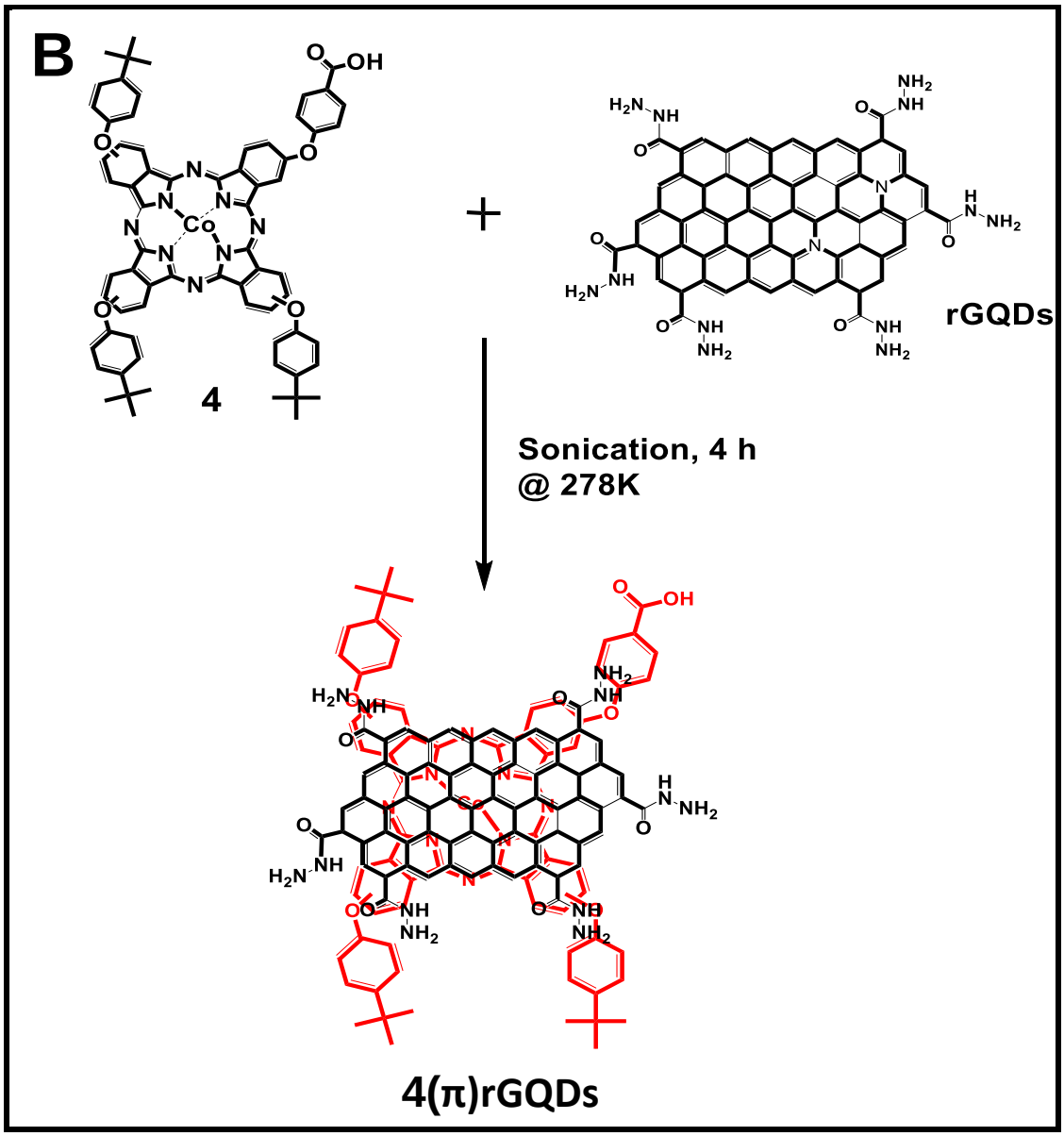

Scheme 3.5 Schematic representation of the approach toward the formation of **1**(π)GQDs (**A**) and **4**(π)rGQDs conjugate (**B**).

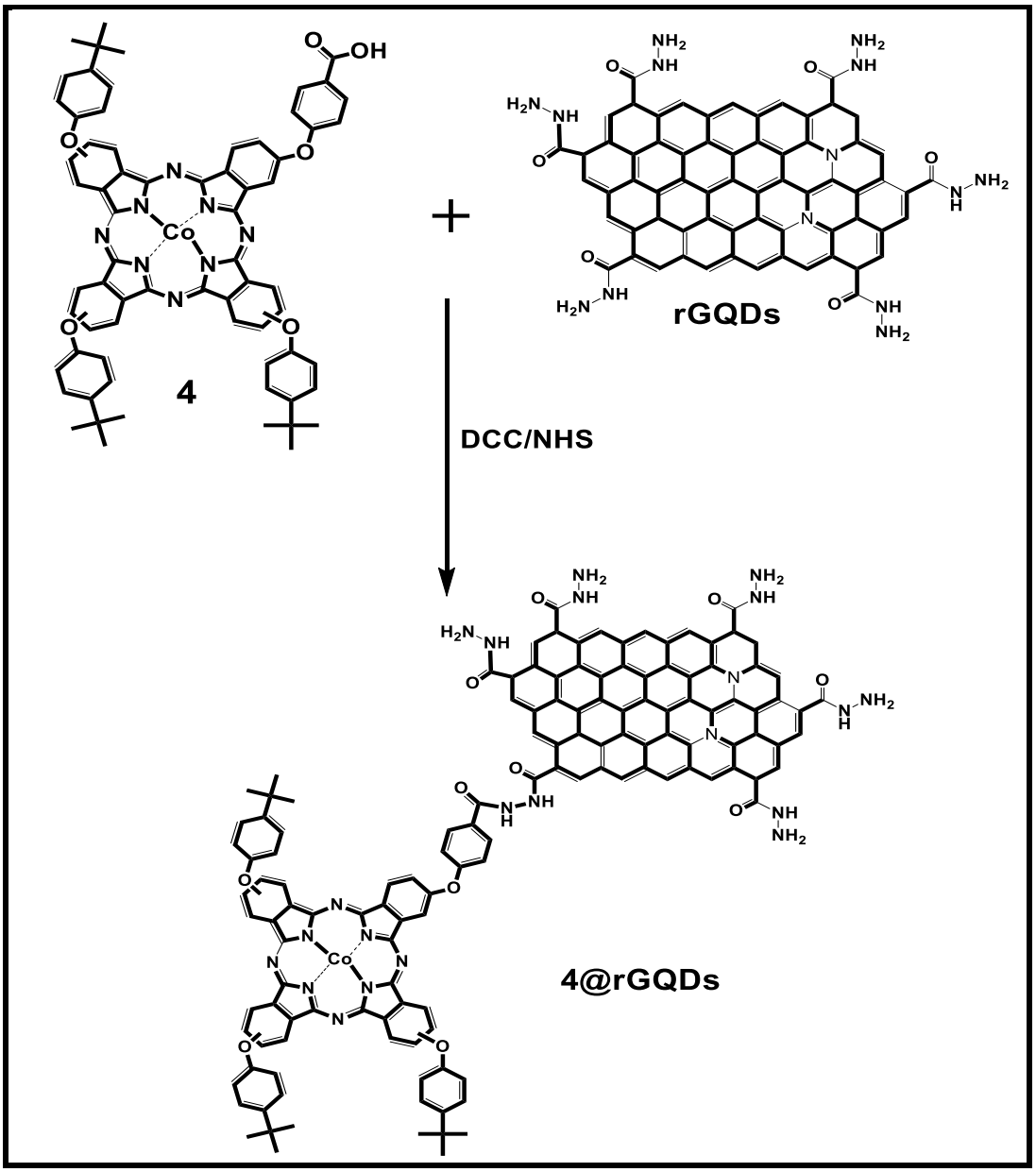

Scheme 3.6 Schematic representations of the **4**@rGQDs conjugate synthetic approach.

3.3.1. UV-Vis spectra

The UV-Vis absorption spectra of the various conjugates are shown in **Fig 3.10((A)-(D))**. The conjugates spectra are plotted against the respective Pc for comparison

purposes. There is a blue shift of the Q band for **1**(π)GQDs compared to complex **1** alone, **Fig 3.10A**, while there is a red shift for **2**(π)GQDs compared to complex **2** alone, **Fig 3.10B** and no shift for complex **3**(π)GQDs, **Fig 3.10C**. Red shifts and flattening of similar macrocycles such as porphyrins have been observed in porphyrins-graphene oxide nanoconjugates **[86]**. Blue shifts in UV-Vis spectra have also been reported for porphyrin-graphene oxide conjugates and were attributed to strong interaction between the two **[87]**. Both complexes **1** (monocarboxyphenoxy) and **2** (teracarboxyphenoxy) contain the same substituents but the Q band is blue-shifted in **1**(π)GQDs and red-shifted in **2**(π)GQDs. For both conjugates, the shifts may indicate strong interaction of the Pc with GQDs. The lack of change in the Q band for complex **3**, suggests weak interaction with GQDs. The Q-bands of the covalently formed **4**@rGQDs and **4**@NH_2GQDs conjugates were blue shifted by 6 nm and 4 nm respectively, compared to **4** alone, **Table 3.2**. There is no significant shift in the Q-band of the non-covalently formed **4**(π)rGQDs and **4**(π)NH_2GQDs conjugates, **Fig 3.10D**. The increase in absorption in the B band region for all the conjugates compared to Pcs alone is due to the absorption by GQDs.

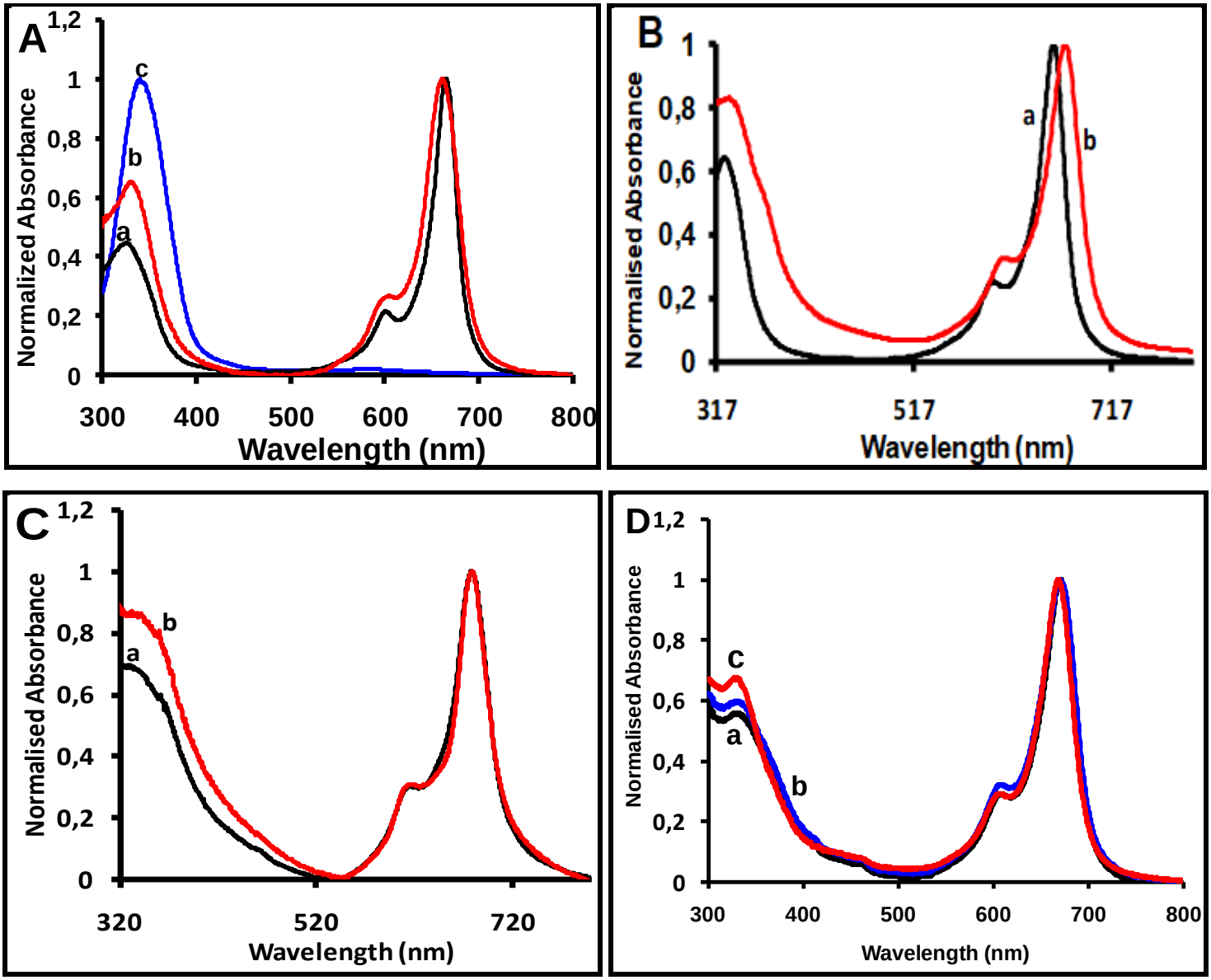

Fig 3.10 UV-Vis spectra of (**A**)**1**(a), **1**(π)GQDs (b) and GQDs (c), (**B**) **2** (a) and **2**(π)GQDs(b); (**C**) spectra of **3** (a), and **3**(π)GQDs (b) and (**D**) **4**(a), **4**(π)rGQDs (b) and **4**(π)NH_2GQDs (c). All in DMSO except for GQDs alone this was run in water.

3.3.2. Raman Spectroscopy

The structure of the formed conjugates was further explored using Raman spectroscopy. **Fig 3.11** shows the Raman spectrum of **4**@GQDs and **4**(π)rGQDs as examples. For the covalently formed conjugates, red shifting on the D bands of the resulting conjugates were observed. The conjugates **4**@rGQDs and **4**@NH_2GQDs

had red shifted D values compared to rGQDs and NH_2GQDs alone, **Table 3.2**.The I_D/I_G ratio increased from 0.21 (rGQDs alone) to 0.58 for **4**@rGQDs, and from 0.18 (NH_2GQDs alone) to 0.44 for **4**@NH_2GQDs. The increase in the I_D/I_G ratio may be symbolic of further disorders and defect formation upon covalent conjugation. For the non-covalently formed conjugates **1**(π)GQDs, **2**(π)GQDs, **3**(π)GQDs, **4**(π)NH_2GQDs and **4**(π)rGQDs there was no peak shift observed, **Fig 3.11** (**4**(π)rGQDs used as an example) . The relative intensities (I_D/I_G ratio) of the GQDs alone and the π-stacked conjugates (for **1** to **3**) remained unchanged at 0.19. There was moderate increase in the I_D/I_G ratio of the **4**(π)rGQDs (0.23) and **4**(π)NH_2GQDs (0.20) was observed. The minimal and absent change indicates intactness of the central graphene sheets and that π-π interaction preserves the structural integrity. The broadening if the D and G bands may be associated with further disruption of the GQDs sp^2 framework during conjugation.

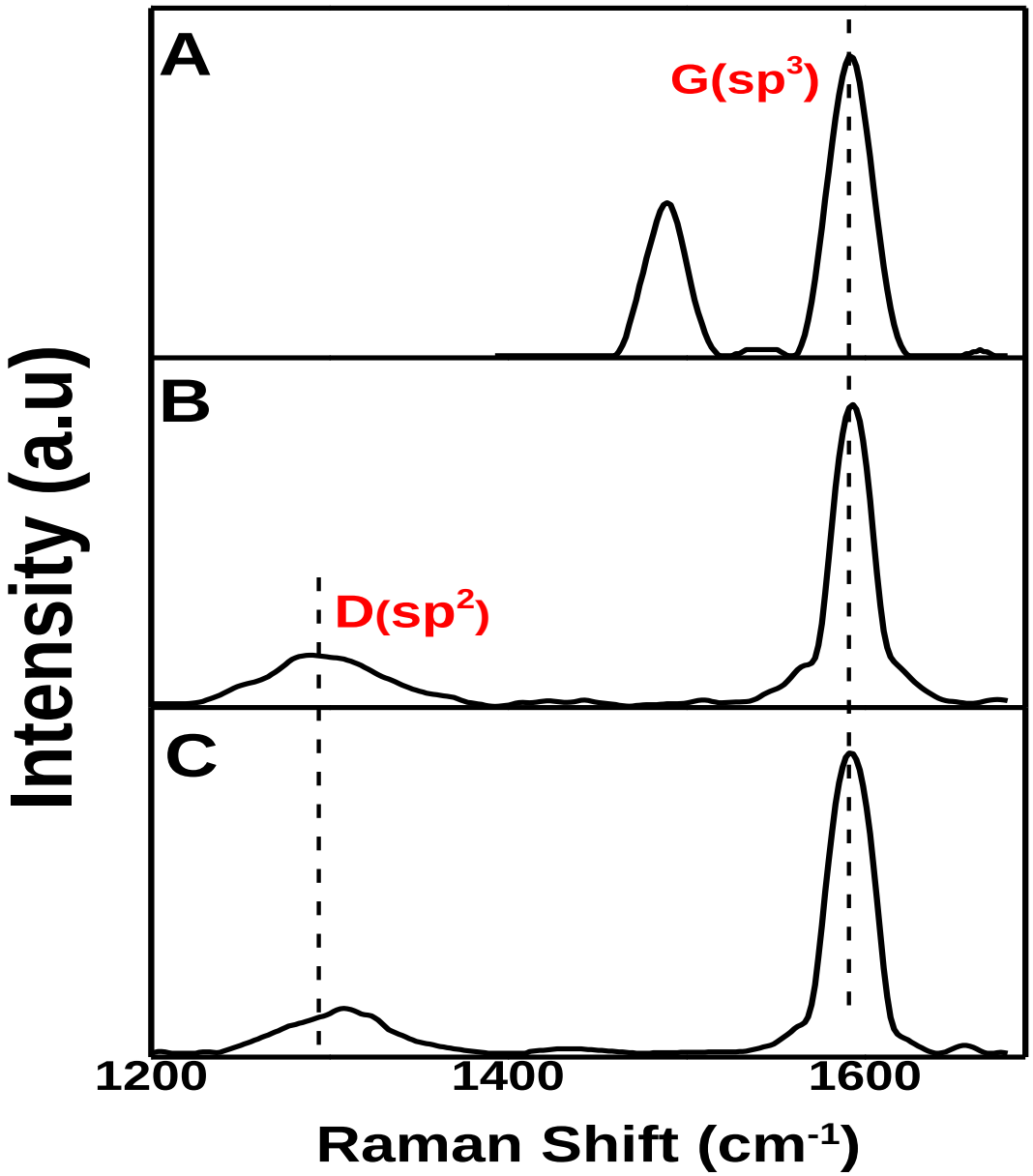

Fig 3.11 Raman Spectra of (**A**) **4**@rGQDs, (**B**) **4**(π)rGQDs and (**C**) rGQDs run in liquid.

3.3.3. FT-IR Spectroscopy

The FTIR spectra for, GQDs, **1**, **1**(π)GQDs and **4**@rGQDs (as examples) are shown in **Fig 3.12**. All conjugates exhibit the same functional groups contained in GQDs (**Fig 3.12**) and the respective individual CoPc derivatives, but with shifts. For **1**(π)GQDs the peaks at 3240 cm^{-1}, 2889 cm^{-1}, 1642 cm^{-1} and 1350 cm^{-1} are associated with O-H, C-H,C=O/C=N and C-O, respectively. For complexes **2** (**3** in brackets) conjugates, the

peaks at 3339 cm^{-1}(3269 cm^{-1}), 1556 cm^{-1} (1570 cm^{-1}), 1230 cm^{-1} (1387 cm^{-1}) and 1035 cm^{-1}(1048 cm^{-1}) associated with O-H, C=O, C-O and C-N, respectively. A similar trend was observed for **4**(π)rGQDs and **4**(π)NH_2GQDs, where the spectra were a combination of both the Pc and individual GQDs. The conjugates **4**@NH_2GQDs and **4**@rGQDs are formed following a nucleophilic substitution reaction which results in the formation of an amide bond between the GQDs and **4**; as such an amide stretch was observed for both conjugates at 3060 cm^{-1} and 3080 cm^{-1} respectively, **Table 3.1**. The presence of such a stretch serves as possible confirmation to successful amide linkage. The spectral shifts observed for the functional peaks in all conjugates were associated with structural changes that might have occurred during conjugation [**88**].

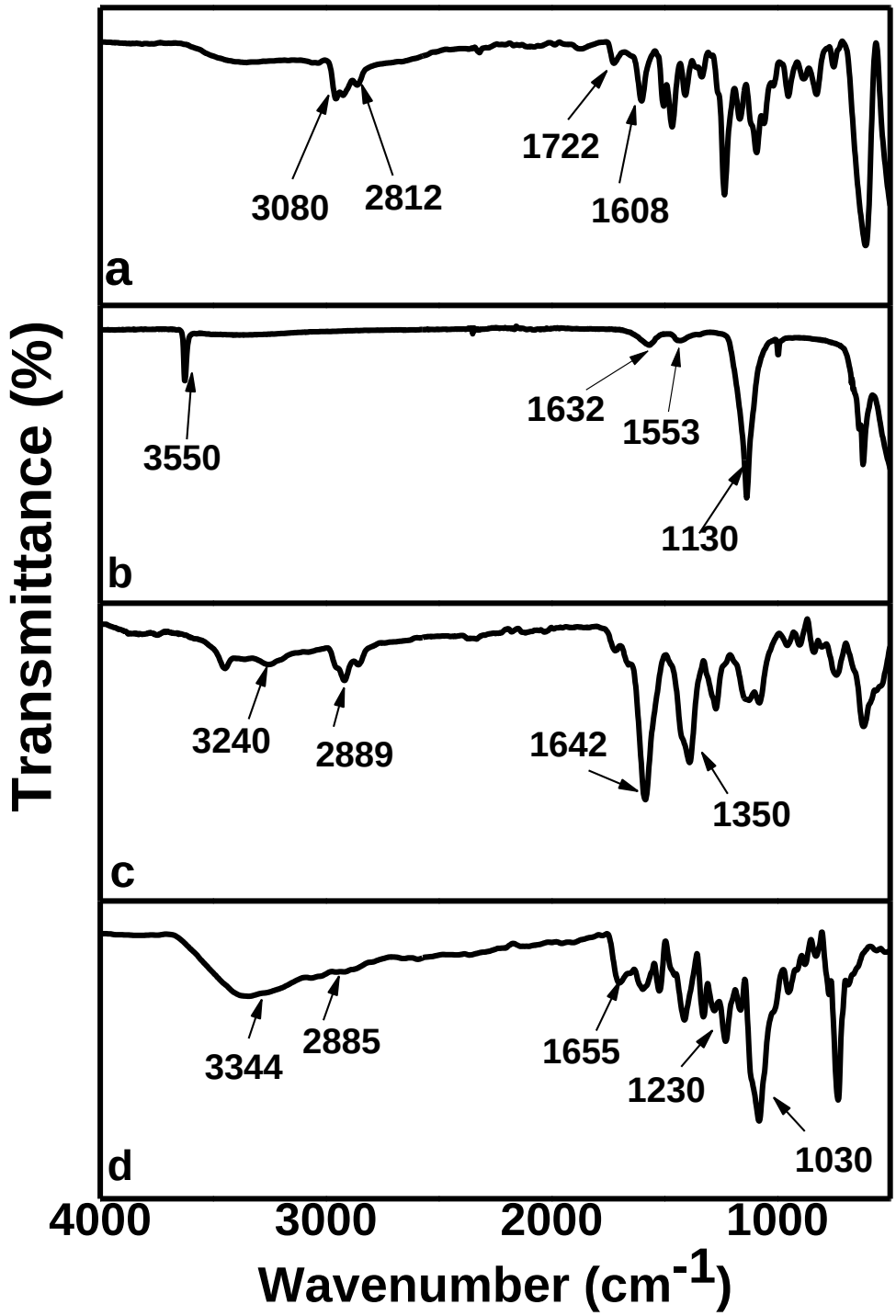

Fig 3.12 IR spectra of (**a**) **4**@rGQDs, (**b**) rGQDs, (**c**) **1**(π)GQDs and (d) **1**.

3.3.4. TEM and DLS Analysis

The morphology and size distribution of GQDs alone and GQDs/MPcs conjugates was analysed using Transmission Electron Microscopy (TEM). **Fig 3.13a** shows fairly dispersed rGQDs as an example. Aggregates seem to have formed upon conjugation as depicted in **Fig 3.13b** (**4**(π)rGQDs shown as representative). Aggregation upon conjugation could be due to π-π interaction from adjacent Pc. Dynamic Light Scattering (DLS) was used to determine the hydrodynamic sizes of the nanoparticles. The pristine GQDs had hydrodynamic sizes of 2.4 nm. A size increase was observed upon conjugation of GQDs onto Pcs. The size increase of GQDs upon conjugation onto MPcs is evident in the DLS data obtained. The resulting conjugates compared to pristine GQDs alone, had hydrodynamic size of 15 nm, 18 nm and 21 nm for **1**(π)GQDs, **2**(π)GQDs and **3**(π)GQDs respectively upon conjugation. The rGQDs and NH_2GQDs (shown in **Fig 3.13c**) had hydrodynamic size 3.2 nm and 2.8 nm, **Table 3.2**. The modification of these GQDs entails introduction of new bulky groups hence the slight size increase from 2.4 nm of pristine GQDs. There was further increase in size upon conjugation of the respective GQDs onto **4**. Hydrodynamic sizes of 10.4 nm and 7.1 nm were obtained for **4**@rGQDs and **4**@NH_2GQDs (shown in **Fig 3.13d** as an example) respectively. Similarly the π-π stacked conjugates had increased in size **4**(π)rGQDs (11.2 nm) and **4**(π)NH_2GQDs (8.2 nm) compared to the respective GQDs alone, **Table 3.2**. The increase in size serves as possible formation of the desired nanoconjugates.

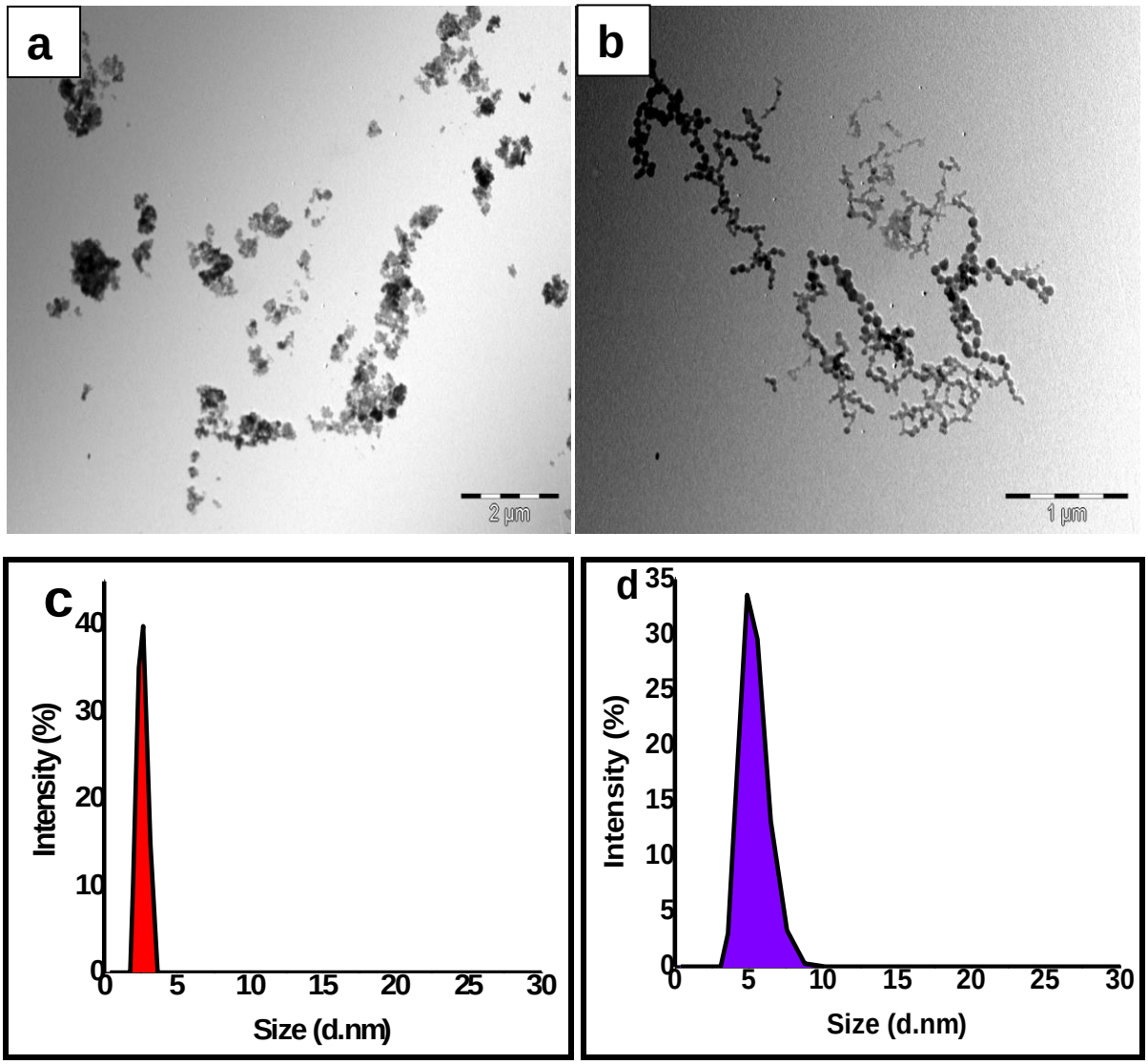

Fig 3.13 TEM image of rGQDs (**a**), **4**(π)rGQDs (**b**), DLS images for NH_2GQDs (**c**) and **4**(π)NH_2GQDs (**d**).

3.3.5. XRD analysis

The XRD data of the conjugates was obtained and is recorded in **Fig 3.14** (**1**(π)GQDs shown as an example). The XRD spectrum of the complex **1** shows sharp peaks indicative of the crystalline nature of the Pc complex [**89**], whilst a broad amorphous peak is observed for GQDs. The XRD spectrum of the resulting conjugate, **1**(π)GQDs shows both the peaks from GQDs and complex **1**. A similar trend was observed for the rest of the conjugates.

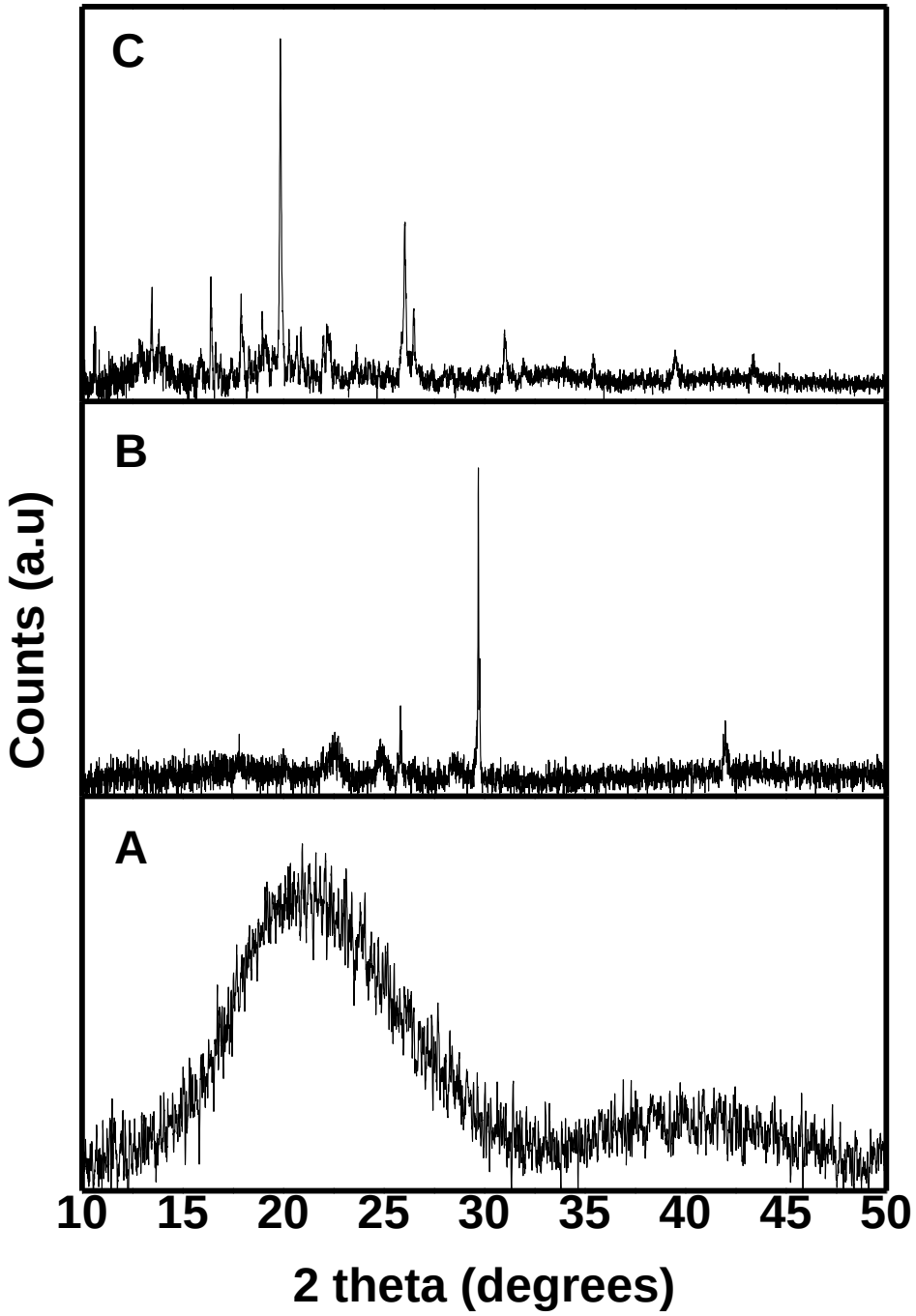

Fig 3.14 XRD spectra images of pristine GQDs (**A**), **1** (**B**) and **1**(π)GQDs (**C**).

3.3.6. XPS analysis

The presence of the amide peaks in the FT-IR spectra of **4**@rGQDs and **4**@NH_2GQDs is not enough confirmation to a successful amide linkage between the respective GQDs and **4**. XPS characterization of the conjugates was for this reason conducted. The N1s high resolution spectra of **4**@rGQDs and **4**@NH_2GQDs conjugates are

shown in **Fig 3.15**. The spectra of both conjugates show the following peaks: C-N, C=N, NH and N-C=O. All peaks are common with those found in the rGQDs and NH_2GQDs alone except for the new NH (400.5 eV; 402.1 eV) peak, **Fig 3.15**. The occurrence of the new peak and disappearance of the NH_2 peak might be as a result to successful amide linkage in **4**@rGQDs and **4**@NH_2GQDs conjugates. Furthermore, the peak occurred at binding energies reported for amide linkages in MPc nanoconjugates [**90**]. The C1s spectra of the formed conjugates (not shown) gave the values shown in **Table 3.3** for O=C-NH since both rGQDs and NH_2GQDs have this peak, the increase in its intensity in the presence of **4** shows an increase in made bonds. The C: O ratio also increased in the presence of complex **4** due to the carbon content from the Pc. The N content also increased in the presence of the complex **4** owing to the N content from the Pc. Both the C/O and N content were found to be higher for the **4**@rGQDs compared to **4**@NH_2GQDs due to the different layering and structural composition of the rGQDs and NH_2GQDs.

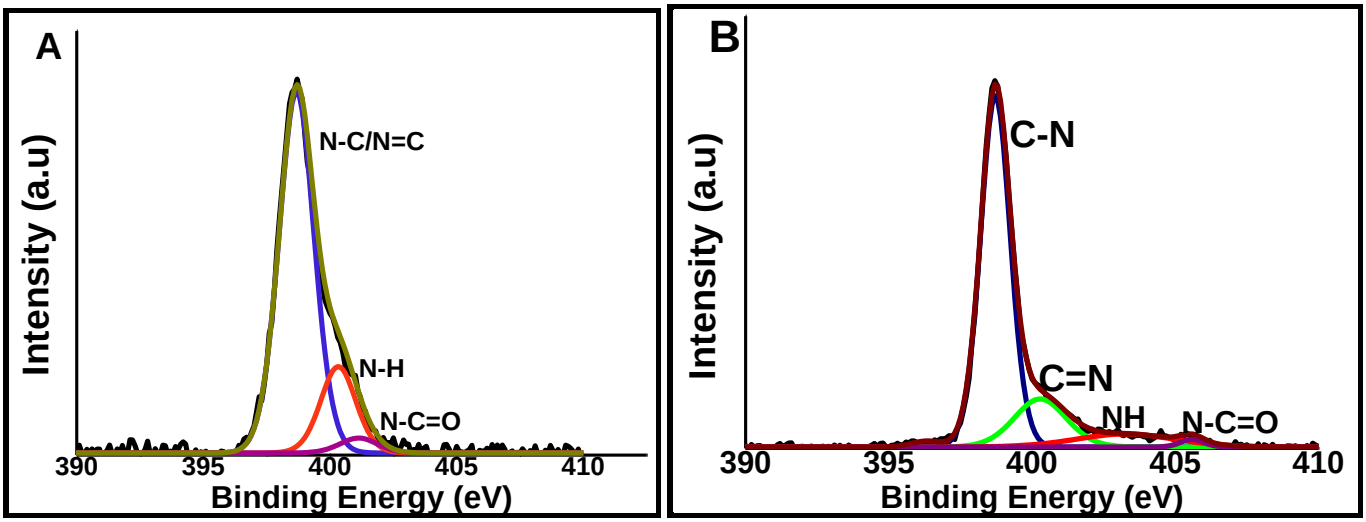

Fig 3.16 N1s high resolution spectra of (**A**) **4**@NH_2GQDs and **4**@rGQDs (**B**) conjugate.

3.4. Conclusions

To conclude this chapter, the information obtained from the spectroscopic and microscopic techniques was used confirm successful synthesis of the desired nanomaterials. TEM and DLS techniques were used to characterize the morphology and size distribution of the synthesized nanomaterials. The FT-IR was useful in confirming the functionalities present in the individual GQDs and CoPc derivatives as well as when combined. XPS provided substantial evidence for the functionalization of GQDs as well as the successful conjugation of the rGQDs and NH_2GQDs onto **4**.

Chapter 4:
Electrode Modification and Characterization

This chapter looks at the electrochemical methods used to characterize the modified GCE. The electrodes were modified using the drop and dry adsorption method. The surface modifiers were used alone, as conjugates (mixed or linked prior modification) and sequentially adsorbed onto an electrode. The drop-dry method is based on the formation of π-π interactions with the bare GCE since it is a carbon based electrode. The extent and manner in which a material is adsorbed onto an electrode plays an important role on its conductivity.

4. Electrode Modification and Characterization

4.1. Cyclic voltammetry

4.1.1. Characterization in Ferricyanide solution

Cyclic voltammetry (CV) was used as a primary characterization technique of the modified electrodes. The conductivity of the probes was interrogated in ferricyanide solution. Ferricyanide solutions have proven to be viable redox mediators owing to their stable Fe(II) and Fe(III) redox states, well-behaved electrochemistry and great sensitivity towards electrode surface kinetics [**91,92**].

Fig 4.1 shows a selection of cyclic voltammograms for 1 mM $[Fe(CN)_6]^{3-/4-}$ in 0.1 M KCl using different electrode modifiers. Different modifiers resulted in varying peak potential separations indicative of different electron transfer abilities. Peak potential separation (ΔE) values close to the standard Nernst value of 58 mV imply good electron transfer ability. The obtained ΔE values of the modified electrodes are listed in **Table 4.1**.

In general, sequentially modified electrodes show lower ΔE values, hence better electron transfer ability. For sequentially modified electrodes, better electron transfer was obtained when Pcs are placed on top, with the exception of GCE/GQDs-**1** (seq). When comparing the carboxyphenoxy substituted complexes **1** and **2**, better electron transfer ability is obtained for the mono substituted complex **1** when alone (GCE/**1**) and in π-π conjugation with GQDs (GCE/**1**(π)GQDs). When comparing the tetra substituted complexes **2** and **3** containing different substituents; complex **3** containing aminophenoxy, shows better electron transfer in all cases, showing the importance of this substituent. The ΔE of bare GCE (BGCE), GCE/GQDs, GCE/GQDs-**2** (seq), and GCE/GQDs-**3** (seq) are closer to the Nernstian value of 58 mV for a one electron process; this serves an indication of their good electron transfer kinetics for the

$[Fe(CN)_6]^{3-/4-}$. The modified with Pc complexes **1**, **2** and **3** alone showed better electron transfer kinetics compared to its respective conjugates {**1**(π)GQDs, **2**(π)GQDs and **3**(π)GQDs}. The difference may be because of aggregation of Pc during π-π interactions, which might have resulted in passivation of the electrode surface and hence higher Nernstian values for the conjugates compared to Pc complexes alone. Even though GCE/GQDs showed good electron transfer in ferricyanide solution, it will be shown below that this electrode gave low detection currents for hydrazine detection, hence, the presence of phthalocyanines is important. The non-covalent conjugates: GCE/**4**(π)rGQDs and GCE/**4**(π)NH_2GQDs had a lower ΔE when compared to the corresponding covalent conjugates, GCE/**4**@rGQDs and GCE/**4**@NH_2GQDs, showing the advantage of preserving the π structure of GQDs. It is important to note that the good electron transfer in ferricyanide is independent of the catalytic activity of the probes towards hydrazine detection.

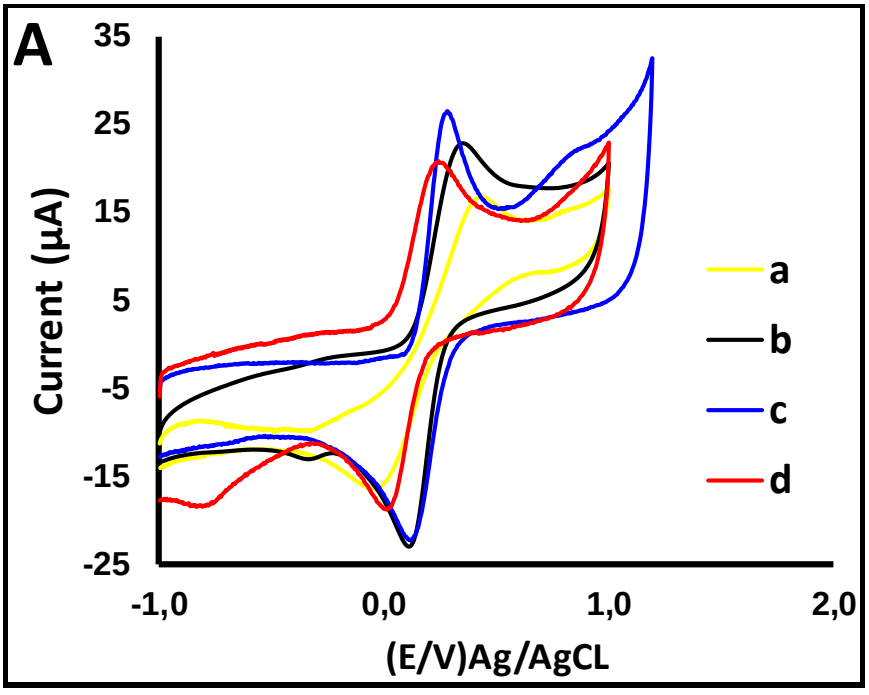

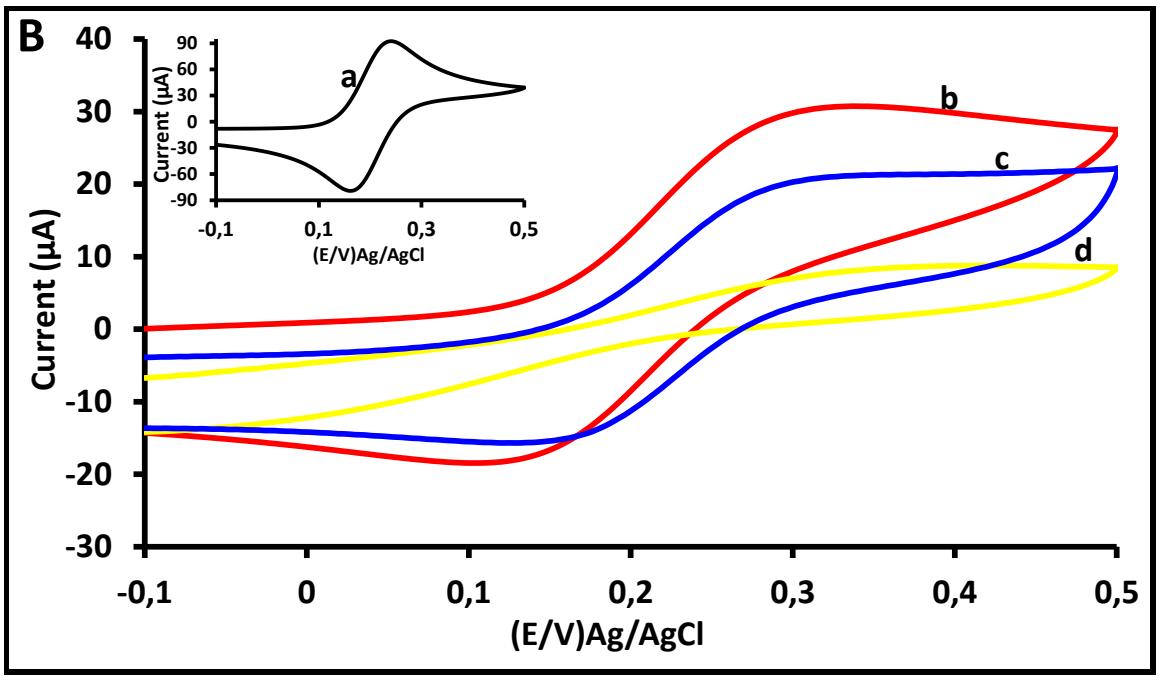

Fig 4.1 Cyclic voltammograms of the modified electrodes in 1 mM $[Fe(CN)_6]^{3-/4-}$ in 0.1 M KCl: (**A**) GCE/**2**(π)GQDs(**a**), GCE/**3**(π)GQDs (**b**), GCE/**3** (c) and GCE/**2** (**d**), and (**B**) BGCE (**a**), GCE/**4**@NH_2GQDs (b), GCE/**4**@rGQDs (**c**) and GCE/rGQDs (**d**).

Table 4.1 ΔE values for the modified electrodes in ferricyanide solution

Probes	**ΔE $Fe(CN)_6^{3-/4-}$ (0.1 M KCl) (mV)**
GCE	60
GCE/GQDs	73
GCE/rGQDs	171
GCE/NH_2GQDs	100
GCE/**1**	127
GCE/**2**	165
GCE/**3**	108
GCE/**1**(π)GQDs	200
GCE/**2**(π)GQDs	385
GCE/**3**(π)GQDs	179
GCE/**1**-GQDs (seq)	91
GCE/GQDs-**1** (seq)	165
GCE/**2**-GQDs (seq)	217
GCE/GQDs-**2**(seq)	66
GCE/**3**-GQDs (seq)	107
GCE/GQDs-**3**(seq)	59
GCE/**4**	132
GCE/**4**(π)rGQDs	185
GCE/**4**(π)NH_2GQDs	192
GCE/**4**@rGQDs	232
GCE/**4**@NH_2GQDs	207

*Reminder: GCE/Pc-GQDs = Pc first and GCE/GQDs/Pc = GQDs first for sequential

Seq = sequentially adsorbed electrodes

4.1.2. Characterization in 0.1 M NaOH buffer

The modified electrodes were tested in a 0.1 M NaOH solution in which hydrazine (analyte) was to be dissolved in. The buffer is used as a blank and it helps distinguish the activity of the electrocatalysts in the absence and presence of the analyte. The obtained scans provide the ability to monitor any interference and to ensure that any peaks that arise in the presence of the analyte belong to the analyte. The CV scans obtained in the buffer are shown in **Fig 4.2**. The electrodes modified with the complexes **1**, **2**, **3** and **4** alone showed oxidation peaks at potentials 0.32 V, 0.12 V, 0.15 V and 0.25 V. These peaks may be assigned to Co^{3+}/Co^{2+} of the CoPc **[93]**. The conjugate GCE/**2**(π)GQDs showed a peak around 0.85 V which can be assigned to ring based oxidation. No peaks were observed for the rest of the electrodes.

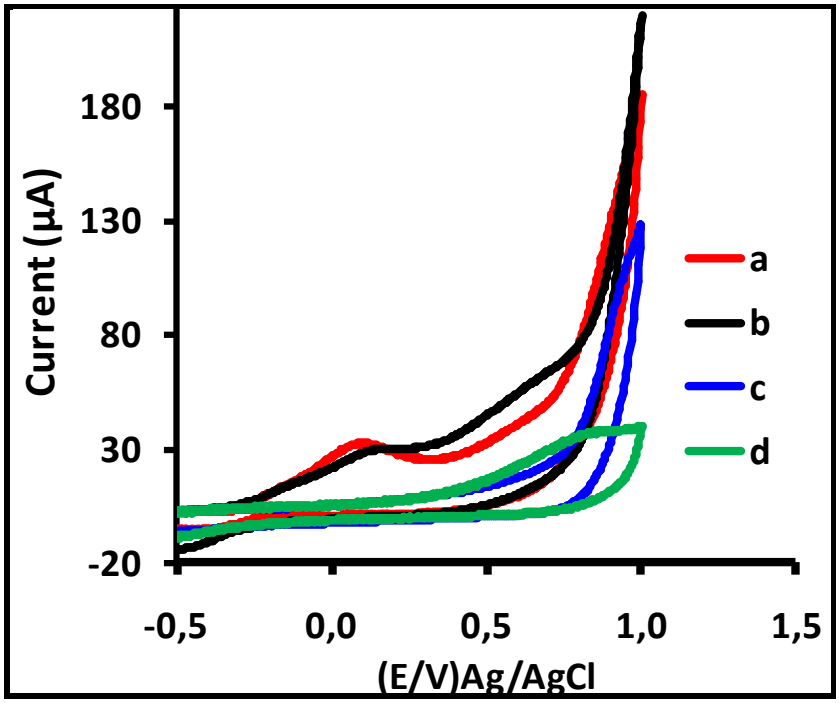

Fig 4.2 Cyclic voltammograms of GCE/**3** (**a**), GCE/**2** (**b**), GCE/**3**(π)GQDs (**c**) and GCE/**2**(π)GQDs (**d**) in pH 7 buffer. Scan rate 100 mV/s.

4.2. Scanning electrochemical microscopy (SECM)

SECM is a technique in which current flowing through an ultramicroelectrode (UME) tip near a conducting, non-conducting or insulating substrate immersed in solution is used to amperometrically or voltammetrically characterize processes and structural features at the substrate, as the tip is moved close to the surface. The electrode tip can be moved in three dimensions; to the surface (z- direction) to probe the diffusion layer, across the surface at constant z (the x and y directions). The technique is an electrochemical process, and so the tip and the substrate are part of an electrochemical cell with an auxiliary and reference electrode **[94, 95]**. .

In this work SECM was used to study the conductivity of the substrates through area scans and approach curves. For an insulating material a decrease in the current is observed as the electrode tip approaches the surface, this is also known as the negative feedback (**Fig 4.3a**). In the case of a conducting surface however, an increase in current as the probe approaches the surface is observed and this is referred to as the positive feedback mode (**Fig 4.3b**) **[96, 97]**.

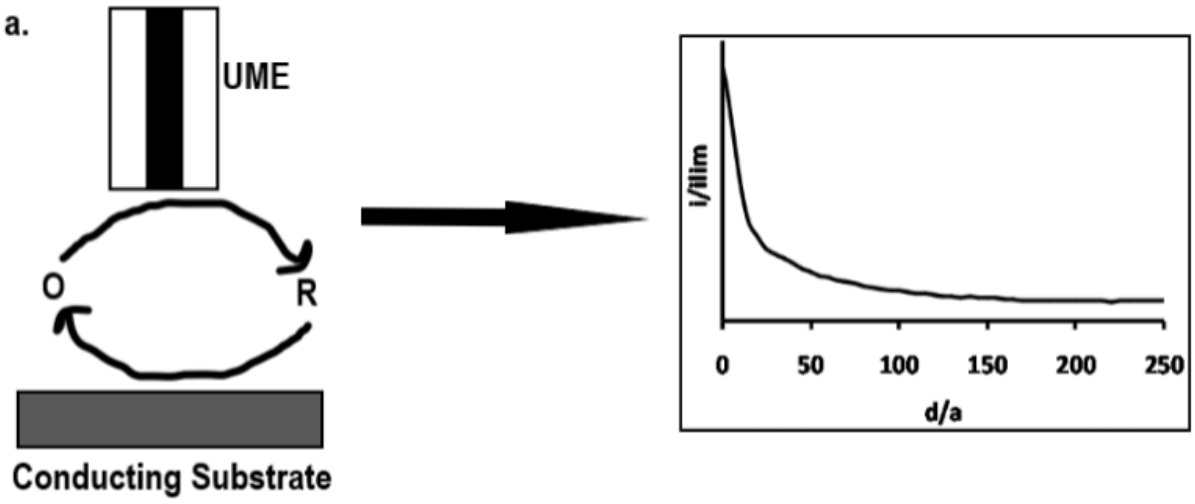

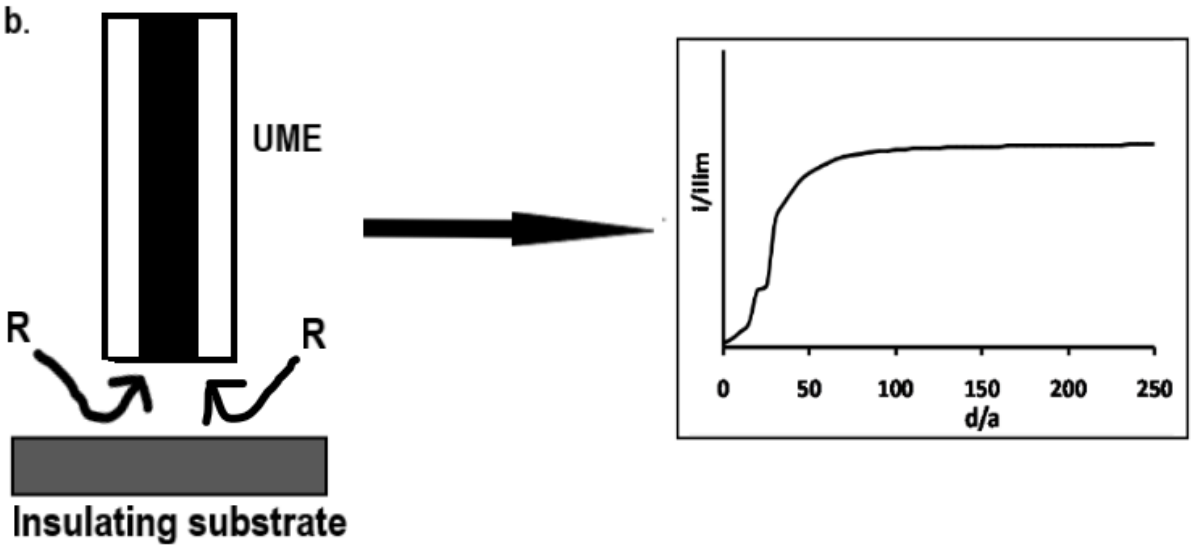

Fig 4.3 SECM approach curves on a conducting (**a**) and insulating (**b**) substrates.

The approach curves obtained for the modified surfaces is shown in **Fig 4.4** (showing **1**(π)GQDs as an example). The approach curves show changes in tip current as the UME tip approaches the substrate in a feedback mode experiment in the presence of Fe^{3+}/Fe^{2+} redox mediator. Teflon is an insulator, as a result current decreased as the tip approached the surface, **Fig 4.4**. The bare glassy carbon plate (BGCP) is more conductive than the GCP/**1**(π)GQDs. Approach curves showing low conductivity of electrodes modified with Pc by grafting followed by click chemistry have been reported **[98]**, with the electrode still being catalytic for the analyte.

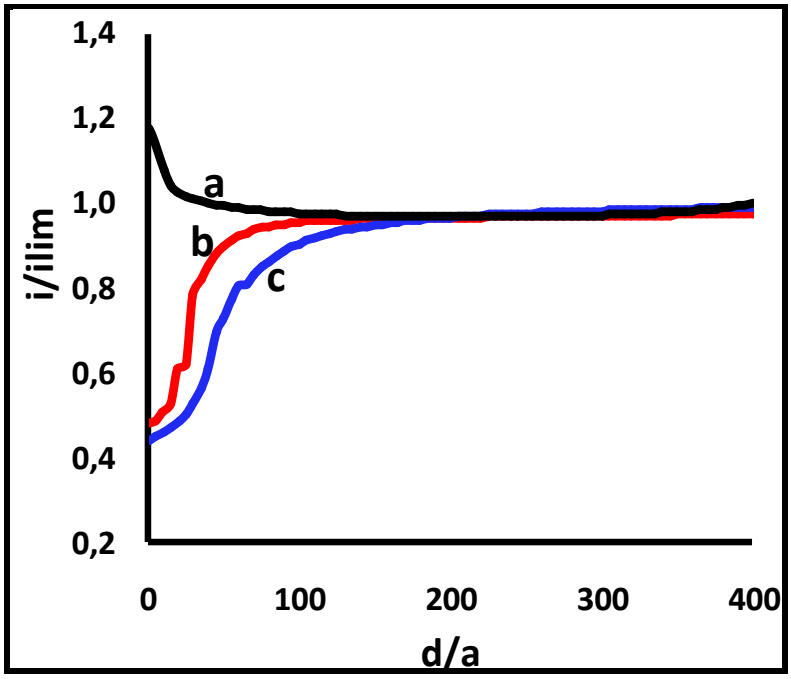

Fig 4.4 Approach curves of (**a**) Bare GCP, (**b**) GCP/**1**(π)GQDs and (**c**) non-conducting Teflon. All in 1 mM $[Fe(CN)_6]^{3-/4-}$ in 0.1 M KCl. Where d/a=ratio of tip substrate to UME tip radius.

Area scans are obtained by scanning through the surface while maintaining the height (z-axis) constant and measuring the current with respect to position. Area scans of the bare electrode and the modified GCE/**1**(π)GQDs are shown in **Fig 4.5**. The bare GCP shows a uniform conducting surface compared to the **1**(π)GQDs modified surface. The bare GCP had the least recorded currents compared to the catalyst modified plates. This may be indicative of the catalytic nature of the various modifiers employed.

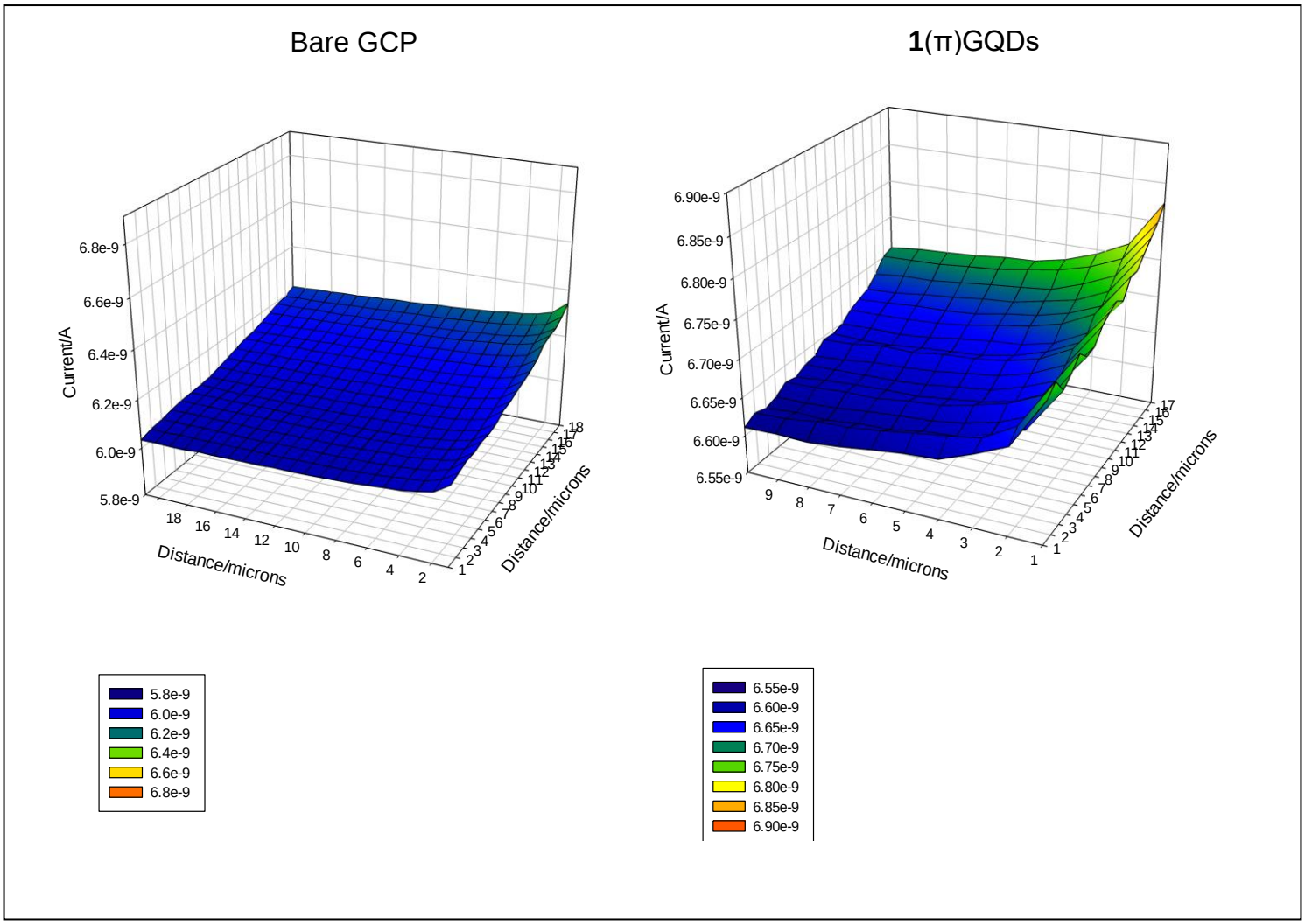

Fig 4.5 SECM area scan obtained for a bare glassy carbon plate (BGCP) and GCP/**1**(π)GQDs in using 2.5 µm UME in 5 mM $[FeCN_6]^{3-/4-}$ in 0.1 M KCl.

4.3. Conclusions

The CV diagrams obtained in $[FeCN_6]^{3-/4-}$ emphasizes on the difference in electron transfer abilities of the probes. Poor electron transfer properties were observed for CoPc/GQDs probes as evidenced by the large ΔE values. The varying ΔE values between the BGCE and modified electrodes confirm that the modification was successful. Furthermore, from the SECM; the difference in the conductivity obtained for the BGCP and modified GCP confirm change in surface of the substrate. The area scans obtained displayed higher currents for modified GCP than the bare GCP indicating surface difference. The CV scans obtained from the buffer solution provided

information about the species present on the surface, further confirming successful modification of the GCE.

Chapter 5:
Electrocatalysis - Electrocatalytic Detection of Hydrazine

The synthesized nanoprobes were tested towards the electrooxidation of hydrazine. The main focus of this work is on the electrocatalytic activity of cobalt based phthalocyanines as surface modifiers alone and in the presence of GQDs. The influence of the GQDs on the electroactivity of CoPc derivatives is reported. Cyclic voltammetry and chronoamperometry were applied on all the electrodes. Cyclic voltammetry was used for the determination of Tafel slopes and oxidation potentials. Chronoamperometry was found useful for the determination of the sensitivity and limit of detection (LOD) of the catalysts.

5. Electrocatalytic Detection of Hydrazine

5.1. Comparative cyclic voltammetry

5.1.1. Non-covalent (π-π stacked) and covalent

5.1.1.1. Oxidation potentials

Fig 5.1 compares cyclic voltammograms obtained from the various modified electrodes in 1 mM Hydrazine in 0.1 M NaOH. Electrocatalysis is evidenced by lowering of potentials and increasing currents. The GCE/**1** had better oxidation potential towards hydrazine at 0.52 V compared to 0.76 V, 0.90 V and 0.93 V for complexes **4**, **3** and **2** respectively, **Table 5.1**. Double oxidation peaks were observed in some cases. The electro-oxidation on both scans has been attributed to the regeneration or reformation of the active catalyst that oxidises hydrazine [**99**]. The CV for pristine GQDs (**Fig 5.1A**) showed no defined hydrazine oxidation peak, but a broad feature. Having shown the incompetency of the GCE/GQDs catalyst no further electrochemical reactions involving it were conducted. The CV scans obtained for GCE/NH_2GQDs and GCE/rGQDs (the latter shown as an example, **Fig 5.1B**) show a defined oxidation peak for hydrazine at potentials 0.95 V and 0.88 V respectively. The electrocatalytic activity of the CoPc derivatives in the presence of GQDs is very much dependant on the interaction occurring between the two catalysts, as well as the manner in which the resulting conjugate will interact with the analyte. Lowered potentials are observed for GCE/**3**(π)GQDs (0.85 V) compared to complex **3** (0.90 V) alone. The electrodes GCE/**1** (0.52 V) and GCE/**2** (0.93 V) showed lower potential values alone compared GCE/**1**(π)GQDs (0.62 V) and GCE/**2**(π)GQDs (1.09 V).The functionalized rGQDs and NH_2GQDs were π-π stacked with complex **4** and were applied for surface modification forming the electrodes; GCE/**4**(π)rGQDs and

GCE/**4**(π)NH_2GQDs. The rGQDs and NH_2GQDs were also covalently linked onto **4** to form the electrodes GCE/**4**@rGQDs and GCE/**4**@NH_2GQDs. The electrodes GCE/**4**(π)rGQDs and GCE/**4**(π)NH_2GQDs showed less favourable potentials 1.07 V and 0.98 V respectively for hydrazine oxidation compared to the corresponding covalent conjugates GCE/**4**@rGQDs (0.87 V) and GCE/**4**@NH_2GQDs (0.92 V) showing the importance of covalent linking.

5.1.1.2. Oxidation Current

In terms of catalytic currents for hydrazine oxidation, the largest currents are observed for GCE/**4**(π)rGQDs and the least observed for GCE/**1**. A significant increase in catalytic current for complexes **1** and **2** upon conjugation with GQDs; GCE/**1**(π)GQDs and GCE/**2**(π)GQDs respectively was observed, **Table 5.1**. A noticeable increase in current is observed for all catalysts compared to the BGCE following the trend **1**<**4**<**3**<**2**. Complex **1** has a single carboxyphenoxy substituent while complex **2** has four. This implies that complex **2** has more active sites for interaction with the analyte compared to **1**, hence the better catalytic activity. The better catalytic activity of **2** compared to the aminophenoxy containing complex **3** is not fully understood.

Higher catalytic currents were obtained for GCE/rGQDs compared to GCE/NH_2GQDs, **Table 5.1** alone or upon conjugation. This demonstrates the significance of band gap manipulation by reduction of the GQDs, which in turn results in enhanced electron transfer and electrocatalytic activity. Higher catalytic currents were as a result obtained for all rGQDs containing electrodes compared to NH_2GQDs derivatized. Higher catalytic currents were obtained for the GCE/**4**(π)rGQDs and GCE/**4**(π)NH_2GQDs compared to GCE/**4**@rGQDs and GCE/**4**@NH_2GQDs. The GCE/**4** showed superior catalytic activity compared to the covalently linked modifiers (GCE/**4**@rGQDs and GCE/**4**@NH_2GQDs).

The characteristic contributor to the electrocatalytic activity of **4** is its push-pull effect arising from its substitution and symmetry, which has been reported to enhance delocalization and thus electron transfer properties [**100**]. As a result the Pc complex **4** showed superior catalytic activity alone compared to **1**, **2** and **3** alone and when conjugated to GQDs, **Table 5.1**. During π-π interactions, the push-pull property of **4** is preserved, the opposite is observed for the covalently formed conjugates. Upon the covalent linkage of rGQDs and NH_2GQDs onto **4**, the electron with drawing –COOH group is replaced with the electron rich rGQDs and NH_2GQDs entities thereby disturbing the push-pull effect and electron transfer of **4**.

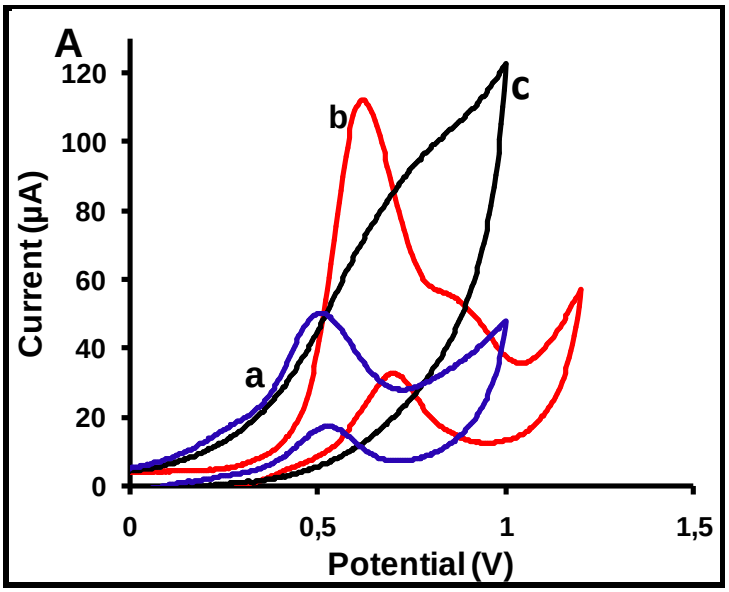

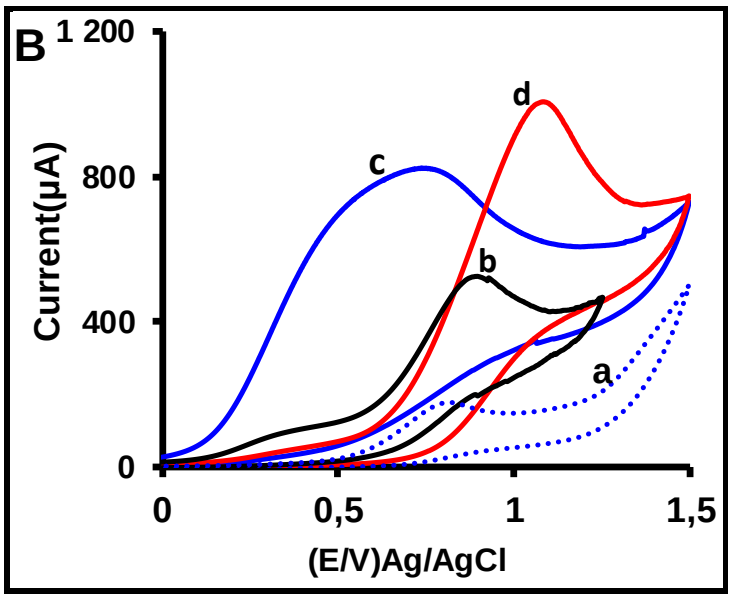

Fig 5.1 (**A**) shows CV scans obtained for (a) GCE/**1**, (b) GCE/**1**(π)GQDs and (c) GCE/GQDs, (**B**) shows CV scans obtained for GCE/rGQDs (a), GCE/**4**@GQDs (b), GCE/**4** (c) and (d) GCE/**4**(π)rGQDs 1 mM Hydrazine in 0.1 M NaOH.

Table 5.1 Oxidation potential and catalytic currents of all the electrodes in this thesis

Modified electrodes	**Ep [N_2H_4]**	**Background corrected Current (μA)**	**Tafel Slope (mV/decade)**
GCE/**1**	0.52	39	608
GCE/**1**(π)GQDs	0.62	100	218
GCE/**2**	0.93	402	136
GCE/**2**(π)GQDs	1.09	811	148
GCE/**3**	0.90	373	372
GCE/**3**(π)GQDs	0.85	323	362
GCE/**1**-GQDs (seq)	0.80	55	35
GCE/GQDs-**1**(seq)	0.75	76	342
GCE/**2**-GQDs (seq)	1.04	150	72
GCE/GQDs-**2**(seq)	0.89	797	268
GCE/**3**-GQDs(seq)	0.98	276	150
GCE/GQDs-**3** (seq)	0.87	747	120
GCE/rGQDs	0.88	187	136
GCE/NH_2GQDs	0.95	122	96
GCE/**4**	0.76	807	180
GCE/**4**@rGQDs	0.87	522	78
GCE/**4**(π)rGQDs	1.07	1090	210
GCE/**4**@NH_2GQDs	0.92	405	220
GCE/**4**(π)NH_2GQDs	0.98	424	92

5.1.2. Sequentially Modified Electrodes

The sequential adsorption of the modifiers onto electrodes involves layering of the catalysts on top each other in drops. The electrodes were sequentially modified such that a layer of the CoPc is placed beneath the GQDs (CoPc-GQDs) and vice versa (GQDs-CoPc). The resulting modifiers are GCE/**1**-GQDs (seq), GCE/GQDs-**1** (seq), GCE/**2**-GQDs (seq), GCE/GQDs-**2** (seq), GCE/**3**-GQDs (seq) and GCE/GQDs-**3** (seq). The CV scans obtained for the electrooxidation of hydrazine by these modifiers is shown in **Fig 5.2** (sequential electrodes for complexes **2** and **3** shown as examples). For sequentially modified electrodes, less positive potential is observed when the Pc is placed on top GQDs in all cases (involving complexes **1**, **2** and **3**). The modified GCE/GQDs-**3** (seq) electrode showed better catalytic currents compared to GCE/**3**(π)GQDs. The catalytic current obtained for the GCE/GQDs-**2** (797 μA) is comparable to GCE/**2**(π)GQDs (811 μA). Where complex **1** is concerned however, the GCE/**1**(π)GQDs (100 μA) showed better activity than the sequentially modified GCE/GQDs-**2** (76 μA) electrode. The Pc being on top (GQDS-CoPc) implies direct interaction with the analyte of interest, compared to when it is shielded by GQDs when placed first (CoPc-GQDs). The (CoPc-GQDs) electrodes show deformation of the CV scan compared to the well-defined scans obtained for GQDs-CoPc electrodes. There is no clear trend in the electrocatalytic activity of the sequentially adsorbed electrodes compared to the electrodes of π-π stacked conjugates.

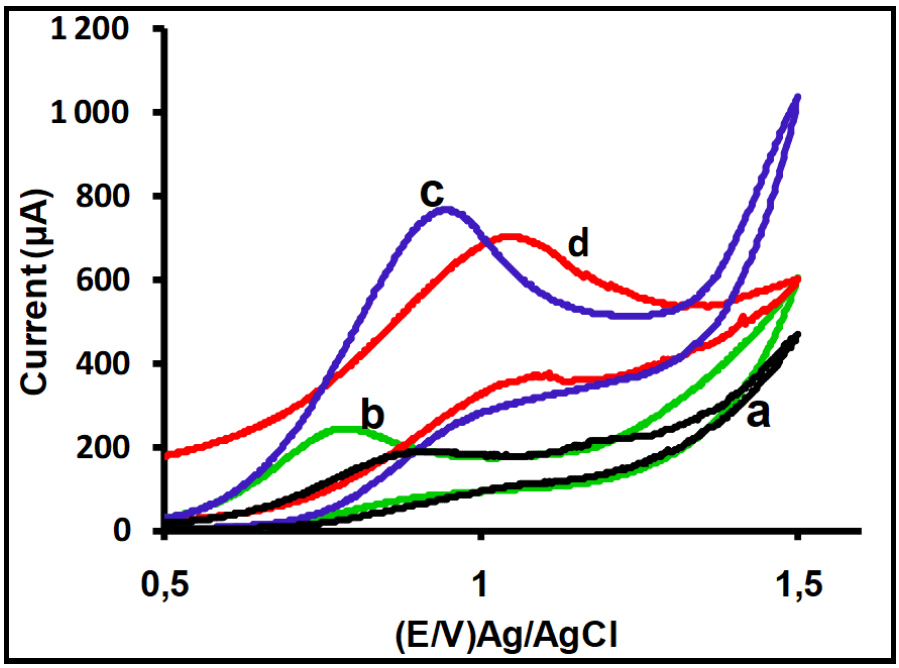

Fig 5.2 CV scans obtained for sequentially adsorbed modifiers (**a**) GCE/**2**-GQDs (seq), GCE/**3**-GQDs (seq) (**b**), GCE/GQDs-**3** (seq) (**c**) and GCE/GQDs-**2** (seq) (**d**).

5.2. Electrode Stability

To test the stability and reusability; the electrodes were subject to 20 consecutive scans at 100 mV/s in 1 mM hydrazine. **Fig 5.3** shows the stability cycles obtained for GCE/**2**(π)GQDs and GCE/**3**(π)GQDs as examples. The stability of the electrodes was characterized by decrease in the catalytic currents over time. The currents of the electrodes stabilized after 20 scans. The electrodes were stored for a week under inert atmosphere and still displayed fair stability. The GCE/**2**(π)GQDs showed better stability in that its oxidation peaks stabilized at higher currents compared to the rest of the modified electrodes. The electrodes containing **4** showed better catalytic stability than those of **1**, **2** and **3**. The non-covalent GCE/**4**(π)rGQDs and GCE/**4**(π)NH_2GQDs showed better stability compared to its corresponding covalent GCE/**4**@rGQDs and GCE/**4**@NH_2GQDs respectively. For the sequentially adsorbed electrodes, superior electrode stability was observed for electrodes where the Pc was on top of the GQDs (GCE/GQDs-CoPc). The percentage current loss obtained for all probes was less than

50% and as a result probes can be used several times as the currents stabilize over time.

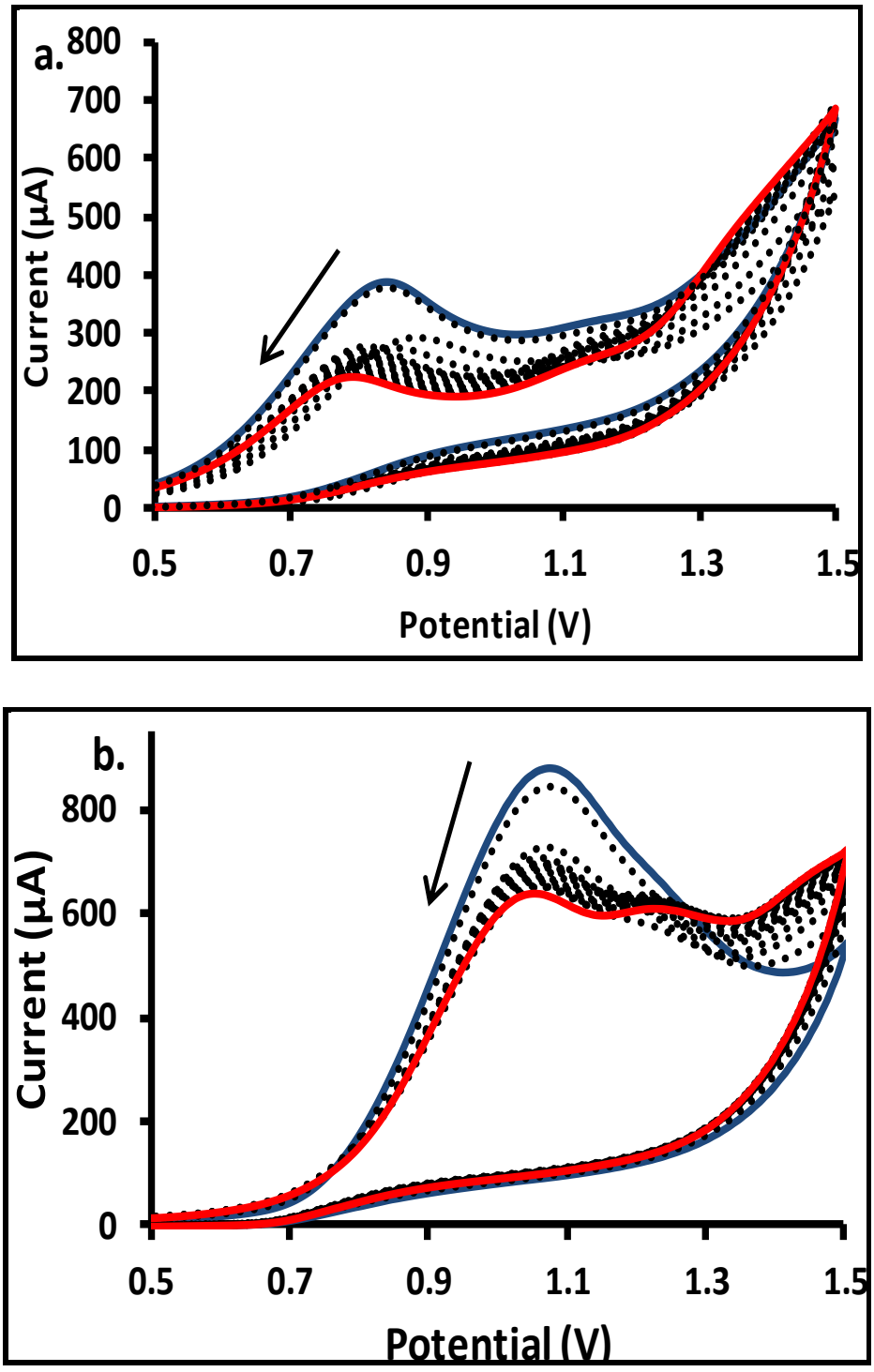

Fig 5.3 Stability scans for (**a**) GCE/**3**(π)GQDs and (**b**) GCE/**2**(π)GQDs at 100 mV/s in 1 mM hydrazine in 0.1 M NaOH. Blue=1st scan and red=20th scan.

5.3. Kinetics using CV

Fig 5.4 shows that peak potential increased with scan rate (showing GCE/**3**(π)GQDs as an example) thus indicating the chemical irreversibility of the hydrazine electrooxidation process. The linear relationship between the current and the square root of the sweep rate is symbolic of a diffusion-controlled oxidation reaction. The relationship between peak potential and scan rate for an irreversible and diffusion controlled is given by equation (**5.1**) [**101**]

$$Ep = \frac{b}{2}\log v + K \qquad (\mathbf{5.1})$$

where *v* is the scan rate and b is the Tafel slope. Linear plots for log *v* vs. Ep were obtained and employed for the calculation of Tafel slopes, **Fig 5.4b**. Tafel slopes higher than the normal 60–120 mV/decade (**Table 5.1**) were obtained, which may suggest adsorption of either the products and/or intermediates on the modified electrode surface **[102, 103]**. A Tafel slope of 35 mV/decade is observed for GCE/**1**-GQDs, such low Tafel slopes have been explained in terms of diffusion overvoltage, with the Tafel step no longer rate-determining [**104**]. The linearity of the plot of current vs. square root (time) implies that the oxidation reaction is diffusion controlled, **Fig 5.4c**.

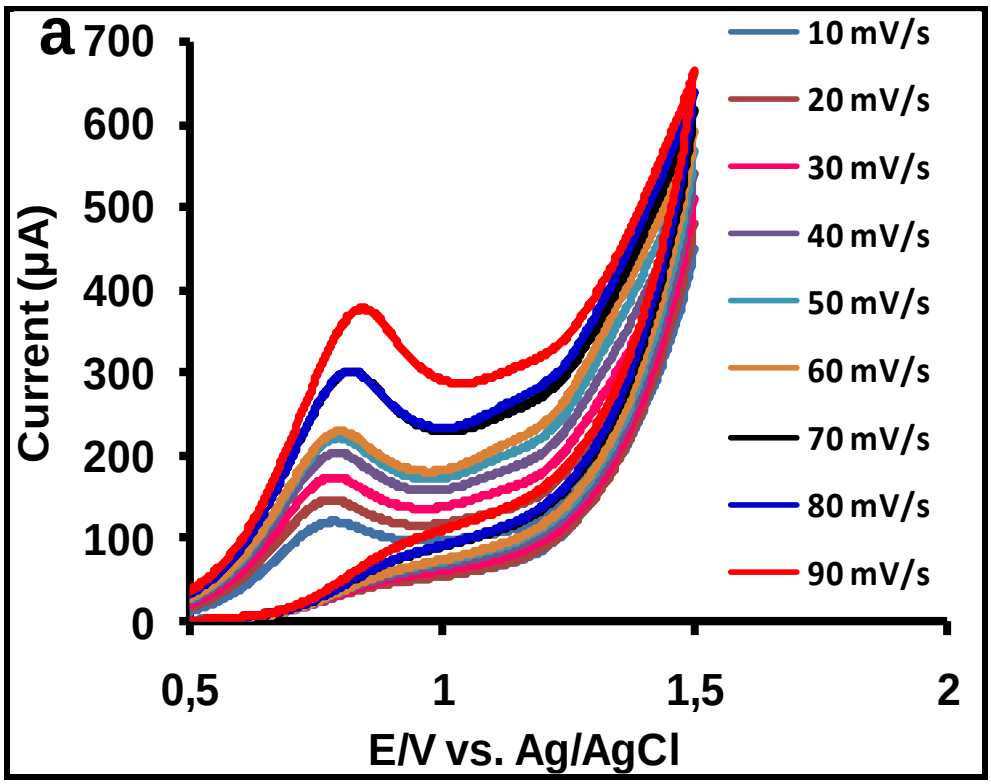
a
700
600
500
400
300
200
100
0
Current (µA)
0,5
1
1,5
2
E/V vs. Ag/AgCl
10 mV/s
20 mV/s
30 mV/s
40 mV/s
50 mV/s
60 mV/s
70 mV/s
80 mV/s
90 mV/s

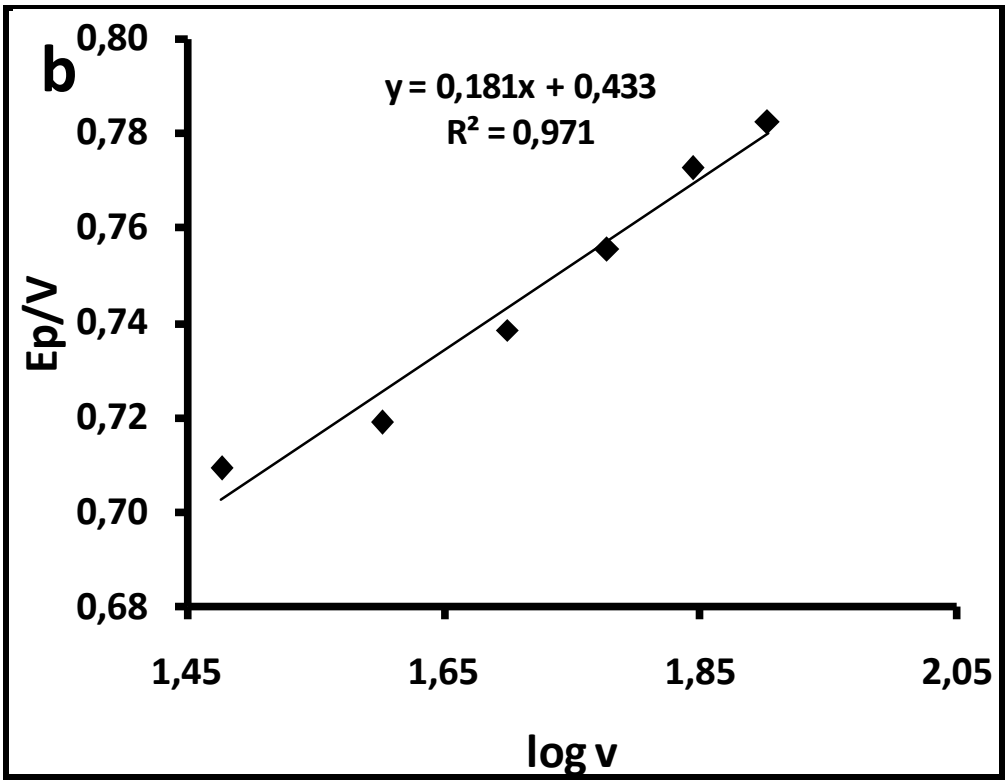
b
0,80
0,78
0,76
0,74
0,72
0,70
0,68
Ep/V
y = 0,181x + 0,433
R² = 0,971
1,45
1,65
1,85
2,05
log v

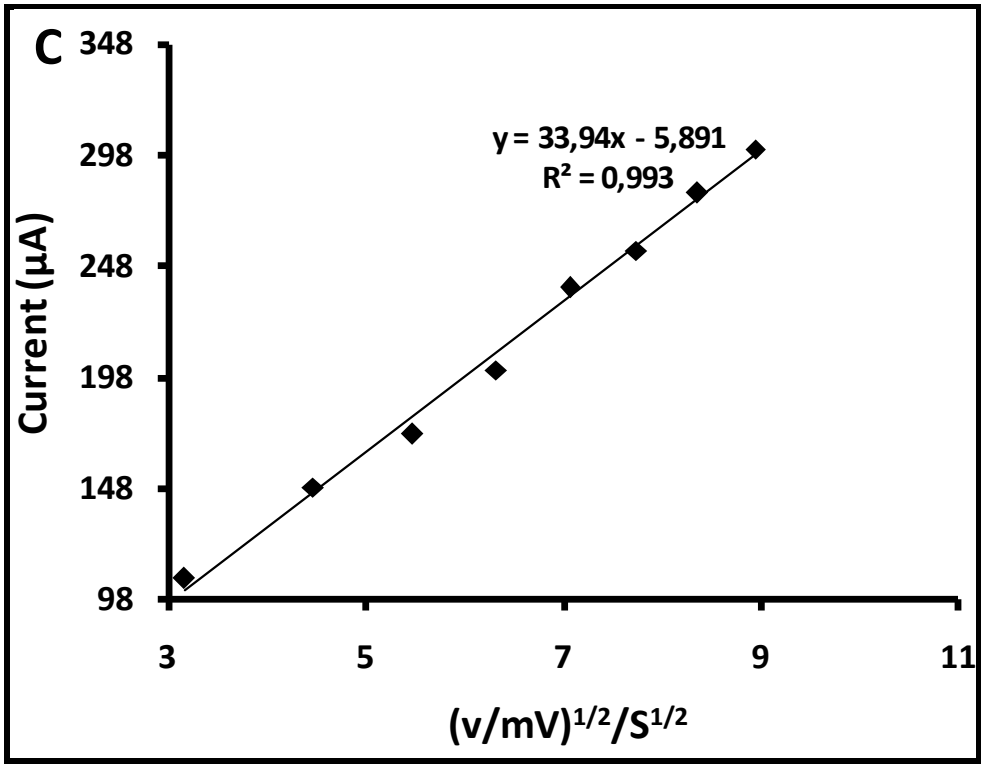

Fig 5.4 (**a**) Various scan rate of GCE/**3**(π)GQDs, (**b**) potential (Ep) vs. log v and (**c**) plot of current vs. square root scan rate ($v^{1/2}$) in 1 mM hydrazine in 0.1 M NaOH. Scan rate=100 mV/s

5.4. Chronoamperometry

5.4.1. Determination of rate constants

Chronoamperometry is a transient technique in which the applied potential leads to the immediate oxidation or reduction of the analyte on the electrode surface, to give a current signal that rapidly decays in the mass transfer limited region. The polarizing potential is chosen based on the oxidation/reduction peak potentials of the analyte to allow for its instantaneous oxidation/reduction **[105,106]**. The chronoamperometric data obtained was employed to determine the catalytic rate constant for the oxidation of hydrazine. Catalytic rate constants are a measure of the rate at which the oxidation process occurs at the electrode|analyte interface. **Fig 5.5a** shows chronoamperometric evolutions at various concentrations of hydrazine using

GCE/**2**(π)GQDs as an example. Plots of I_{cat}/I_{buff} vs. square root of time (**Fig. 5.5b** and **Eq 5.2**) within rapid decay region (< 2 s) were linear with varying slopes [**107**]

$$\frac{Icat}{Ibuf} = \gamma^{\frac{1}{2}}\pi^{\frac{1}{2}} = \pi^{\frac{1}{2}}(kCt)^{\frac{1}{2}} \qquad \textbf{(5.2)}$$

where I_{cat} and I_{buff} represent the currents in the presence and absence of hydrazine respectively, *k* the catalytic rate constant, *C* the bulk concentration of hydrazine and *t* the time elapsed in seconds. Plotting the square of the slopes (from **Fig.5.5b**) against the respective concentrations gave linear plots (figure not shown) whose slope is equal to πk where k is the rate constant. The equations are represented in **Table 5.2** and the rate constants in **Table 5.3**.

Table 5.2 Kinetic equations of all the modified electrodes

Modifiers	**Equation**	**R^2**
GCE/**1**	$y = 9.889[N_2H_4] - 0.0057$	0.991
GCE/**1**(π)GQDs	$y = 1353\ [N_2H_4] - 597.7$	0.896
GCE/**2**	$y = 1279[N_2H_4] - 0.0661$	0.964
GCE/**2**(π)GQDs	$y = 0.9621\ [N_2H_4] - 0.0123$	0.998
GCE/**3**	$y = 68.78\ [N_2H_4] - 19.40$	0.837
GCE/**3**(π)GQDs	$y = 68.45\ [N_2H_4] - 17.36$	0.967
GCE/**1**-GQDs (seq)	$y = 7.295[N_2\ H_4\ ] - 1.269$	0.969
GCE/GQDs-**1**(seq)	$y = 7.0249\ [N_2\ H_4\ ] - 3.327$	0.788
GCE/**2**-GQDs (seq)	$y = 0.0504[N_2H_4] - 0.018$	0.959
GCE/GQDs-**2**(seq)	$y = 1.978[N_2H_4] - 0.076$	0.990
GCE/**3**-GQDs (seq)	$y = 0.086[N_2H_4] - 0.018$	0.985
GCE/GQDs-**3**(seq)	$y = 0.577[N_2H_4] - 0.0028$	0.968
GCE/**4**	$y = 204.1[N_2H_4] - 22.83$	0.940
GCE/**4**(π)rGQDs	$y = 249.8[N_2H_4] - 170.76$	0.939
GCE/**4**@rGQDs	$y = 8.858[N_2H_4] - 2.217$	0.956
GCE/**4**(π)NH_2GQDs	$y = 10.163[N_2H_4] - 0.0396$	0.986
GCE/**4**@NH_2GQDs	$y = 5.965[N_2H_4] - 1.713$	0.994
GCE/rGQDs	$y = 7.442[N_2H_4] - 1.972$	0.988
GCE/NH_2GQDs	$y = 4.524x[N_2H_4] - 4.922$	0.931

Comparing the Pc complexes alone; the largest k value was obtained for GCE/**4** showing the significance of the push-pull effect of the Pc compared to complexes **1**, **2** and **3**. The GCE/**1**(π)GQDs probe had a higher k value compared to GCE/**2**(π)GQDs and GCE/**3**(π)GQDs. The GCE/**1**(π)GQDs showed higher catalytic rate constant compared to complex **1** alone in GCE/**1**. On the other hand, for **2** and **3**, the k values decreased or remained unchanged on conjugation to GQDs, **Table 5.3**. High catalytic rate constants were obtained for sequentially modified electrodes (Pc on top of GQDs) for all the probes. This is because of the direct contact of the Pc with the hydrazine; such results emphasize the importance of the interactions between catalyst (CoPc) and analyte. The role of the interactions between complex **4** and the GQDs is further demonstrated by the obtained results. The non-covalently formed conjugates GCE/**4**(π)rGQDs and GCE/**4**(π)NH_2GQDs had higher catalytic constants compared to its corresponding covalent GCE/**4**@rGQDs and GCE/**4**@NH_2GQDs. The rGQDs containing conjugates gave better k values than the corresponding NH_2GQDs conjugates, owing to the superior activity of rGQDs due to its eliminated oxygen functionalities which result in a narrowed energy band gap.

5.4.2. LOD determination

Limit of detection (LOD) is the lowest possible concentration at which detection is feasible. Using the plots of concentration vs. current from chronoamperometry data (**Fig 5.5a, insert**) LOD values of all the probes were determined using the 3δ approach. The approach is as follows; several chronoamperometric evolutions are run in a blank solution repeatedly. A common point is chosen for all the obtained scans and a standard deviation is calculated (δ). This statistic is then multiplied by 3 to give the 3σ notation, which is later divided by sensitivity obtained from the slope of the concentration vs. current (**Fig 5.5a insert**) plot to give the limit of detection. Of the Pcs

alone, complex **4** had the lowest detection limit showing the importance of its push-push effect. Comparing complexes **1** (asymmetrical) and **2** (symmetrical) when alone, **2** had a lower detection limit, showing the tetra substitution to be advantageous. Comparing complex **2** (electron withdrawing substituents) and **3** (electron donating substituent), less favourable detection limits were obtained for **3**. Comparing the π-π stacked conjugates with the respective Pcs alone, better LOD values were obtained for all the conjugates except for **3**. Thus GQDs do not improve the electrocatalytic activity of **3** containing the electron donating (-NH_2 groups). Sequentially adsorbed electrodes where the Pc was adsorbed on top of GQDs (GQDs-CoPc) had lower LOD values compared to when the Pc is underneath (CoPc-GQDs). The non-covalently formed GCE/**4**(π)rGQDs and GCE/**4**(π)NH_2GQDsshowed more favourable LOD values compared to the corresponding covalently formed GCE/**4**@rGQDsand GCE/**4**@NH_2GQDs conjugates. The rGQDs containing conjugates gave better LOD values than the corresponding NH_2GQDs conjugates, which may suggest superior sensitivity of the rGQDs over NH_2GQDs towards hydrazine, **Table 5.3**.The LOD values obtained and reported in this work are less favourable than those reported in [**98**] and [**108**] but were found to be better than the 6.21μM and 9 μM [**109**]**,** 75 μM [**110**], 51.83 μM and 173 μM [**111**] for CoPc derivatives towards electrooxidation of hydrazine.

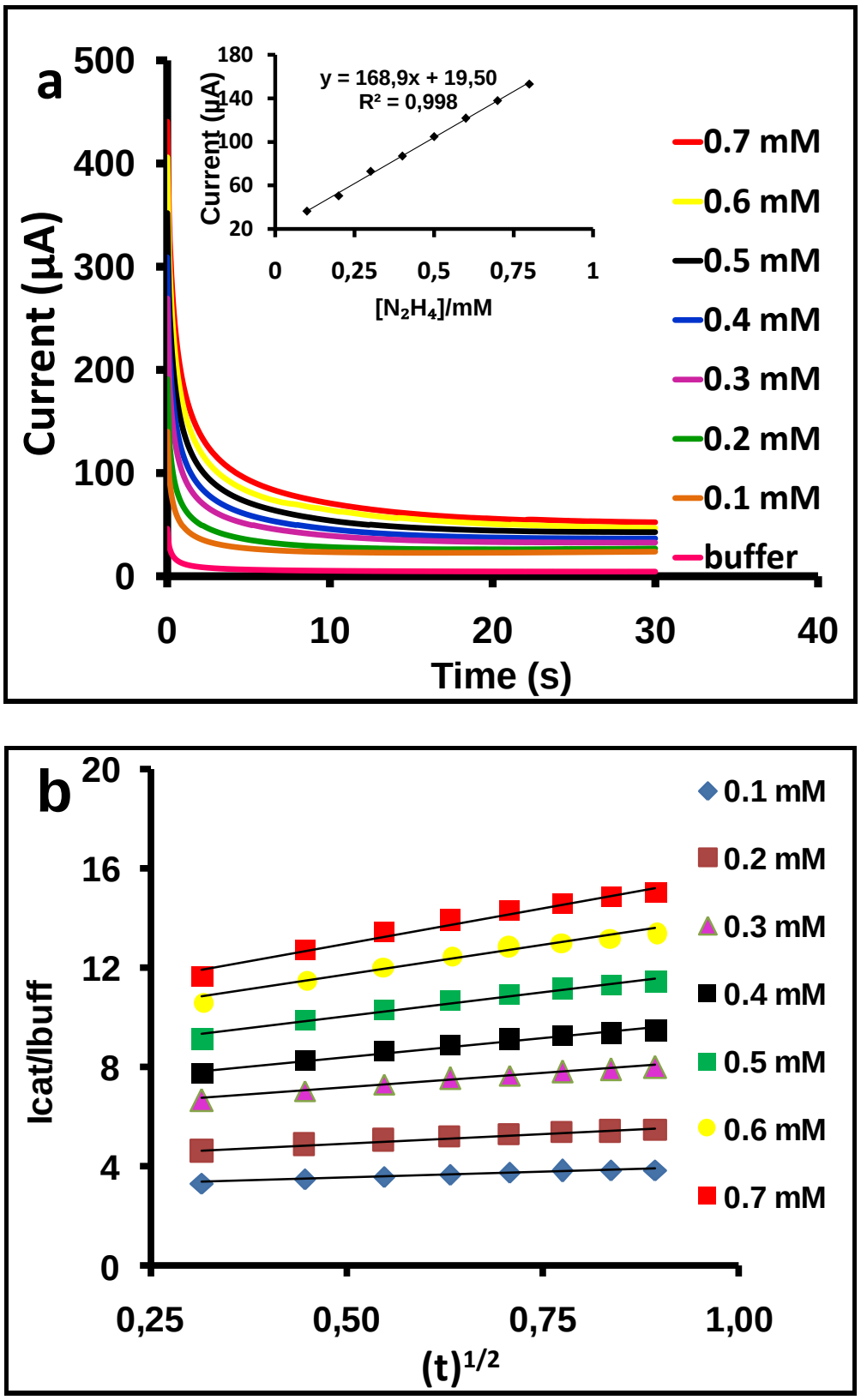

Fig 5.5 (**a**) Chronoamperometric scans of GCE/**2**(π)GQDs at various concentrations, **insert** = Current vs. hydrazine concentration and **(b)** plot of current vs. $t^{1/2}$.

Table 5.3 Limits of detection and catalytic rate constants obtained for all modified electrodes

Modified	**LOD (μM)**	**Catalytic rate constant (Ms^{-1})**
GCE/**1**	68	3.15×10^3
GCE/**1**(π)GQDs	10	4.31×10^5
GCE/**2**	33	4.07×10^4
GCE/**2**(π)GQDs	8	3.06×10^2
GCE/**3**	22	2.18×10^4
GCE/**3**(π)GQDs	43	2.19×10^4
GCE/**1**-GQDs (seq)	62	2.24×10^3
GCE/GQDs-**1** (seq)	46	2.32×10^3
GCE/**2**-GQDs (seq)	51	1.60×10^1
GCE/GQDs-**2** (seq)	20	6.29×10^2
GCE/**3**-GQDs (seq)	49	2.74×10^1
GCE/GQDs-**3** (seq)	18	1.83×10^2
GCE/rGQDs	6.6	2.37×10^3
GCE/NH_2GQDs	16.2	1.44×10^3
GCE/**4**	3.2	6.49×10^4
GCE/**4**@rGQDs	4.4	2.88×10^3
GCE/**4**(π)rGQDs	2.1	7.93×10^4
GCE/**4**@NH_2GQDs	8.6	1.90×10^3
GCE/**4**(π)NH_2GQDs	6.4	3.21×10^3

5.5. Mechanism for hydrazine electrooxidation by CoPc

The catalytic activity of phthalocyanines on the electrooxidation of hydrazine is determined by the central metal ion. The transition metal not only determines the activity but also dictates the mechanism of the process. The following reaction mechanism has been proposed for electrocatalytic oxidation of hydrazine on CoPc derivatives [**112**] equations **5.3** to **5.5**

$$[Co(II)Pc]_{surface} + N_2H_4 + OH^- \xrightarrow{rds} [Co(I)Pc \dots N_2H_3]^-_{surface} + H_2O \quad (\mathbf{5.3})$$

$$[Co(I)Pc \dots N_2H_3]^-_{surface} \rightarrow [Co(I)Pc]^-_{surface} + * N_2H_3 \quad (\mathbf{5.4})$$

$$* N_2H_3 + 3OH^- \xrightarrow{fast} N_2 + 3e^- + 3H_2O \quad (\mathbf{5.5})$$

This mechanism shows the involvement of the central Co metal in electrocatalysis. During the electrooxidation process the hydrazine molecule interacts with the metal centre, causing electron drain from one of the lone pair electrons of the nitrogen atoms of hydrazine towards the central metal. The active species Co(II)Pc is reduced to Co(I) by hydrazine undergoing oxidation, **eq. 5.3**. The Co(I)Pc-N_2H_3 is decomposed, **eq. 5.4**, with N_2H_3 released into solution to react with $^-$OH ions from the basic media (NaOH) to form N_2, **eq. 5.5**. From Co(I)Pc, Co(II)Pc can be generated, allowing repetition of the process.

5.6. Structure-Activity analysis: Effect of Substituents

5.6.1. Pristine GQDs conjugates

The difference in catalytic activity of the formed conjugates is owed to structural difference in the complexes **1, 2** and **3.** The structural arrangement of these complexes influence the manner in which they interact with the GQDs when conjugated. Following the Hunter-Sanders model for non-covalent interactions, where the strength of π-π interaction occurring is attributed to various contributors other than the π-electron cloud **[113]**. Pristine GQDs alone have their sp^2 carbon framework and dominant peripheral carboxylic groups. This structural arrangement allows for electrostatic contribution from the partially positive dipole charge of the carbonyl from the carboxylic groups on the GQDs edges during non-covalent interactions. The Pc complexes in addition to their π-electron conjugated systems are substituted such that; **1** and **2** have peripheral carboxyphenoxy groups (-O-Ph-COOH; Ph=phenoxy) while **3** has an aminophenoxy (-O-Ph-NH_2) group. The π-π interactions occurring between the GQDs and CoPc are contributed to by the interactions occurring between the carboxylic groups on the edge of GQDs and the substituents on the respective Pcs. As a result, **1**(π)GQDs and **2**(π)GQDs showed favourable catalytic activity in terms of LOD than **3**(π)GQDs, **Table 5.3**. Furthermore, better catalytic activity is obtained for **3** alone compared to when combined with GQDs in terms of currents and LOD values obtained. Where **1**(π)GQDs and **2**(π)GQDs conjugates are concerned, the similar dipole from the –COOH groups of both the GQDs and Pcs (**1** and **2**) results in electrostatic repulsion which prevents aggregation. Reduced aggregation between the GQDs and complexes implies minimal shielding of the central metal and rather increased exposure to the analyte and hence excellent catalytic activity observed in terms of current and hence the favourable LOD values. The amino group on the Pc

complex **3** affords it with hydrogen bonding contribution to the occurring π-π interactions with GQDs, where the amino groups serves as the donor and the carboxylic group of the GQDs is an acceptor. The strength of the hydrogen bonding encourages strong interactions between the two entities which might be conducive for aggregation and hence shielding of the metal centre and therefore minimal interaction with the analyte. Sequentially adsorbed electrodes where the Pc was on top (GQDs-CoPc) compared to when underneath (CoPc-GQDs) showed favourable catalytic activity in terms of catalytic current and LOD values. The variation in the catalytic activity of the electrodes is determined by the accessibility of the Pc to the hydrazine molecule during oxidation. For the GQDs-CoPc electrodes, the Pc metal center is well exposed to the analyte, compared to the CoPc-GQDs where the Pc central metal is shielded by the GQDs layer on top. As such, electrodes where the Pc was on top the electrooxidation of hydrazine was favoured given the fact that the mechanism of electrooxidation is governed by the Pc metal center (**Eq 5.3 – Eq 5.5**).

5.6.2. Functionalized GQDs conjugates

The rGQDs compared to the NH_2GQDs displayed higher electrocatalytic behaviour towards detection of hydrazine. The conductivity of GQDs in general is highly dependent on its structure as per determined by the energy band gap. The rGQDs were manufactured such that there was elimination of the excessive oxygen moieties on the surface, and introduction of new nitrogen containing groups on the edges. The NH_2GQDs on the other hand, are formed solely from peripheral modification while still maintaining the oxygenated core structure. As a result, there was intense narrowing of the energy band gap of the rGQDs compared to NH_2GQDs, hence better electrocatalytic performance. The use of tri-*tert*-butyl substituted push-pull cobalt phthalocyanine permits directionality of charge transfer from the highest occupied

molecular orbital (HOMO) to the lowest unoccupied molecular orbital (LUMO) level to the electrode surface, which then results in enhanced electrocatalytic activity [**114**]**.** The covalent conjugation of the CoPc to graphene quantum dots resulted in the disruption of its push pull effect (**Scheme 3.6**) upon conjugation, the phthalocyanine ends up having all electron donating group substituents. As a result, GCE/**4** has better electrocatalytic behaviour than GCE/**4**@rGQDs and GCE/**4**@NH_2GQDs in terms of current and LOD values. The non-covalent interactions of the CoPc to the rGQDs and NH_2GQDs result in the extension of its π-electron system. Extension therefore of the π system aids increased electron transfer abilities, which also enhances the electrocatalytic activity of the CoPc/GQDs complex, compared to CoPc alone. As a result the **4**(π)rGQDs modified electrode had favourable catalytic currents and LOD value compared to **4** alone. This was not the same for **4**(π)NH_2GQDs modified electrode. The difference in activity of the **4**(π)rGQDs and **4**(π)NH_2GQDs may be attributed the difference in chemical make-up of the planar GQD system as governed by the modification employed.

5.7. Conclusions

The reported probes displayed effective electrooxidation of hydrazine. The obtained results emphasize the role of structural arrangement (substituents and symmetry) of MPcs as electrocatalysts. Furthermore, the role of GQDs on the electrocatalytic activity of CoPc upon conjugation is determined by (**i**) the interactions between the two entities, (**ii**) the resulting structure (conjugate) and (**iii**) the way in which the formed conjugate will interact with the analyte. The non-covalently formed conjugates **1**(π)GQDs, **2**(π)GQDs, **3**(π)GQDs showed high catalytic currents and LOD values than the **1**, **2** and **3** alone. The sequentially adsorbed modified electrodes performed better when the Pc was on top (GQDs-Pc) than when underneath (Pc-GQDs), further

confirming the dependency of the electrooxidation of hydrazine reaction on the Pc. A definite oxidation peak for hydrazine was obtained for the functionalized rGQDs and NH_2GQDs compared to pristine GQDs alone. The non-covalent conjugates **4**(π)rGQDs and **4(**π)NH_2GQDs showed better catalytic activity than the covalently formed **4**@rGQDs and **4**@NH_2GQDs conjugates.

Chapter 6:
Final Conclusions

6. Conclusions and future aspects

6.1. General conclusions

The novel cobalt tris-tert-butylphenoxy monocarboxyphenoxy phthalocyanine (**4**) and the cobalt monocarboxyphenoxy phthalocyanine (**1**) were successfully synthesized as confirmed by the various spectroscopic techniques. The electrochemical activity of the CoPc derivatives has been proven to depend greatly on the symmetry and substituent of the phthalocyanines.

(i) The complexes **1** and **2** have the same substituents as a monocarboxyphenoxy and tetracarboxyphenoxy substituted CoPc respectively. Complex **2** displayed better catalytic activity in terms of LOD than **1** owing to the excessive active sites for interaction with the analyte and adsorption onto the electrode compared to the mono substituted complex **1**. The trend is maintained even upon conjugation to GQDs via π-π stacking. Better interactions occurring between **2** and GQDs compared to **1** and GQDs as a result of the symmetry.

(ii) The complexes **2** and **3** are both tetra substituted phthalocyanines with the (-COOH) electron withdrawing group and the electron donating (-NH_2) group respectively. The tetracarboxyphenoxy phthalocyanine **2** showed better electroactivity in terms of LOD compared to **3** alone and when both are combined with GQDs (**2**(π)GQDs and **3**(π)GQDs). The carboxylic group is a flat sp^2 hybridized entity therefore it is adsorbed easily onto the electrode, compared to the sp^3 hybridized out of plane -NH_2 group. The catalytic activity of these complexes in the presence of GQDs in turn is determined by their structural properties. Electrostatic repulsion occurring between the -COOH groups of both GQDs and **2** allow for access of the Co centre

(directs the oxidation of hydrazine) during catalysis. While, complex **3** and GQDs hydrogen bonding encourages stacking and aggregation which shield the Co centre during interaction and so low catalytic activity is observed. This demonstrates the contribution by substituents and structure in electrocatalytic activity.

(iii) The functionalization of GQDs not only reduces the energy band gap of the GQDs but also make them less polar which makes them more viable as surface modifiers and electrocatalysts in aqueous media.

(iv) The reduction of GQDs (rGQDs) does indeed narrow the band gap as shown by the high catalytic activity obtained compared to that of NH_2GQDs and pristine GQDs.

(v) The **4**(π)rGQDs and **4**(π)NH_2GQDs π-π stacked conjugates showed better catalytic activity than the covalently formed **4**@rGQDs and **4**@NH_2GQDs conjugate. This is owed to the (i) interactions occurring between the GQDs and the CoPc, (ii) the resultant structure formed as well as (iii) the preservation of the π-π of the Pc during interactions.

6.2. Future aspects

Electrocatalysis is dependent on the materials used as surface modifiers. The understanding of the structural contribution of MPcs onto their electrocatalytic activity is the key to designing novel and efficient electrocatalytic systems. Interactions between the catalyst and analyte detected are equally important and help understand the designed catalysts as well as their activity better. There is still greater room for the application of GQDs in electrocatalysis pristine and functionalized. Their structural flexibility and tuneable band gap leaves room for more discoveries. Metallophthalocyanines are essential for hydrazine detection.

REFERENCES

1. C. G. Claessens, U. Hahn and T. Torres, J. Chem. Rec., 8 (2008) 75
2. J. Garcia, A. Gonzalez, A. Gouloumis, E.M. Maya M.D. Perez, B.D. Rey, P. Vazquez and T. Torres, Tr. J. Chemistry.,22 (1998) 23
3. K. Sakamoto and E. Ohno-Okumura, Materials., 2 (2009)1127
4. Y. Wang, K. Wu, J. Kroger and R. Berndt, AIP Adv., 2 (2012) 041402
5. I. Balan, I.G. David, V. David, A. Stoica, C. Mihailciuc, I. Stamatin and A. A. Ciucu, J. Electroanal. Chem., 654 (2011) 8
6. M. G. Walter, A. B. Rudine and C. C. Wamser, J. Porphyr. Phthalocya.,14 (2010) 759
7. J. O Escobedo, O. Rusin, S. Lim and R. M. Strongin, J. Curr. Opin. Chem. Biol., 14 (2010) 64
8. D. Swain, R. Singh, V. K. Singh, N. V. Krishna, L. Giribabu and S. V. Rao, J. Mater. Chem. C, 2 (2014) 1711
9. J. Zhao, J. Wang, J. Chen, W. Chidawanykia, T. Nyokong, K. Ishii and N. Kobayashi, Med. Chem., 12 (2012) 604
10. J. H. Zagal, S. Griveau, J. F. Silva, T. Nyokong, and F. Bedioui, Coord. Chem. Rev., 254 (2010) 2755
11. A.B.P. Lever, E.R. Milaeva and G. Speier, The Phthalocyanines, Properties and Applications, in The Redox Chemistry of Metallophthalocyanines in solution, Vol. 3 ed., C.C. Leznoff and A.B.P. Lever, VCH, New York, 69 (1993)
12. N. B. McKeown, J. Mater. Chem., 10 (2000) 1979

13. H. Ali, R. Langlois, J. R. Wanger, N. Brasseur, B. Paquette and J.E. van Lier, Photochem. Photobiol., 47 (1988) 713
14. T. Nyokong and H. Isago, J. Porphyr. Phthalocya., 8 (2004) 1083
15. V.N. Nemykin and E.A. Lukyanets, Arkivoc (i) (2010) 136
16. T. Torres, J. Porphyr. Phthalocya., 4 (2000) 325
17. Y. Yan, S. Lu, B. Li, R. Zhu and S. Wei, J. Phys. Chem. A., 110 (2006) 10757
18. M. Shumba and T. Nyokong, J. Electrochim. Acta., 196 (2016) 457
19. V. Mani, S. Haung, R. Devasenathipathy and T. C. K. Yang, RSC Adv., 6 (2016) 38463
20. T. Mugadza and T. Nyokong, Polyhedron., 30 (2011) 1820
21. S. Bak, D. Kim and H. Lee, Curr. Appl. Phys., 16 (2016) 1192
22. H. Sun, L. Wu, W. Wei and X. Qu, Mater. Today, 12 (2013) 433
23. M. Bacon, S. J. Bradley and T. Nann, Part. Part. Syst. Char., 31 (2014) 415
24. A. Ananthanarayanan, Y. Wang, P. Routh, M. Alam Sk, A. Than, M. Lin, J. Zhang, J. Chen, H. Sun and P. Chen, Nanoscale 7 (2015) 8159
25. Y. Li, H. Shu, X. Niu and J. Wang, J. Phys. Chem. C., 119 (2015) 24950
26. N. Hashemzadeh, M. Hasanzadeh, N. Shadjou, J. Eivazi-Ziaei, M. Khoubnasabjafari and A. Jouyban, J. Pharmaceut. Anal., 6 (2016) 235
27. J. Fan, D. Li and X. Wang, Diam. Relat. Mater., 69 (2016) 81
28. K. L. Schroeder, R. V. Goreham and T. Nann, Pharm Res., 33 (2016) 2337
29. D. Du, K, Wang, Y. Wen, Y. Li and Y.Y. Li, ACS Appl. Mater. Interfaces.,8 (2016) 3287
30. G. Zhao, X. Li, M. Huang, Z. Zhen and Y. Zhong, Q. Chen, X. Zhao, Y. He, R. Hu, T. Yang and R. Zhang, C. Li, J. Kong, J. Xu, R. S. Ruoff and H. Zhu, Chem. Soc. Rev., 46 (2017) 4417

31. S. Navalon, A. Dhakshinamoorthy, M. Alvaro, M. Antonietti and H. Garcı'a, Chem. Soc. Rev., (2017) DOI: 10.1039/c7cs00156h
32. Z. Jin, P. Owour, S. Lei and L. Ge, Curr. Opin. Colloid Interface Sci., 20 (2015) 439
33. S. Kellici, J. Acord, N. P. Power, D. J. Morgan, P. Coppo,T. Heilf and B. Saha, RSC Adv., 7 (2017) 14716
34. L. Yan, Y. B. Zheng, F. Zhao, S. Li, X. Gao, B. Xu, P. S. Weiss and Y. Zhao, Chem. Soc. Rev., 41 (2012) 97
35. B. Qi, H. Hu, L. Bao, Z. Zhang, B. Tang, Y. Peng, B. Wang and D. Pang, Nanoscale, 7 (2015) 5969
36. X. T. Zheng, A. Ananthanarayanan, K. Q. Luo and P. Chen, Small 11 (2015) 1620
37. J. Ryu, E. Lee, S. Lee and J. Jang, Chem. Comm., 50 (2014) 15616
38. A. Mathkar, D. Tozier, P. Cox, P. Ong, C. Galande, K. Balakrishnan, A. Reddy and P. M. Ajayan, J. Phys. Chem. Lett., 3 (2012) 986
39. R. Yadav and C.K. Dixit, J. Sci. Adv. Mater. Dev., 2 (2017) 141
40. Z. L. Wu, Z. X. Liu and Y. H. Yuan, J. Mater. Chem. B., (2017), DOI: 10.1039/C7TB00363C.
41. J. J. L. Hmar, T. Majumder, S. Dhar and S. P. Mondal, Thin Solid Films, (2016) doi: 10.1016/j.tsf.2016.06.014
42. K. H Koh, S. H. Noh, T. Kim, W.J. Lee, S. Yi and T. H. Han, RSC Adv., 7 (2017) 26113
43. J. Wang, Y. Zhang, J. Ye and Z. Jiang, J. Lumin., 32 (2017) 573
44. R. Matshitse, K. E. Sekhosana, O. J. Achadu and T. Nyokong, J. Coord. Chem., 70 (2017) 3308
45. O. J. Achadu, I. Uddin and T. Nyokong, J. Photochem. Photobio A., 317 (2016) 12
46. O. J. Achadu and T. Nyokong, New J. Chem., 40 (2016) 8727

47. O. J. Achadu and T. Nyokong, Talanta 166 (2017) 15
48. O. J. Achadu, M. Managa and T. Nyokong, J. Photochem. Photobio., 333 (2017) 174
49. O. J. Achadu and T. Nyokong, Spectrochim. Acta., A 174 (2017) 339
50. D. M. Mafukidze and T. Nyokong, J. Coord. Chem., 70 (2017) 3598
51. O. M. Bankole, O. J. Achadu and T. Nyokong, J Fluoresc., 27 (2017) 755
52. M. L Waters, Curr. Opin. Chem. Biol., 6 (2002) 736
53. C. A. Hunter and J. K.M Sanders, J. Am. Chem. Soc., 112 (1990) 5525
54. A. L. Ringer, M. O. Sinnokrot, R. P. Lively, and C. D. Sherrill, Chem. Eur. J., 12 (2006) 3821
55. Herrero, E., Feliu, J. M. and Aldaz, A. 2007. Electrocatalysis. Encyclopaedia of Electrochemistry, DOI:10.1002/9783527610426.bard020501
56. Royce W. Murray, A. G. Ewing and R. A. Durst, J. Anal. Chem., 59 (1987) 379
57. D. A. Geraldo, C. A. Togo, J. Limson and T. Nyokong, Electrochim. Acta., 53 (2008) 8051
58. K.D. Snell and A.G. Keenan, Chem. Soc. Rev., 8 (1979) 259
59. A. B. Sorokin, Chem. Rev.,113 (2013) 8152
60. A. L. Beilby, T. A. Sasaki and H. M. Stem, Anal. Chem., 67 (1995) 97
61. M. Sajid, M. K. Nazal, M. Mansha, A. Alsharaa, S. M. Jillani and C. Basheer, Trends. Anal. Chem., (2015), DOI: 10.1016/j.trac.2015.09.006
62. G. Li and P. Miao, Electrochemical Analysis of Protein and Cells, in Theoretical Backgrounds of Electrochemical Analysis, Springer (2012) DOI: 10.1007/978-3-642-34252-3_2
63. J. E. Troyan, Ind. Eng. Chem., 45 (1953) 2608

64. Chemicals Evaluation and Research Institute (CERI) in collaboration with the National Institution of Technology and Evaluation (NITE), New Energy Industrial Development Technology Organisation (NEDO), Hydrazine Assessment Report, Japan
65. Y. Yan, S. Lu, B. Li, R. Zhu and S. Wei, J. Phys. Chem. A, 110 (2006) 10757
66. M. Shumba and T. Nyokong, Electrochim. Acta, 196 (2016) 457
67. O. J. Achadu, I. Uddin and T. Nyokong, J. Photochem. Photobiol. A: 317 (2016) 12
68. T. Fan, W. Zeng, W. Tang, C. Yuan, S. Tong, K. Cai, Y. Liu, W. Huang, Y. Min and A. J. Epstein, Nanoscale Res. Let 10 (2015) DOI 10.1186/s11671-015-07839
69. X. F. Zhang and X. Shao, J. Photochem. Photobiol. A. 278 (2014) 69
70. T. Sainsbury, M. Passarelli, M. Naftally, S. Gnaniah, S. J. Spencer and A. J. Pollard, ACS Appl. Mater. Interfaces, 8 (2016) 4870
71. G. S. Kumar, R. Roy, D. Sen, U. K. Ghorai, R. Thapa, N. Mazumder, S. Sahab and K. K. Chattopadhyay, Nanoscale 6 (2014) 3384
72. C. Xu, X. Shi, A. Ji, L. Shi, C. Zhou and Y. Cui, PLoS One. 10 (2015) e0144842.
73. A. Navaee and A. Salimi, RSC Adv., 5 (2015) 59874
74. G. Rajender and P. K. Giri, J. Mater. Chem. C 4 (2016) 10852
75. X. Xu, F. Gao, X. Bai, F. Liu, W. Kong and M. Li, Materials 10 (2017) DOI:10.3390/ma10111328
76. Y. Dong, X. Zhang, X. Cheng, Y. Xu, S. Gao, H. Zhao and L. Huo, RSC Adv., 2014, 4, 57493
77. S. Karna, M. Mahat, T. Choi, R. Shimada, Z. Wang and A. Neogi, Sci. Rep. 6 (2016) DOI: 10.1038/srep36898
78. C. Hsieh, D.Tzou, K. Hsieh and K. Yin, RSC Adv., 7 (2017) 18340

79. W. Zhang, Y. Liu, X. Meng, T. Ding, Y. Xu, H. Xu, Y. Ren, B. Liu, J. Huang, J. Yang and X. Fang, Phys. Chem. Chem. Phys., 17 (2015) 22361

80. Y. Fenga, J. Zhao, X. Yan, F. Tang and Q. Xue, Carbon 66 (2014) 334

81. Y. Sun, S. Wang, C. Li, P. Luo, L. Tao, Y. Wei and G. Shi, Phys. Chem. Chem. Phys., 15 (2013) 9907

82. H. Whatley in Basic Principle and Capillary Electrophoresis., ed. J.R Peterson and A.A Mohammad., Humana Press Inc, Totowa, NJ, Ch 2.

83. J.L. Beckers and P. Bocek, Electrophoresis 21 (2000) 2747

84. S.P. Porras, M. Riekkola and E. Kenndler, Electrophoresis 24 (2003) 1485

85. M. J. Stillman and T. Nyokong in:Phthalocyanines - Properties and Applications, Edited by A. B. C. Lever, C. C. Leznoff, VCH, New York, Vol.1 1989. Chapt. 3

86. Z. D. Liu, H. X. Zhao and C. Z. Huang, PLoS ONE 7 (2012) e50367

87. M. H. V. Reddy, R. M. Al-Shammari, N. Al-Attar, S. Lopez, T. E. Keyes and J. H. Rice, Proc. SPIE 9172 (2014) DOI: 10.1117/ 12.2061951

88. X. Cai, Y. Zhang, X. Zhang and J. Jiang, J. Molec. Struct. Theochem. 801 (2006) 71

89. P. Baerker and A.V Salker, Indian J. Chem. Technol. 13 (2006) 341

90. A. Fashina and E. Antunes, T. Nyokong, Polyhedron 53 (2013) 278

91. F.J Rawson, A.J. Downard and K.H. Baronian, Sci. Rep. 4 (2014) DOI:10.1038/srep05216

92. R. L. McCreery, Chem. Rev. 108 (2008) 2646

93. A. Salimi, C.E. Banks and R.G. Compton, Phys. Chem. Chem. Phys. 5 (2003) 3988

94. A. J. Bard, F. F. Fan, J. Kwak, and O. Lev, Anal. Chem. 61 (1989) 132

95. R. C. Engstrom and C. M. Pharr, J. Anal. Chem. 61 (1989) 1099A

96. C. G. Zoski, J. Electrochem. Soc. 163 (2016) H3088

97. D. Polcari, P. Dauphin-Ducharme and J. Mauzeroll, Chem. Rev. 16 (2016) 13234

98. C. S. J.N. O'Donoghue, G. Fomo and T. Nyokong, J. Electroanal. 28 (2016) 3019

99. I.G. Casella and M. Contursi, J. Electroanal 24 (2012) 752

100. F. Bure. RSC Adv., 4 (2014) 58826

101. A. Salimi, K. Abdi, Talanta., 2(2004) 475

102. J. M. Zen, A. Senthil Kumar and M. R. Chang, Electrochim. Acta. 10 (2000) 1691

103. C. A. Caro, F. Bedioui and J. H. Zagal, Electrochim. Acta. 9 (2002) 1489

104. K. Kunimatsu, T. Senzaki, M. Tsushima, M. Osawa, Electrochem. Soc., 249 (2005) 2004

105. D. Nkosi and K.I. Ozoemena, J. Electroanal. Chem. 628 (2008) 304

106. T. Mugadza and T. Nyokong. J. Electrochim. Acta 56 (2011) 1995

107. M. H. Pournaghi-Azar, R. J. Sabzi. Electroanal. Chem. 543 (2003) 115–125

108. S. R. Nxele, P. Mashazi, T. Nyokong, Electroanal., 27 (2015) 2468

109. C. Foster, J. Pillay, J. Metters and C. Banks, Sensors 14 (2014) 21905

110. C. Conceicao, R. Faria, O. Fatibello-Filho and A. Tanaka, Anal. Lett. 41 (2008) 1010

111. C. Canales, L. Gedi, R. Arce and G. Ramirez, New J. Chem. 40 (2016) 2806

112. F. S. Damos, R. de Cassia Silva Luz and A. A. Tanaka, in Electrochemistry of N4 Macrocyclic Metal Complexes (Eds: J. H. Zagal, F. Bedioui), Springer International Publishing; 2016, pp. 201–224.

113. M. Cao, A. Fu, Z. Wang, J. Liu, N. Kong, X. Zong and H. Liu, J. Phys. Chem. C, 118 (2014) 2650

114. N. Masilela, N. Nombona, T. Loewenstein, T. Nyokong and D. Schlettwein, J. Porphyr. Phthalocya., 14 (2010) 986